THESIS FOR THE DEGREE OF DOCTOR OF PHILOSOPHY

On-scalp MEG using high-T_c SQUIDs: Measuring brain activity with superconducting magnetometers

CHRISTOPH PFEIFFER

On-scalp MEG using high-T_c SQUIDs:
Measuring brain activity with superconducting magnetometers
CHRISTOPH PFEIFFER

Cover:
Top left: MRI of a subject's head with N20m sources localized with on-scalp and conventional MEG. *Top right:* On-scalp MEG sensors localized on a subject's head. *Bottom right:* Occipital alpha recorded with the 7-channel systems. *Bottom left:* Tail of the 7-channel system with the vacuum window removed, showing the SQUID sensors. *Center:* 7-channel system placed to record from the author's head.

On-scalp MEG using high-T_c SQUIDs:
Measuring brain activity with superconducting magnetometers
CHRISTOPH PFEIFFER
Department of Microtechnology and Nanoscience
Chalmers University of Technology

Abstract

This thesis describes work done towards realizing on-scalp magnetoencephalography (MEG) based on high critical temperature (high-T_c) superconducting quantum interference device (SQUID) sensors. MEG is a non-invasive neuroimaging modality that records the magnetic fields produced by neural currents with good spatial and high temporal resolution. However, state-of-the-art MEG is limited by the use of liquid helium-cooled sensors (T $\sim$4 K). The amount of thermal insulation between the sensors and the subject's head that is required to achieve the extreme temperature difference ($\sim$300 K), typically realized in the form of superinsulation foil and $\sim$2 centimeters of vacuum, limits measurable signals. Replacing the sensors with high-T_c SQUIDs can mitigate this problem. High-T_c SQUIDs operate at much higher temperatures ($\leq$90 K) allowing significant reduction of the stand-off distance (to $\sim$1 mm). They can furthermore be cooled with liquid nitrogen (77 K), a cheaper, more sustainable alternative to the liquid helium used for cooling in conventional MEG systems.

The work described in this thesis can be divided into three main areas: (I) simulation work for practical implementations of on-scalp systems, (II) development of a 7-channel high-T_c SQUID-based on-scalp MEG system, and (III) on-scalp MEG recordings.

In the first part, spatial information density (SID), a metric to evaluate the performance of simulated MEG sensor arrays, is introduced and - along with total information capacity - used to compare the performance of various simulated full-head on-scalp MEG sensor arrays. Simulations demonstrate the potential of on-scalp MEG, with all on-scalp systems exhibiting higher information capacity than the state-of-the-art. SID further reveals more homogeneous sampling of the brain with flexible systems. A method for localizing magnetometers in on-scalp MEG systems is introduced and tested in simulations. The method uses small, magnetic dipole-like coils to determine the location and orientation of individual sensors, enabling straightforward co-registration in flexible on-scalp MEG systems. The effects of different uncertainties and errors on the accuracy of the method were quantified.

In the second part, design, construction, and performance of a 7-channel on-scalp MEG system is described. The system houses seven densely-packed (2 mm edge-to-edge), head-aligned high-T_c SQUID magnetometers (9.2 mm x 8.6 mm) inside a single, liquid nitrogen-cooled cryostat. With a single filling, the system can be utilized for MEG recordings for >16 h with low noise levels ($\sim$50-130 fT). Using synchronized clocks and a direct injection feedback scheme, the system achieves low sensor crosstalk (<0.6%).

In the third part, on-scalp MEG recordings with the 7-channel system as well as its predecessor, a single-channel system, are presented. The recordings are divided into proof-of-principle and benchmarking experiments. The former consist of well-studied, simple paradigms such as auditory evoked activity and visual alpha. Expected signal components were clearly seen in the on-scalp recordings. The benchmarking studies were done to compare and contrast on-scalp with state-of-the-art MEG. To this end, a number of experimental stimulus paradigms were recorded on human subjects with the high-T_c SQUID-based on-scalp systems as well as a state-of-the-art, commercial full-head MEG system. Results include the expected signal gains that are associated with recording on-scalp as well as new details of the neurophysiological signals. Using the previously described on-scalp MEG co-registration method enabled source localization with high agreement to the full-head recording (the distance between dipoles localized with the two systems was 4.2 mm).

Keywords: magnetoencephalography, on-scalp MEG, high-T_c SQUID, magnetometer, sensor array, localization, neuroimaging.

This thesis is dedicated to my son, Francisco.
Always be curious and dare to question.

List of Papers

This thesis is based on the work contained in the following papers:

I. **Evaluation of realistic layouts for next generation on-scalp MEG: spatial information density maps**, B. Riaz, C. Pfeiffer and J.F. Schneiderman, *Scientific Reports*, **7**: 6974, 2017

II. **Localizing on-scalp MEG sensors using an array of magnetic dipole coils**, C. Pfeiffer, L.M. Andersen, D. Lundqvist, M. Hämäläinen, J.F. Schneiderman and R. Oostenveld, *PLOS ONE*, **13**(5): e0191111, 2018

III. **A 7-channel high-T_c SQUID-based on-scalp MEG system**, C. Pfeiffer, S. Ruffieux, L. Jönsson, M.L. Chukharkin, A. Kalaboukhov, M. Xie, D. Winkler and J.F. Schneiderman, *IEEE Trans. Biomed. Eng.*, DOI: 10.1109/TBME.2019.2938688 (early access), 2019

IV. **Sensor localization using magnetic dipole-like coils: A method for highly accurate co-registration in on-scalp MEG**, C. Pfeiffer, S. Ruffieux, L.M. Andersen, A. Kalaboukhov, D. Winkler, R. Oostenveld, D. Lundqvist and J.F. Schneiderman, *NeuroImage*, under revision, 2019 - *preprint on bioRxiv: 661678*

V. **Similarities and differences between on-scalp and conventional in-helmet magnetoencephalography recordings**, L.M. Andersen, R. Oostenveld, C. Pfeiffer, S. Ruffieux, V. Jousmäki, M. Hämäläinen, J.F. Schneiderman and D. Lundqvist, *PLOS ONE*, **12**(7): e0178602, 2017

VI. **On-scalp MEG SQUIDs are sensitive to early somatosensory activity unseen by conventional MEG**, L.M. Andersen, C. Pfeiffer, S. Ruffieux, B. Riaz, D. Winkler, J.F. Schneiderman and D. Lundqvist, *NeuroImage*, under revision, 2019 - *preprint on bioRxiv: 686329*

Other papers outside the scope of this thesis:

VII. **Feedback solutions for low crosstalk in dense arrays of high-T_c SQUIDs for on-scalp MEG**, S. Ruffieux, M. Xie, M. Chukharkin, C. Pfeiffer, A. Kalabukhov, D. Winkler and J.F. Schneiderman, *Supercond. Sci. Technol.*, **30**: 054006, 2017

List of Abbreviations

MEG	magnetoencephalography
EEG	electroencephalography
MRI	magnetic resonance image
SQUID	superconducting quantum interference device
OPM	optically pumped magnetometer
T_c	critical transiton temperature of a superconductor
J_c	critical current density
SNR	signal-to-noise-ratio
ECD	equivalent current dipole
MNE	minimum norm estimate
MUSIC	multiple signal classification
HPI	Head position indicator
ICP	iterative closest point
DC	direct current
AC	alternating current
RCSJ	resistively- and capacitively shunted junction
YBCO	yttrium barium copper oxide ($YBa_2Cu_3O_{7-x}$)
STO	strontium titanate ($SrTiO_3$)
CVD	chemical vapor deposition
PLD	pulsed laser deposition
FLL	flux locked loop
LHe	liquid helium
LN_2	liquid nitrogen
MSR	magnetically shielded room
SID	spatial information density
FFT	fast fourier transform
PCB	printed circuit board
DAQ	data acquisition
AEF	auditory evoked field
AI	primary auditory cortex
ISI	inter-stimulus interval
SF	sustained field
SEF	somatosensory evoked field
SI	primary somatosensory cortex
SII	secondary somatosensory cortex
PPC	posterior parietal cortex
HFO	high frequency oscillation

Contents

Contents

1

Introduction

Magnetoencephalography (MEG) is a non-invasive functional neuroimaging method based on measuring magnetic fields that originate from the brain. Similar to electroencephalography (EEG), it detects electromagnetic activity generated by neural currents. Based on the measured activity, the location of the neural generators can be estimated. Since the first recording in 1968, MEG has been developed into a useful tool for neuroscience. With its combination of high spatial and temporal resolution, MEG has led to a number of discoveries over the years [1, 2]. Clinically, MEG is used primarily to localize epileptic foci and map important brain functions prior to surgery [3].

A major challenge in MEG is the extremely low magnitude of the magnetic fields of interest. Typical fields are on the order of hundreds of femtotesla (1 fT $= 10^{-15}$T). For comparison, the earth's magnetic field is some 8 orders of magnitude higher at $\sim$50 μT. For the first MEG recordings in humans, Cohen used a large (9 cm by 9 cm), 1-million-turn coil with ferrite core inside a magnetically shielded room to record fields on the order of 30-100 fT [4]. Even then, averaging thousands of trials was necessary to extract the extremely low signals from the noisy measurement.

MEG made a leap forward with the introduction of superconducting quantum interference device (SQUID) sensors which eventually increased field sensitivity by a factor of $\sim$100-200. Such low sensor noise levels, combined with the construction of sensor arrays with increasing sensor count in the 1980s and 1990s, was critical to the development of the modern MEG systems used today. State-of-the-art MEG systems sample the neuromagnetic field at hundreds of locations around the subject's head [1].

A major limitation of these systems stems from the fact that the SQUID sensors have to be cooled with liquid helium ($\sim$4 K) to reach operating temperature. High thermal insulation, typically several layers of superinsulation foil along with a few centimeters of vacuum, has to be placed between the sensors and the subject in order to maintain the extreme temperature difference. This increases the distance to neural sources in the subject's brain, which diminishes the magnitude of the measurable signals because magnetic fields generated by neural currents decrease approximately with the square of the distance from the sources (i.e., the neural currents)[3].

The development of new types of sensitive magnetic field sensors that operate at higher temperatures might enable MEG to make yet another leap in terms of sensitivity and resolution. High critical temperature (high-T_c) SQUIDs (as opposed to conventional, low-T_c SQUIDs), for example, operate at temperatures high enough to cool them with liquid nitrogen ($\sim$77 K). In addition to being cheaper and more

sustainable, cooling with liquid nitrogen makes it possible to use simpler cryogenics and to place the sensors within 1 millimeter of objects at room temperature [5, 6], e.g., the subject's head. In addition to an increase in signal magnitude, moving the sensors to "on-scalp" is expected to improve the spatial resolution of MEG [7, 8]. Recordings with individual high-T_c SQUIDs have shown their feasibility for on-scalp MEG [9] as well as the expected increase in signal [10]. However, to utilize the full potential of high-T_c SQUID-based on-scalp MEG, whole-head coverage is required. As the 20 years of development of conventional, full-head MEG shows, going from single-channel systems to whole-head coverage represents a large endeavor.

The work presented in this thesis was part of a larger project called NeuroSQUID (funded by the Knut and Alice Wallenberg Foundation, KAW 2014.0102) with the aim of developing high-T_c SQUID-based on-scalp MEG. One of the main goals of the project and the aim of this work was to develop multichannel on-scalp MEG systems and test their usefulness for neuroscience.

1.1 Outline

In Chapter 2, a general background for MEG is provided, explaining signal origins, important analysis concepts, and essential instrumentation, with a focus on SQUID sensors. Chapter 3 describes the concept of on-scalp MEG in more detail and shows simulation for quantifying the benefits and guiding the design of practical full-head on-scalp MEG systems. In Chapter 4, a 7-channel on-scalp MEG system developed as part of this work is presented in detail. A single-channel system that was used in previous on-scalp MEG recordings is also briefly described. In Chapter 5, on-scalp MEG recordings with the systems described in Chapter 4 are presented. Chapter 6 provides conclusions of the thesis along with an outlook.

2

MEG

This chapter provides theoretical background about MEG. The physiological basis of neuromagnetic signals is introduced before discussing how these signals can be analyzed and interpreted. Finally, essential MEG instrumentation, namely SQUIDs, cryostats, and magnetic shielding, is presented.

2.1 Neuromagnetic fields

Neurons are the basic building block of the brain. They consist of a cell body (soma) with several dendrites that provide input to the cell and an axon through which output signals travel to the synapses where they are transferred to neighboring neurons, c.f., Fig. 2.1. The dendrites and cell body receive excitatory or inhibitory inputs from other neurons through those synapses. If the sum of excitatory and inhibitory inputs to a neurons passes a threshold, then voltage sensitive ion channels on the neuron's axon membrane open. The resulting inflow of ions (Na^+ and K^+) depolarizes a volume that encloses other ion channels, resulting in neighboring ion channels opening up, leading to a chain reaction. This wave of depolarization is followed shortly after by a repolarization wave. Together, the depolarization and repolarization waves make up the action potential. Once the action potential reaches a synapse in the axon terminal, transmitter molecules are released that diffuse through the postsynaptic cleft and attach to receptors on the following (receiving) cell which, in turn, leads to the opening of ion channels in its membrane. Ions (primarily Na^+, K^+ or Cl^-) flow from the postsynaptic cleft into the dendrites of the receiving cell and from there to the soma, creating the postsynaptic current/potential. The direction of the postsynaptic current and polarity of the postsynaptic potential, respectively, depends on the type of channels opened, as they are ion selective [11] (negative ions for excitatory, positive for inhibitory inputs). The postsynaptic current/potential lasts significantly longer ($\sim$20 ms) than the action potential [2, 11].

Following Maxwell's fourth law (Ampére's law with Maxwell's addition) an electric current (e.g., the postsynaptic current) gives rise to a magnetic field $\boldsymbol{B}$ as

$$\nabla \times \boldsymbol{B} = \mu_0(\boldsymbol{J} + \epsilon_0 \frac{\partial \boldsymbol{E}}{\partial t}),\tag{2.1}$$

where $\boldsymbol{J}$ is the current density and $\boldsymbol{E}$ is the electric field. We can use the quasistatic approximation for $\boldsymbol{B}$ as it can be shown that, assuming realistic material properties for the brain tissue, the time-derivative terms of $\boldsymbol{E}$ and $\boldsymbol{B}$ are negligible in the
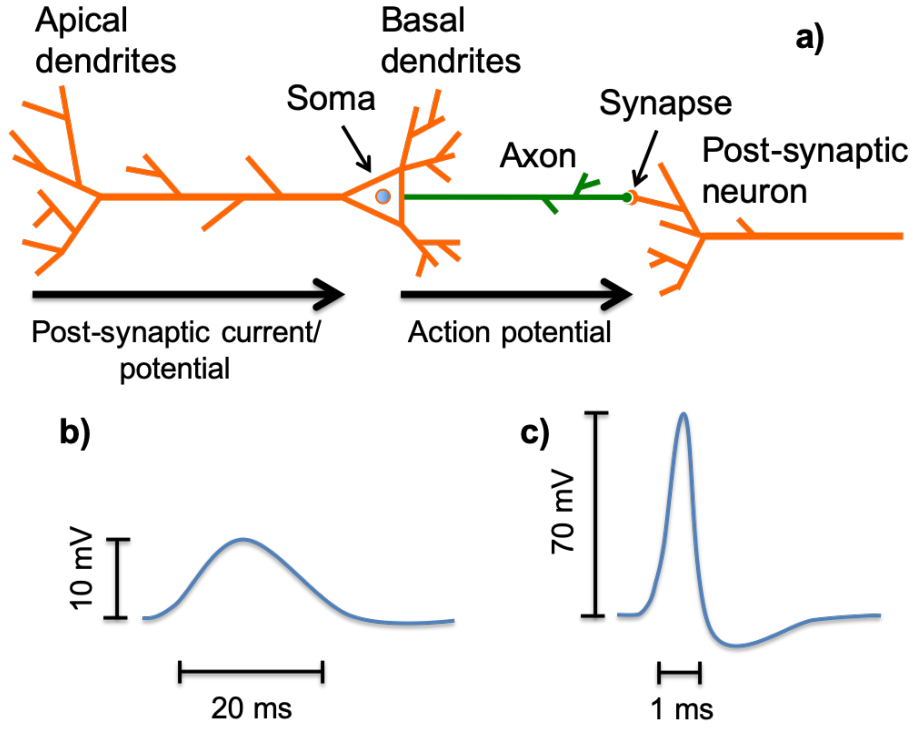
Figure 2.1: Neural signaling. a) Simplified schematic of a pyramidal neuron showing the direction of post-synaptic currents and potentials, as well as action potentials. b) Schematic time course of excitatory post-synaptic current and c) action potential.

frequencies of neuromagnetic interest (0.1 - 1000 Hz) [11, 12]. Eq. 2.1 therefore reduces to Ampére's law:

$$\nabla \times \boldsymbol{B} = \mu_0 \boldsymbol{J} \tag{2.2}$$

Since no net charge can build up in the brain, neural currents have to form a closed loop. Charge is returned via volume currents through the extracellular conducting medium. The current density $\boldsymbol{J}$ can therefore be divided into a primary current $\boldsymbol{J}^p$ that flows in the neural dendrites and a return (or volume) current $\boldsymbol{J}^r$ that flows through the extracellular medium:

$$\boldsymbol{J} = \boldsymbol{J}^p + \boldsymbol{J}^r = \boldsymbol{J}^p + \sigma \boldsymbol{E}. \tag{2.3}$$

Both currents take part in the generation of neuromagnetic fields, but mainly the primary current is of interest in neuroscience. For simplicity, the primary current is often approximated by a current dipole, i.e., a point-like current source with a direction and magnitude. The primary current density then becomes $\boldsymbol{J}^p(r) = \boldsymbol{Q}\delta(\boldsymbol{r} - \boldsymbol{r}_Q)$ where $\boldsymbol{Q}$ is a vector describing the current dipole and δ the delta function [13].

The magnetic field $\boldsymbol{B}$ at location $\boldsymbol{r}$ generated by a neural current at r' can be calculated using the Ampère-Laplace law

$$\boldsymbol{B}(\boldsymbol{r}) = \frac{\mu_0}{4\pi} \int \frac{\boldsymbol{J}(\boldsymbol{r}') \times \boldsymbol{R}}{|R|^3} dv, \tag{2.4}$$

where $\boldsymbol{R} = \boldsymbol{r} - \boldsymbol{r'}$.

In the following, we will focus on the contribution of the primary current. However, to correctly solve Eq. 2.4 (which is called generating a forward solution) both contributions have to be determined. The contribution of the volume currents can be solved numerically with boundary or finite element methods using a structural magnetic resonance (MR) image of the subject's head [11, 12].

The postsynaptic and action potentials of a single neuron generate current dipoles of approximately 20-200 fAm and 100 fAm, respectively [13]. The magnetic field generated by a single neuron would therefore be far too weak to measure outside the head. Fortunately, grey matter, specifically the cerebral cortex, contains a large number of parallel-oriented (pyramidal) neurons aligned perpendicular to the cortical surface [14]. Magnetic fields generated by close-by parallel current dipoles can then sum up. The signals typically measured in MEG are the result of ∼10 000 - 50 000 aligned neurons with post-synaptic currents that are flowing roughly simultaneously (summing up to current dipole moments on the order of 10 nAm) [15]. Assuming 100 neurons in a cortical patch with 40 μm diameter, 50 000 neurons corresponds to a cortical area of at least ∼0.6 mm^2 [16] (assuming all cells fire and none of them produce opposing fields, which would increase the required number of neurons). Due to their longer duration and lack of a large repolarization cycle (c.f., Fig. 2.1), there is significantly larger temporal overlap for postsynaptic potentials/currents as compared to action potentials. The resulting summation effect for the fields generated by postsynaptic potentials/currents, combined with the parallel alignment of dendrites (c.f., Fig. 2.2), is what makes neural currents generated by the grey matter of the cerebral cortex measurable outside the head. Action potentials, on the other hand, are relatively silent [2]. Observing action potentials is furthermore hindered by the fact that the depolarization and repolarization waves that comprise them behave as two opposing currents, forming a current quadrupole [11, 17]. Signals recorded by MEG (as well as EEG) are therefore primarily the result of postsynaptic potentials/currents [13, 14].
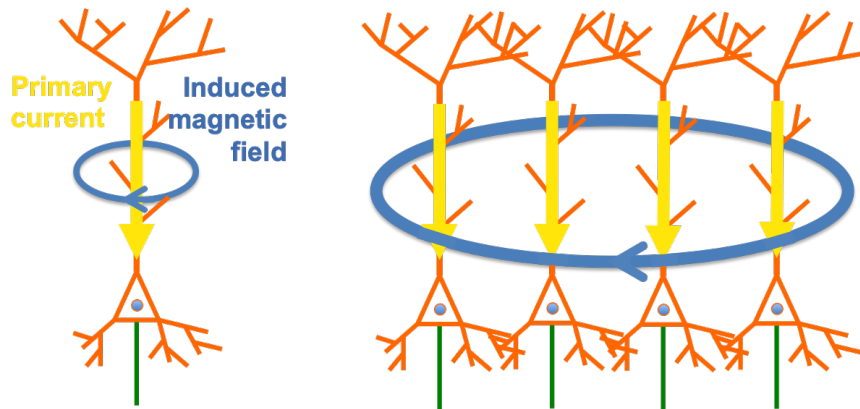

Figure 2.2: Magnetic field (blue) generated by the primary current (yellow) in one (left) and multiple, aligned neurons (right).

Current dipoles produce magnetic fields that are primarily perpendicular to the current direction. MEG is therefore most sensitive to tangential sources, such as pyramidal neurons in the walls of sulci [2, 3]. Due to the ∼ $1/R^2$ dependence of the

magnetic fields generated by a current dipole (eq. 2.4) MEG is furthermore more sensitive to superficial sources.

2.2 From signals to brain activity

MEG systems measure neuromagnetic fields outside the subject's head using magnetic field sensors that convert magnetic fields to electric signals. They are typically only sensitive to fields in one direction (or the gradient in one direction). By approximating the magnetic field sensors as point magnetometers, the signals b measured by the sensors i can generally be represented with the following simple relationship:

$$b_i(\boldsymbol{r}_i) = \boldsymbol{B}(\boldsymbol{r}_i) \cdot \boldsymbol{n}_i, \tag{2.5}$$

where $\boldsymbol{n}_i$ is a vector describing the sensitivity of the sensor located at position $\boldsymbol{r}_i$. More complex magnetic field sensors can be approximated by the combination of multiple point magnetometers (e.g., a planar gradiometer by the difference of two point magnetometers or a coil as an average of multiple point magnetometers distributed over the coil area).

In practice, the signals recorded in MEG are afflicted with noise from the sensors $b_{noise,i}$ as well as field noise from the environment $\boldsymbol{B}_{noise}$:

$$b_i(\boldsymbol{r}_i) = (\boldsymbol{B}(\boldsymbol{r}_i) + \boldsymbol{B}_{noise}(\boldsymbol{r}_i)) \cdot \boldsymbol{n}_i + b_{noise,i}. \tag{2.6}$$

Environmental noise is disturbances of the magnetic field that can be the result of background electromagnetic activity (e.g., mobile networks, power line), moving metallic objects (e.g., nearby cars) or biomagnetic signals from the subject itself (e.g., muscle activity or the heart beat). Even neural activity unrelated to the experimental paradigm can act as a source of noise ('brain noise'), masking signals of interest.

2.2.1 Response averaging

In many cases, analyzing neural activity based on a single measurement is not possible due to an insufficient signal-to-noise ratio (SNR). Where possible, neural activity is therefore recorded multiple times and averaged. If the neural activity does not change in time, then it remains unaffected by averaging, while random signals (such as noise and unrelated activity) are reduced in magnitude, thereby increasing the SNR.

In MEG, neural activity is often recorded as a response to some form of sensory stimulation (e.g., tactile, electrical, auditory, or visual input) or conscious action (e.g., moving a finger, opening/closing one's eyes, or speaking). Neural activity can therefore be recorded repeatedly simply by applying the stimulus multiple times or having the subject repeat his/her action.

Evoked neural responses, i.e., responses that are a direct response to a stimulation or action, are phase locked to the stimulation and can therefore be averaged directly using a trigger that is time-locked to the stimulus. To this end, sets of data around

the stimulus - called epochs - are extracted from the recording and averaged. The result is a time-locked average response with increased SNR (see Fig. 2.3).

Induced neural responses are characterized by modulation of spontaneous brain rhythms as a consequence of a stimulation or action. In contrast to evoked responses, induced responses are not phase-locked with respect to the stimulus/trigger event. Averaging induced responses directly would therefore reduce the signal as well as the noise. Instead, induced activity can be averaged by performing time-frequency analysis and averaging the resulting time-frequency spectra (see Fig. 2.3) [18].
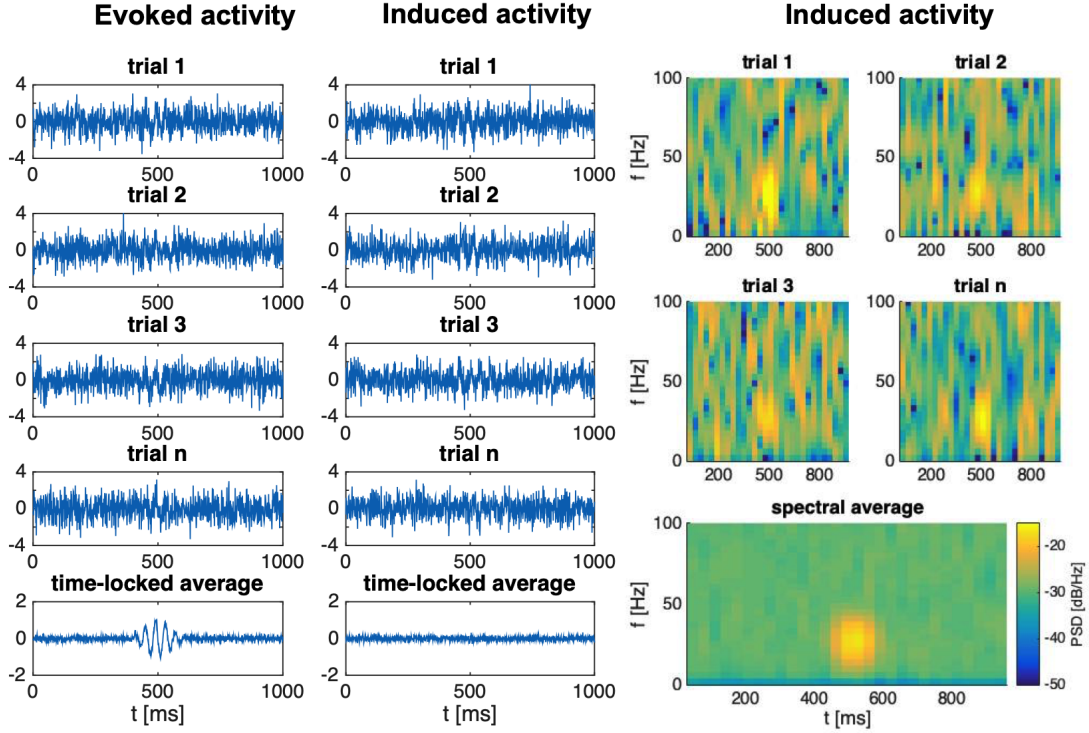

Figure 2.3: Example of evoked (left) and induced response averaging (middle and right). *Left:* Examples of simulated evoked (phase-locked) activity with high noise (SNR∼1) and time-locked average showing improved SNR. *Middle:* Examples of simulated induced (not phase-locked) activity with high noise (SNR∼1) and time-locked average showing no improvement. *Right:* Power spectral density (PSD; estimated with short time Fourier transform) of the same induced activity data and PSD average showing improved spectral SNR. Evoked and induced data were simulated by applying a Gaussian window to a 25 Hz sine signal with constant and random phase, respectively, and adding random, normally distributed noise.

2.2.2 Inverse problem

The magnetic field $\boldsymbol{B}$ is linearly related to the primary current density $\boldsymbol{J}^p$ [11]. Equation (2.5) can therefore be rewritten as:

$$b_i = \boldsymbol{B}(\boldsymbol{r}_i) \cdot \boldsymbol{n}_i = \int_{\boldsymbol{r}'} \boldsymbol{\mathcal{L}}_i(\boldsymbol{r}') \cdot \boldsymbol{J}^p(\boldsymbol{r}')dv, \qquad (2.7)$$

where $\boldsymbol{r}_i$ is the position of the sensor, $\hat{\boldsymbol{n}}_i$ a vector defining the sensitive direction of the sensor and the lead field $\boldsymbol{\mathcal{L}}_i(\boldsymbol{r}')$ describing the sensitivity of sensor i to a source at $\boldsymbol{r}'$.

By approximating the current distribution with a distribution of current dipoles, Eq. (2.7) becomes:

$$b_i = \int_{\boldsymbol{r}'} \boldsymbol{\mathcal{L}}_i(\boldsymbol{r}') \cdot \boldsymbol{Q}(\boldsymbol{r}')\delta(\boldsymbol{r} - \boldsymbol{r}')dv, \tag{2.8}$$

where $\boldsymbol{Q}(\boldsymbol{r})$ is the magnitude of the current dipole at position $\boldsymbol{r}$.

By confining the current dipoles to a discrete set of points G (the source space) the integral in equation (2.8) becomes a finite sum:

$$b_i \approx \sum_{\boldsymbol{r}' \in G} \boldsymbol{\mathcal{L}}_i(\boldsymbol{r}') \cdot \boldsymbol{Q}(\boldsymbol{r}'). \tag{2.9}$$

In matrix notation the forward solution for multiple sensors can be expressed as $\mathbf{b} = \mathbf{L}\,\mathbf{q}$ where $\mathbf{b}$ is an $m \times 1$- column vector representing the recorded magnetic field signals from m sensors, $\mathbf{q}$ is an $n \times 1$- column vector representing the set of n possible current dipoles in G, and $\mathbf{L}$ the $m \times n$ lead field matrix that describes the coupling between each source and sensor.

To determine neural activity from a measured neuromagnetic field distribution (called the inverse problem) $\mathbf{q} = \mathbf{L}^T\mathbf{b}$ has to be solved. Unfortunately, there is no unique solution for a given $\mathbf{b}$. Since the sensors might not pick up the field generated by some sources (e.g., sources oriented perpendicular to the head surface), any neuromagnetic field distribution $\mathbf{b}$ can be explained by a set of sources that generate the observed field distribution plus an arbitrary number of sources whose fields are not detected. Since a magnetic field sensor measures only the sum of the fields generated by all current dipoles $\mathbf{q}$, fields from opposing dipoles in close proximity to one another can furthermore cancel each other out. The inverse problem is thus ill-posed. Solving it requires additional assumptions about the sources.

An intuitive assumption that is shared by many methods is the *a priori* restriction of the source space based on anatomical constraints. Often the source space is confined to a grid of points on the cortical surface, which greatly simplifies the inverse problem.

2.2.3 Solutions to the inverse problem

2.2.3.1 Equivalent current dipoles

The simplest and most restrictive model for solving the inverse problem is the equivalent current dipole (ECD). Herein, one assumes that a single current dipole can explain the observed neuromagnetic fields, i.e., q is zero at all but one point. Using standard optimization approaches, a current dipole can be fitted to the data by minimizing the residual variance between the measured magnetic fields and the ones calculated for a single dipole:

$$\underset{r,q}{\arg\min}\Big(\frac{\sum_i (b_{i,meas} - \mathbf{L}_i\mathbf{q})^2}{\sum_i (b_{i,meas})^2}\Big). \tag{2.10}$$

Similarly, in case of multiple distinct (i.e., spatially separated [11, 19]) sources, multiple dipoles can be fitted to the data; however, in this case, the fitting becomes more difficult and time-consuming with increasing number of dipoles [12].

The ECD approximation places strong *a priori* assumptions about the measured activity - specifically the number of sources contributing to the recorded field distribution. Assuming too few or too many sources can result in missing, incorrectly localizing, or even creating fake, sources. In many more complex MEG experiments, the number of dipoles is not known beforehand, making ECD estimates in these cases unreliable [12]. While methods have been proposed that automatically determine the number of sources required to explain the data, these still face issues related to fitting multiple dipoles (e.g., local minima and high computational demand) and are not widely used [12].

2.2.3.2 Distributed current models

By including additional assumptions, distributed current models constrain the inverse problem in order to try to find a most likely distribution of sources that is able to explain the measured fields. Minimum norm estimates (MNE), the most prominent distributed current model, is based on the assumption that the brain – like many systems in nature – does not waste energy. MNE enables identification of the current distribution with the lowest power, i.e. the distribution with the smallest L_2 norm $||\boldsymbol{J}^p||^2 = \int |\boldsymbol{J}^p(\boldsymbol{r})|^2 dV$ [13], while still explaining a large fraction of the measured neuromagnetic field distribution. MNE also confines the source space to the subspace that is spanned by the lead fields of the sensors G' [13]. By imposing the minimum norm requirement, the inverse problem can be solved uniquely.

MNE does not include assumptions about the number of sources contributing to the observed field distribution other than the (user defined) definition of the source space (which typically includes thousands of sources), making it well suited for analyzing complex or unknown neural activity. Regularization can make MNE more robust against noise by suppressing sources that couple weakly to the sensors [13]. However, MNE tends to overestimate the spatial extent of sources, resulting in many weak sources over a few strong ones [3].

2.2.3.3 Scanning approaches

Scanning approaches iterate through the source space and analyze each potential dipole location independently to determine its contribution to the measured signals. Beamformers, for example, apply spatial filters to the measured data to extract only the signals that originate from a given source location [14]. Based on the spatially filtered data, the current dipole strength at the target location can be estimated. Beamformers are sensitive to errors in head-modeling as well as strongly correlated sources [3, 12].

The multiple signal classification (MUSIC) method uses decomposition of auto-correlated data to separate signal and noise subspaces based on the eigenvalues of the autocorrelated data [20]. A single dipole is then scanned over the discrete source space (e.g., a grid over the cortical surface). At each point the correlation between

the forward solution for a dipole at this location and the signal subspace is computed. High correlation values indicate the dipole's contribution to the signal is significant [21]. The dipole locations can then be refined with a non-linear fit of the identified dipoles. By recursively refining the signal subspace based on sources that have previously been identified and projecting it onto (i.e., correlating it to) the forward model, MUSIC can be further improved. In addition to automating the search for high correlations in the source space, such a recursively applied and projected MUSIC (RAP-MUSIC) approach is more robust to noise [22].

2.2.4 Co-registration

All the above mentioned solutions to the inverse problem presume knowledge of the anatomy of the subject's head and its position relative to the sensors (and vice versa). MEG, however, provides information only about the magnetic field at the sensors' positions. Localizing neural activity in the brain therefore requires combining MEG data with structural data, e.g., from MR images. To this end, MEG and structural data have to co-registered, i.e., the positions and orientations of the sensors with respect to the anatomy must be established for a given recording.

In today's commercial full-head MEG systems, co-registration is typically performed with small, magnetic dipole-like (so-called head position indicator, HPI) coils attached to the subject's head [23]. First, structural information about the head surface as well as the location of the coils thereon are obtained. This can be done with an optical 3D scan [24–26] or by manually digitizing points using an electromagnetic, ultrasound, etc. position tracker [27]. Once the head surface and coil locations are known, they can be related to the structural image by extracting the head surface from the structural image and fitting the two head surfaces to each other, e.g., using an iterative closest point (ICP) algorithm.

When the subject is placed in the MEG system, the HPI coils are driven with sinusoidal currents at different frequencies with amplitudes strong enough to ensure sufficiently high SNR. Since the coil signals are separated in frequency, the magnetic field generated by each coil can be extracted from the sensor signals using spectral analysis (e.g., Fourier transform). The amplitudes can then be used to localize the coils within the MEG system (if the locations of all the sensors relative to each other are known) by fitting magnetic dipoles to the data. Finally, the coils localized by the MEG system can be related to the coil locations from the structural scan - and consequently to the structural image. A schematic representation of the standard co-registration procedure is shown in Fig. 2.4.
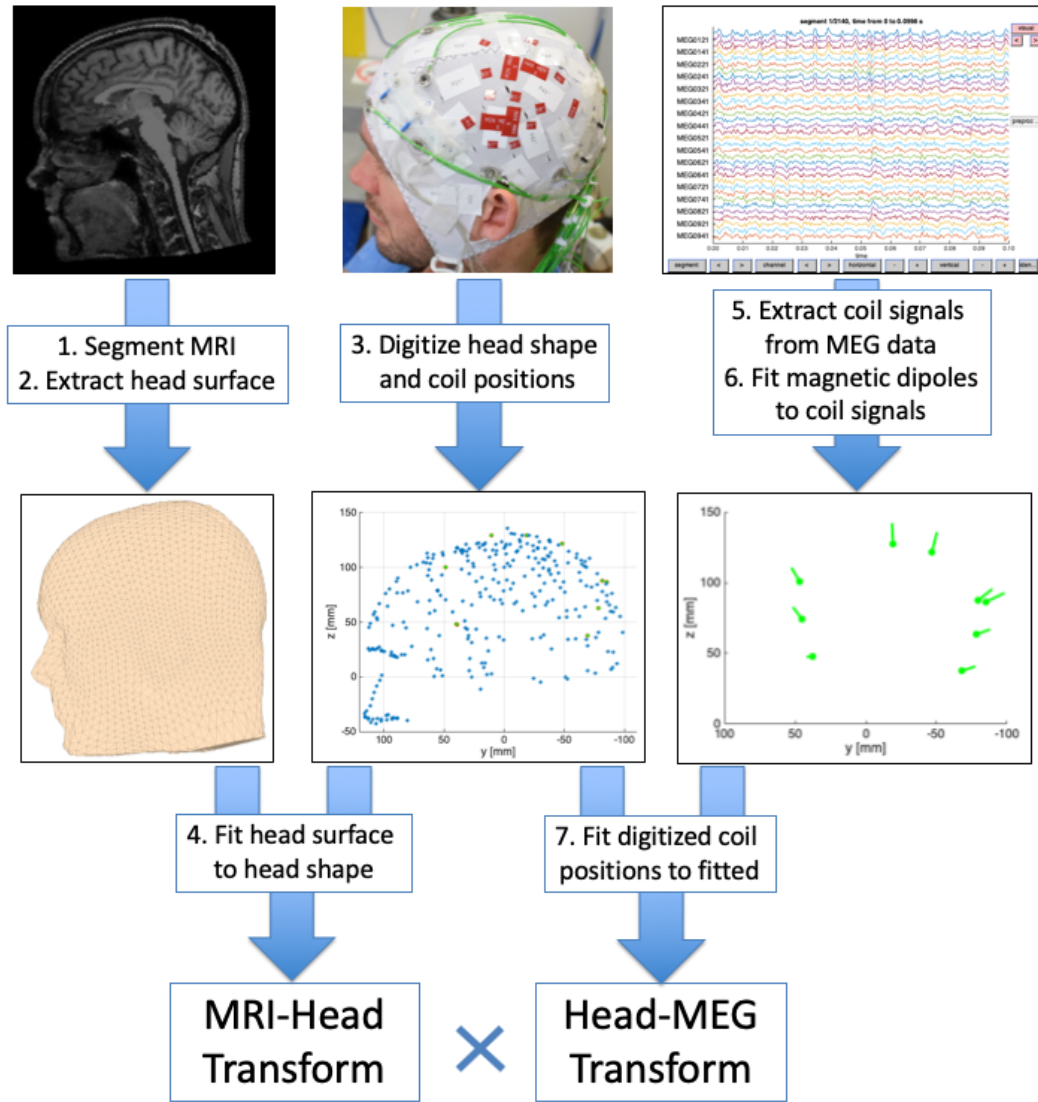
Figure 2.4: Head localization procedure for co-registration of MEG and MRI data.

2.3 SQUIDs

The neuromagnetic fields measured in MEG are typically on the order of femtotesla up to a few picotesla. Measuring such low fields requires extremely sensitive magnetic field sensors. The first MEG recordings were performed by David Cohen with a ($\sim$90 $\times$90 mm^2) 1-million-turn coil with ferrite core [4]. Due to the large size of the sensor, field distortions from the ferrite core, and high noise ($\sim$600 fT$_{RMS}$ at 10 Hz [4]), MEG with such sensor technology was not practical. Soon after, Cohen therefore switched to a newly-developed sensor technology - superconducting quantum interference devices (SQUIDs) - which are still the most widely used sensor type in MEG [3, 28].

2.3.1 Superconductivity

Discovered in 1911 by Heike Kamerlingh Onnes, superconductivity is a state that occurs in some materials when they are cooled below a critical temperature T_c. Transition to superconductivity is characterized by two phenomena in the material - the disappearance of electrical resistance and the expulsion of magnetic fields (Meissner effect). In addition to a material-specific critical temperature, superconductors are characterized by a critical current density J_c as well as magnetic field H_c above which superconductivity breaks down. Conventional superconductors are primarily metals with T_c below 30 K. According to the prevailing theory on superconductivity in these materials, the Bardeen-Cooper-Schrieffer (BCS) model, superconductivity occurs at low temperatures when electrons form bound pairs (Cooper pairs) as a result of electron-phonon interactions at low temperatures [29].

In 1986, high-T_c superconductivity was discovered in cuprates [30]. This new class of superconducting materials exhibit significantly higher T_c (as high as ∼130 K [31]), offering new possibilities in the application of superconductors (e.g., liquid nitrogen-cooled operation). High-T_c superconductors are type II superconductors, meaning that above a certain magnetic field H_{c1} magnetic field can penetrate the material, forming quantized vortices wherein non-superconducting material is surrounded by a circulating supercurrent (Abrikosov vortices). With increasing magnetic field, more such vortices form until superconductivity is broken throughout the material at the upper critical field H_{c2} [32].

2.3.2 Josephson Junctions

A Josephson junction is a small, insulating or weakly conducting connection between two superconductors. If the weak link is narrow enough for the superconducting wave functions to overlap through it, then a superconducting current can tunnel across it [33]. The superconducting tunneling current depends on the phase difference across the junction (called the dc Josephson effect):

$$I_s = I_0 \sin(\delta), \tag{2.11}$$

where I_0 is the critical current of the junction, I_s the superconducting current and δ the phase difference of the superconducting wave function across the junction [34].

Practical Josephson junctions are usually described using a resistively- and capacitively- shunted junction (RCSJ) model (see Fig. 2.5), where a capacitance C, a resistance R, and a current noise source I_n are modeled in parallel with the ideal junction. The current through a RCSJ junction is given by:

$$I = C\frac{\Phi_0}{2\pi}\ddot{\delta} + \frac{1}{R}\frac{\Phi_0}{2\pi}\dot{\delta} + I_0 \sin(\delta) + I_n, \tag{2.12}$$

where $\Phi_0 = \pi\hbar/e$ i the flux quantum and $\dot{\delta}$ and $\ddot{\delta}$ the first and second derivatives of the time-dependent phase [34].

Below I_0, the current through the junction is entirely superconducting (called the supercurrent), resulting in 0 voltage over the junction. Above I_0 a normal current begins to flow across the junction in addition to the supercurrent and a DC voltage

appears across the junction (in addition to a high-frequency AC voltage with frequency $f \sim 484 \cdot 10^{12}$ Hz/V that we can neglect here). At $I \gg I_0$ the superconducting contribution becomes negligible and the junction shows a linear current-voltage relation. The current-voltage characteristic of a so-called overdamped Josephson junction (where $(R/2)^2 > L/C$) is shown in Fig. 2.5-b.
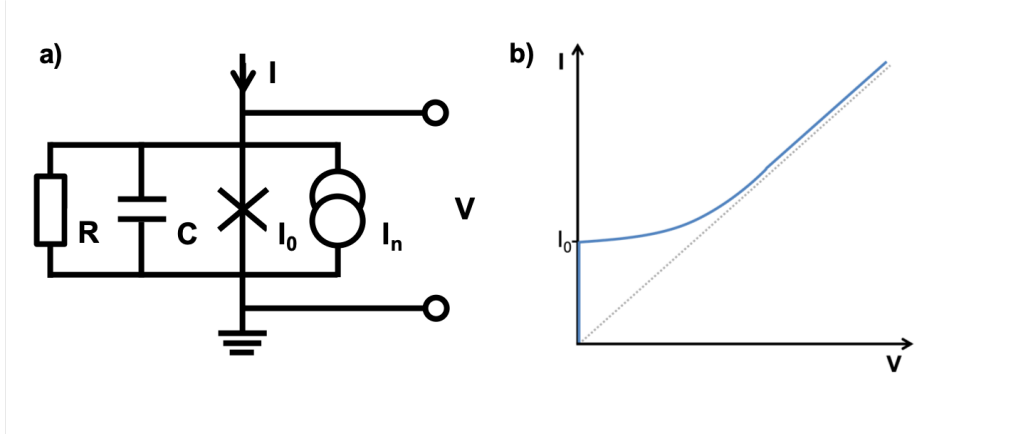

Figure 2.5: Resistively- and capacitively- shunted junction (RCSJ) model (adapted from [34]). a) Schematic of an RCSJ-model Josephson junction. A cross symbolizes the Josephson junction. b) Blue: normalized current-voltage characteristic of an overdamped RCSJ-like Josephson junction; grey dotted line: current-voltage characteristic of simple resistor equal to R. Note the convergence of the junction's current-voltage characteristic to that of a simple resistor $I \gg I_0$.

Josephson junctions can be made in a variety of ways, such as physical restriction of the superconductor (e.g., point contact or nano-bridges), insulating or normally conducting separation layers, or local defects in the superconductor material (e.g., ion irradiation or a grain boundary in crystalline superconductors). The fabrication technique affects the junction parameters.

2.3.3   Dc SQUIDs

As the SQUIDs used in MEG are almost exclusively dc SQUIDs, we will focus on those in the following. A dc SQUID generally consists of a superconducting ring interrupted by two similar Josephson junctions. A schematic of such a SQUID can be seen in Fig. 2.6.

The superconducting wave function has to be single valued anywhere inside a superconductor. As a consequence, the total flux threading a superconducting loop ϕ (i.e., the sum of externally applied flux and flux generated by induced screening currents) is quantized with the flux quantum:

$$\phi = \phi_e + LJ = n\Phi_0, \tag{2.13}$$

where ϕ_e is the externally applied flux, J the induced supercurrent, L the inductance of the superconducting loop, and n an integer [34].
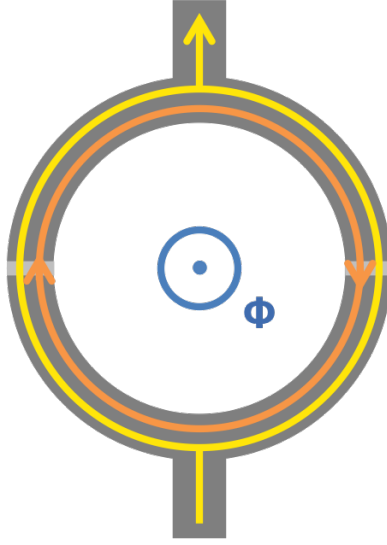
Figure 2.6: Schematic of a dc SQUID consisting of a superconducting ring and leads (dark grey) interrupted by two Josephson junctions (light grey). Externally applied bias current I and circulating current J induced by external flux (ϕ, blue, pointing out of the page) are shown in yellow and orange, respectively. Note that the supercurrent flows such that it induces a field/flux in the SQUID loop that opposed the external flux.

As a result of this flux quantization, the phase differences across the two junctions of a SQUID differ by [35]:

$$\delta_2 - \delta_1 = 2\pi\frac{\phi}{\Phi_0}. \tag{2.14}$$

By combining (2.14) and (2.11), we can derive the supercurrent through the SQUID [35]:

$$I_s = 2I_0 \cos(\pi\frac{\phi}{\Phi_0})\sin(\delta_0) = I_c \sin(\delta_0), \tag{2.15}$$

where I_c is defined as the critical current of the SQUID and $\delta_0 = (\delta_1 + \delta_2)/2$ (for detailed derivations of (2.13), (2.14), and (2.15) see [34, 35]).

The supercurrent is thus modulated by applied flux. For integer multiples of the flux quantum, the SQUID behaves like a Josephson junction with twice the critical current of the individual junctions, whereas for $\phi \neq n\Phi_0$ the critical current is reduced (Fig. 2.7-left). The modulation depth of I_c depends on the SQUID inductance L, with lower SQUID inductances yielding higher modulation depth (Fig. 2.7 - top right) [34].

If the SQUID is current biased (i.e., with a fixed I) at, or slightly above, the maximum critical current $I > 2I_0$, the modulation of the current with flux effectively results in a Φ_0-periodic voltage modulation across the SQUID (Fig. 2.7 - bottom right).
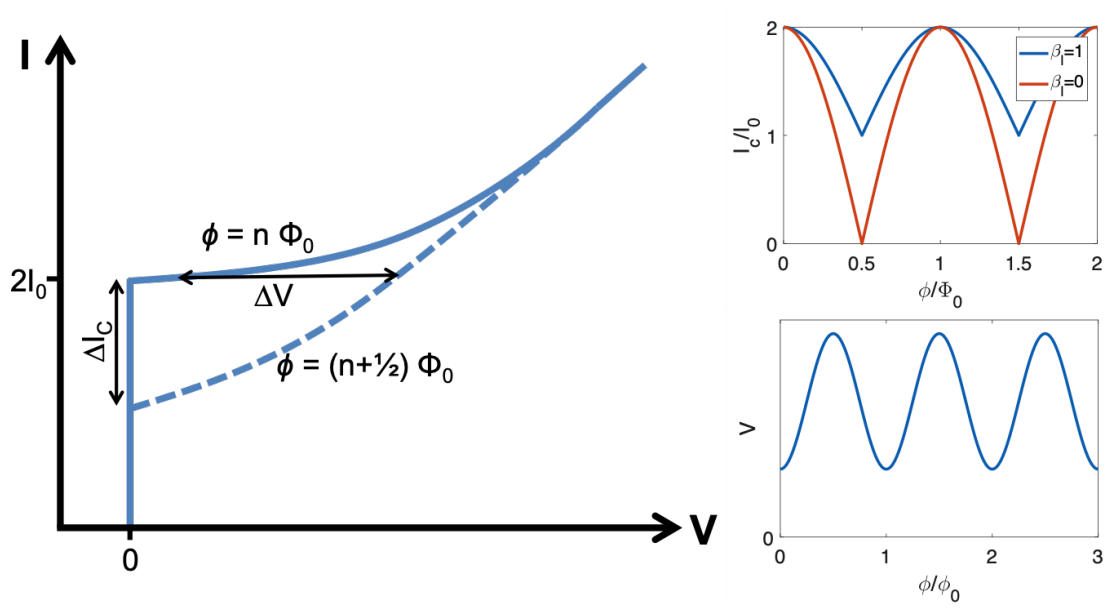
Figure 2.7: Current-voltage-flux characteristics of an ideal SQUID. *Left:* Current-voltage dependence of a SQUID for flux equal to integer (i.e., $n\Phi_0$) and half-integer (i.e., $(n + 1/2)\Phi_0$) multiples of the flux quantum threading the loop ($n = 0, 1, 2, ...$). *Top right:* Critical current as a function of flux for different SQUID inductances (expressed here in the form of the dimensionless screening parameter $\beta_c = 2LI_c/\Phi_0$). *Bottom right:* Voltage-flux dependence for a fixed current $I = 2I_0$.

2.3.4 Noise

Noise in SQUIDs can be conceptually divided into white and 1/f-noise. White noise is broadband noise with constant power over all frequencies and results from thermal fluctuation in the Josephson junctions [34]. At low frequencies, which are of interest in MEG, the noise of SQUIDs is often dominated by noise that decreases with the inverse of the frequency (called 1/f- or flicker noise). The main sources of 1/f-noise in high-T_c SQUIDs are fluctuations of the critical current that are a result of defects in the Josephson junctions and thermally activated movements of flux vortices [34]. Flux vortices can hop between different pinning cites (e.g. defects in the film) when their thermal energy is high enough to overcome the pinning force. Such hopping induces random telegraph noise in the SQUID. Narrow linewidth, good film quality (of the superconducting material), and artificial pinning centers can help reduce vortex formation and hopping, respectively [34]. Slow cooling in low magnetic field and avoiding fast, strong changes in the applied field can help prevent the formation of flux vortices in a given SQUID [34].

2.3.5 Readout electronics

Since the periodic nature of its voltage-flux relation would limit the range of a SQUID magnetometer to one Φ_0, they are usually operated in a so-called flux-locked loop (FLL). In FLL operation, the voltage signal of the SQUID is amplified, integrated, and inductively fed back to the SQUID (e.g., with a small feedback coil)

[34, 36]. Fig. 2.8 shows a simplified FLL circuit schematic. Small changes of the external flux result in changes of the SQUID voltage from the working point. The change in voltage is amplified, integrated and fed to the feedback coil through the feedback resistor R_{fb}. If configured correctly, the flux induced by the feedback coil (L_{fb}) cancels the change in external flux, bringing the SQUID back to the working point, thus closing the negative feedback loop. Within the limits of the electronics (in terms of speed and maximum feedback current), the SQUID is kept at the working point. The output of the integrator V_{out}, i.e., the feedback voltage required to maintain the working point, is linearly proportional to the change in external flux and serves as the output signal of the FLL. For maximum sensitivity, the working point is chosen where the derivative of the flux-voltage relation of the SQUID is maximum.
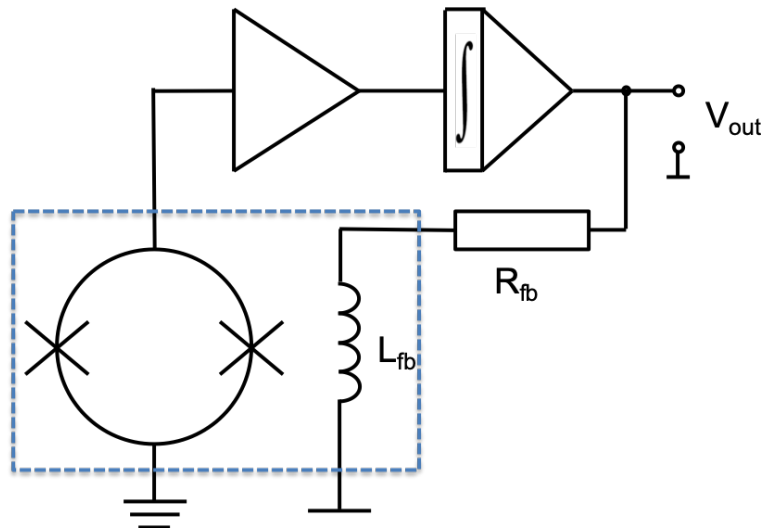

Figure 2.8: Simplified schematic of a flux locked loop circuit. Blue box marks components at cryogenic temperatures (i.e., below the T_c of the superconducting material.

Further improvements can be made to the electronics to suppress noise. In a technique called bias reversal, the polarity of the bias current is switched rapidly. As a result, fluctuations of the critical current and resistance that have opposite phase at positive and negative bias are subtracted, reducing the overall noise. This technique is especially effective at reducing 1/f-like noise that is generated by critical current fluctuations [36].

2.3.6 SQUID magnetometers

SQUIDs are very sensitive flux sensors. However, the small area (typically on the order of a few tens of μm^2) encompassed by a SQUID-loop makes them poor magnetometers by themselves. However, there are ways to improve the field sensitivity of a SQUID. A large pickup loop can be directly coupled to the SQUID (as seen in Fig. 2.9-left). The field picked up by the large loop induces a current that couples into the SQUID-loop - thus the area of the magnetometer is effectively increased.

The increase in effective area is determined by the coupling between the loops that is given by the ratio of their inductances:

$$A_{eff} = A_{eff}^{SQ} + \frac{L_m}{L_{pk}} A_{eff}^{pk} \approx \frac{L_m}{L_{pk}} A_{eff}^{pk}, \tag{2.16}$$

where L_m is the mutual inductance of the SQUID and pickup loop, A_{eff}^{SQ} the effective area of the SQUID, and A_{eff}^{pk} and L_{pk} the effective area and inductance of the pickup loop [37]. SQUID magnetometers with directly coupled pickup loops suffer from a large inductance mismatch between L_m and L_{pk}. Eq. 2.16 shows the importance of inductance matching between the pickup loop and SQUID - a large inductance mismatch can undo the advantage of the geometrically larger pickup loop.

Instead of directly coupling a pickup loop, a second, smaller input coil connected to the pickup loop can be used to couple field inductively to the SQUID (see Fig. 2.9-right). Such a flux transformer (FT) can couple fields more effectively to the SQUID than a directly coupled pickup loop. The effective area for such a setup can be approximated by

$$A_{eff} = A_{eff}^{SQ} + \frac{L_m}{L_i^{FT} + L_{pk}^{FT}} A_{eff}^{FT} \approx \frac{\alpha}{2} \sqrt{\frac{L_{SQ}}{L_{pk}^{FT}}} A_{eff}^{FT}, \tag{2.17}$$

where L_{SQ} is the SQUID inductance, L_{pk}^{FT} and L_i^{FT} the inductances of the flux transformer pickup loop and input coil, A_{eff}^{FT} its effective area, and $L_m = \alpha\sqrt{L_{SQ}L_i^{FT}}$ the mutual inductance between the SQUID and the flux transformer input coil with the coupling coefficient α [38]. The effective area is maximum when $L_i^{FT} = L_{pk}^{FT}$ [38]:

$$A_{eff} \approx \frac{\alpha}{2} \sqrt{\frac{L_{SQ}}{L_i^{FT}}} A_{eff}^{FT}. \tag{2.18}$$

Since it is easier to match the flux transformer's input coil inductance to the SQUID inductance, flux transformers are able to couple flux more effectively to a SQUID, thereby resulting in more sensitive magnetometers.
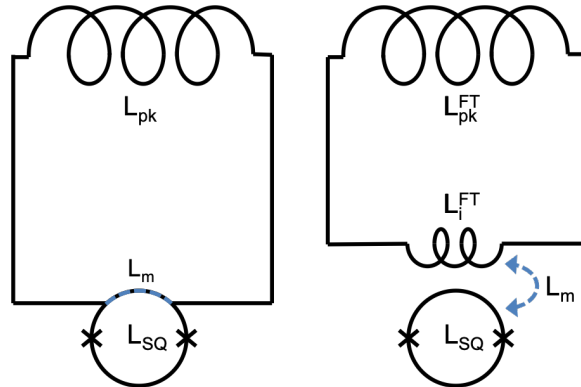

Figure 2.9: SQUID magnetometer with directly (left) and inductively (right) coupled pickup loop, respectively.

In addition to increasing the effective area of the SQUID, the pickup coil - independently if it is coupled directly or inductively - can be configured to measure the

local gradient of the field. A planar figure-of-eight coil design, for example, effectively couples the difference in magnetic field threading the two loops to the SQUID - which corresponds to the field gradient between the two loops. Similarly, axial as well as higher order gradiometers can be constructed.

2.3.7 High-T_c SQUIDs

Soon after the discovery of high critical temperature (high-T_c) superconductors in the 1980s [30] the first SQUIDs using these materials were developed. Today, most high-T_c SQUIDs are made from $YBa_2Cu_3O_{7-x}$ (YBCO). YBCO is a ceramic with highly anisotropic crystal structure. Transport properties are strongly dependent on crystal direction and affected by oxygen content (7-x). YBCO shows a $T_c \approx 92$ K depending on the oxygen stoichiometry [31]. High quality YBCO films can be grown on substrates with similar lattice parameters (e.g., $SrTiO_3$ (STO) or MgO) using pulsed laser deposition (PLD), dc-sputtering, or chemical vapor deposition (CVD). The grown film then follows the orientation of the substrate. Typical film thicknesses are on the order of a few hundred nanometers.

As a result of the materials' structural differences, SQUIDs based on low- and high-T_c superconductors employ very different types of Josephson junctions. The most common Josephson junctions used for high-T_c SQUIDs are step-edge and bicrystal junctions. Step edge junctions are obtained by growing the YBCO on a substrate with a step on it; weak links form where crystals with different growth orientation, i.e., at the edges, meet. Similarly, a bicrystal junction can be made by growing YBCO on a bicrystal substrate, i.e., a substrate that consists of two connected crystals with different lattice orientations, forming a so-called grain boundary between them. The lattice misorientation between the films grown on the two crystals results in a weak link at the grain boundary.

Producing multilayer devices from high-T_c materials is challenging due to their strong anisotropy and dependence on the crystal structure. Flux transformers, for example, require multilayer technology to realize the crossover and interconnects needed to make the coil that couples into the SQUID. Realizing flux transformers for high-T_c SQUIDs is technologically challenging and often results in excess 1/f-noise generated at the crossover/interconnects [34, 39]. Due to their superior flux coupling (c.f., §2.3.6) such devices can, however, reach significantly lower white noise levels than their directly-coupled counterparts [38–40]. Magnetometers using flux transformers can be realized as flip-chip or integrated devices [38, 40, 41].

2.4 Cryostat

SQUIDs require cryogenic temperatures to operate bwlow the T_c of the material from which they are fabricated. Typically this is achieved by cooling them with liquid helium (LHe, boiling temperature ≈ 4 K) or - in case of high-T_c SQUIDs - liquid nitrogen (LN_2, boiling temperature ≈ 77 K). Liquid coolants are preferable in MEG as they produce less vibrations, and thus generate less magnetic noise, than other cooling methods, many of which require pumps and other moving parts. To protect the subject from the extreme cold (and the SQUIDs from room temperature),

the SQUIDs are placed inside a cryostat that thermally insulates them from the room-temperature environment. MEG cryostats typically consist of a double-walled structure with a vacuum space that provides most of the thermal insulation. Layers of superinsulation foil are often added to minimize radiation heating. In order to minimize the distance to the subject's head, the SQUIDs are usually placed as close to room temperature as thermal insulation requirements allow and arranged to match the shape of the human head [42, 43] (see Fig. 2.10).
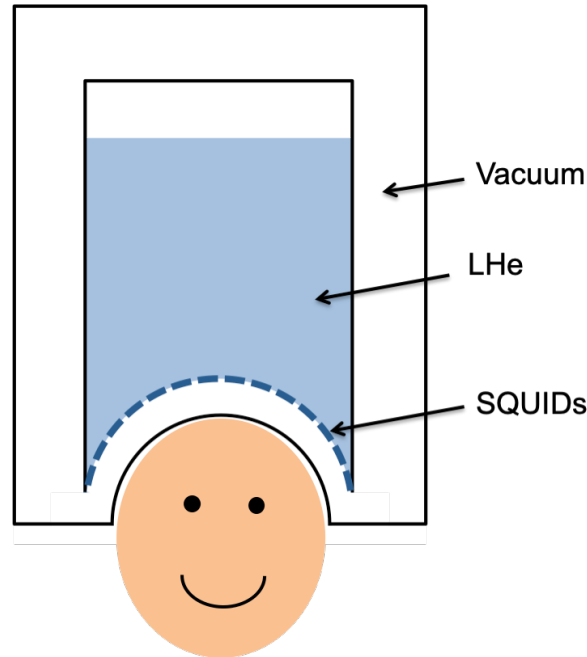

Figure 2.10: Simplified schematic of a conventional MEG cryostat with LHe-cooled low-T_c SQUID sensors.

Commercial, state-of-the-art MEG systems like the TRIUX (MEGIN Oy, Helsinki, Finland) and CTF MEG 275 (CTF MEG, Coquitlam, BC, Canada) consist of a large LHe-cooled cryostat with a helmet-shaped tail containing hundreds of low-noise low-T_c SQUIDs. During recordings, the subject is positioned with his or her head inside the helmet-shaped cryostat tail.

2.5 Magnetic shielding

Typical neuromagnetic signals in MEG are on the order of a few tens to several hundreds of femtotesla – roughly 9 orders of magnitude lower than the earth's magnetic field. In addition to the earth's magnetic field, electromagnetic background noise from cars, wireless communication, power lines, etc. are constantly present in typical, urban environments where MEG recordings are primarily performed. In order to measure neuromagnetic signals, such background fields have to be shielded. To this end, MEG recordings are typically performed inside a magnetically shielded room (MSR). MSRs are rooms enclosed by layers of high permeability metal (e.g., mu-metal) to provide shielding at low frequencies (<100 kHz) as well as normal

metal (typically aluminum and/or copper) for eddy-current shielding that performs better at higher frequencies (>10 kHz) [12]. If passive shielding is not sufficient, then active field compensation can be used to reduce remnant fields inside an MSR [44, 45]. Active shielding uses coils controlled with magnetic field sensors to cancel external fields [11].

Commercial MSRs like the VACOSHIELD (Vacuumschmelze GmbH, Hanau, Germany) employ 2 or 3 mu-metal, combined with 1 or 2 aluminum, layers and reach shielding factors on the order of 200-2000 at 1 Hz within a volume of ∼4 m × 3 m × 2 m. Most MSRs used for MEG today are cuboid rooms with >2 m wall length to allow enough space to comfortably fit the MEG device as well as the subject and stimulation equipment inside.

3

Theoretical studies for on-scalp MEG

In this chapter, the general theory behind on-scalp MEG is introduced, providing the motivation for the experimental work in this thesis. This theory is then applied to guide the design of full-head on-scalp MEG systems. Finally, a method for co-registration in such systems is introduced and tested in simulations.

3.1 Introduction

In conventional MEG, liquid helium-cooled low-T_c SQUIDs are used to sample the magnetic field. While they achieve very high sensitivity, low-T_c SQUIDs also operate at extremely low temperatures ($\sim$4 K). As described above, such an extreme temperature difference between the sensors and the subject's head at room temperature necessitates $\sim$2 cm of thermal insulation (including vacuum space, radiation shields, mechanical support, etc.). Since magnetic fields decrease in magnitude as a function of distance from their source (eq. 2.4), this separation limits the measurable magnetic signal at the sensor locations.

The emergence of new sensor technologies, such as high-T_c SQUDs and optically pumped magnetometers (OPMs), with comparable sensitivities but less extreme operating temperatures, offered the chance to overcome this issue. High-T_c SQUIDs, for example, can operate at 77 K, at which $\sim$1 mm of insulation (e.g., a vacuum supporting window and thin vacuum space) can suffice for thermal insulation [9]. The magnetometers can therefore be placed much closer to the scalp. This is commonly referred to as "on-scalp". At the much closer distance to the subject's head, the sensors can measure significantly higher signals - which can make up for the often higher noise of high-T_c SQUIDs, as compared to low-T_c ones. Depending on the depth of the source of interest, the signals can be 2 to 6 times higher [10]. The gain in signal is generally higher for shallow sources since the relative change in distance between sensors and sources is bigger compared to deep sources (Fig. 3.1).

On-scalp MEG brings additional advantages. The higher operating temperature of the sensors and resulting simpler thermal insulation offers new possibilities in terms of system design. Conventional, liquid helium-cooled MEG systems are mostly restricted to arrays with fixed sensor positions housed in a single, helmet shaped cryostat due to the demanding thermal insulation. Since a system is typically designed to fit the majority of the population, i.e., the helmet has to be big enough to fit the
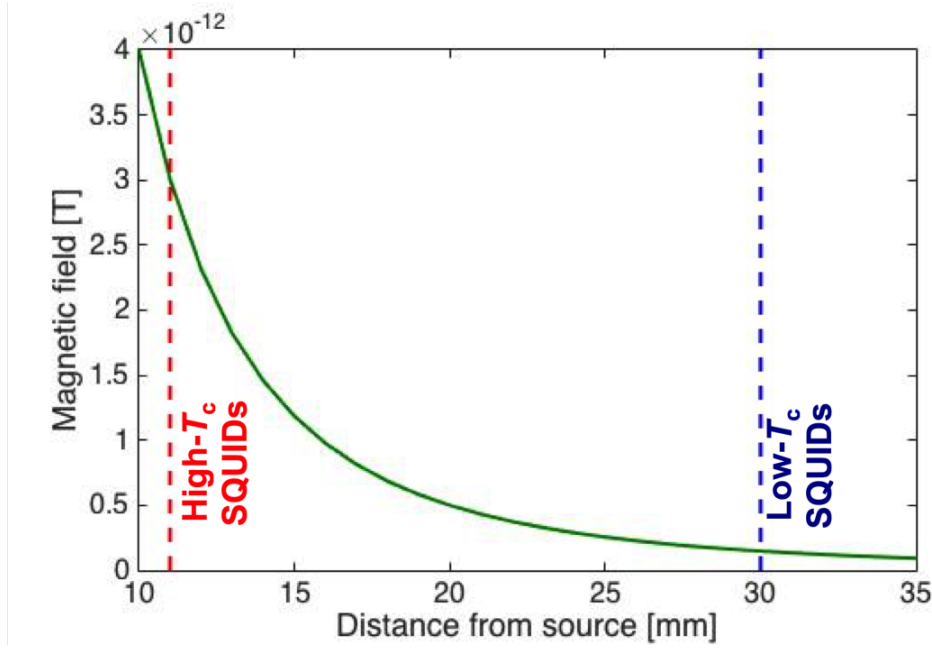
Figure 3.1: Magnetic field as a function of distance from a current dipole. Typical separation from a source 10 mm below the head surface for liquid helium-cooled low-$T_{\rm c}$ SQUIDs ($\sim$ 4.2 K) and liquid nitrogen-cooled high-$T_{\rm c}$ SQUIDs ($\sim$ 77 K) are marked by blue and red dotted lines, respectively.

majority of the population, in many cases a significant fraction of the sensors are even more than 2 cm away from the subject's head. This is especially pronounced in young children and the reason why a few systems dedicated for children have been developed over the years [44, 46, 47]. Conversely, subjects with a head size significantly above average can simply not fit into the helmet, making MEG recordings on them impossible. The reduced thermal insulation of on-scalp sensors means that sensor housings can be made much smaller. As a result, multiple small units (in the case of high-$T_{\rm c}$ SQUID cryostats) housing single or small groups of sensors can be placed close to each other to form a full-head MEG system. Moving the individual units or cryostats then allows modifying the shape of the sensor array: it can be adjusted to different head shapes and sizes to ensure minimal distance to the head for all the sensors.

The general formula (in Cartesian coordinates) for the radial component of the magnetic field arising from a current dipole $\vec{Q}$ located at $\vec{R}$ inside a homogeneous sphere (c.f., Fig. 3.2) is given by:

$$B_r = \frac{\mu_0}{4\pi} \frac{\vec{Q}}{|\vec{r} - \vec{R}|^2} \left(\frac{\vec{r} - \vec{R}}{|\vec{r} - \vec{R}|} \times \frac{\vec{r}}{|\vec{r}|} \right), \tag{3.1}$$

where $\vec{r}$ denotes the sensor location [48].

Fig. 3.3 shows the radial field B_r generated by a current dipole $\vec{Q} = (0, 10, 0)$ nAm at $\vec{R} = (0, 0, 0.06)$ m inside a sphere with radius 8 cm (approximating the head). When coming closer to the head, the neuromagnetic field patterns become
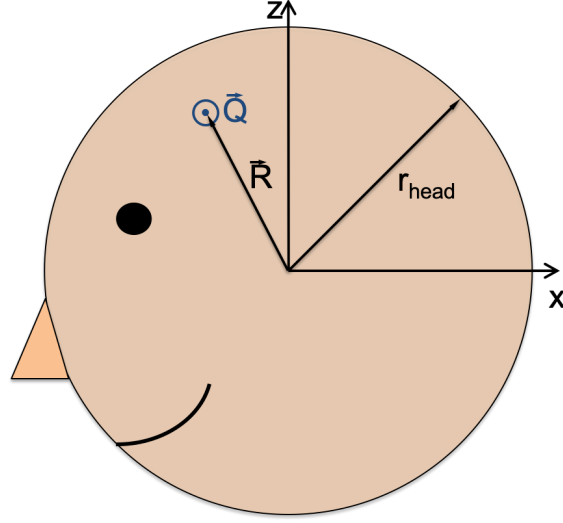
Figure 3.2: Sketch of a current dipole inside a head approximated by a homogeneous sphere.

more focal. The field maximum and minimum of a single dipole current move closer together while spatial gradients become higher in magnitude.
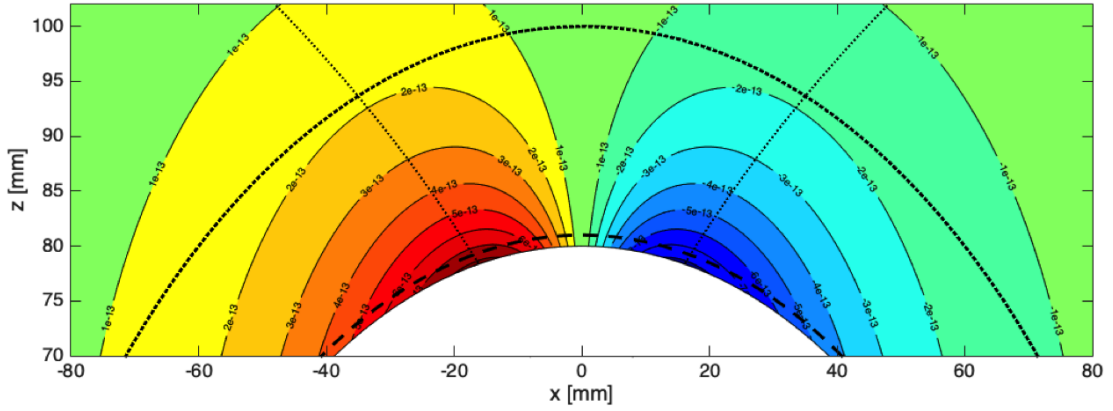

Figure 3.3: Radial magnetic B_r field outside a spherical head with $r_{head} = 80$ mm (white) generated by a current dipole ($Q = 10$ mAm) located 20 mm beneath the surface ($R = 60$ mm). Thick dotted and dashed lines mark the typical separation from the scalp for low-T_c ($r = 20$ mm) and high-T_c SQUIDs ($r = 1$ mm). Thin, dotted lines show the position of the field extrema as a function of r.

We can convert 3.1 in the case of a dipole $\vec{Q} = (0, Q, 0)$ at $\vec{R} = (0, 0, R)$ to spherical coordinates for the measurement location (r, θ, ϕ)

$$B_r = \frac{\mu_0}{4\pi} \frac{Q \sin\phi}{r^2} \rho \frac{\sin(\theta)}{(1 - 2\rho\cos(\theta) + \rho^2)^{3/2}} \tag{3.2}$$

where $\rho = R/r$. The polar and azimuthal angles θ_{max} and ϕ_{max} at which the absolute

23

magnetic field amplitude is maximum (i.e., the field extrema) are given by

$$\cos(\theta_{max}) = \frac{1}{2\rho}(\sqrt{1 + 14\rho^2 + \rho^4} - (1 + \rho^2)) \qquad (3.3)$$

and $\phi_{max} = \pm\pi/2$ [48].

In the case of a dipolar pattern, like that of a single current dipole, the highest spatial frequency is determined by the arc distance between the field extrema

$$f_{max} = \frac{1}{2r2\theta_{max}}. \qquad (3.4)$$

Fig. 3.4 shows the maximum spatial frequency f_{max} as a function of distance from the scalp for different source depths. As expected, f_{max} increases significantly when moving closer to the head surface. Higher spatial frequencies are advantageous because they can enable distinguishing finer details within neuromagnetic field patterns than previously possible - such as two separate, but close sources that would otherwise effectively appear as one. The combination of higher focality and signal gain could further enable measuring weaker sources, e.g., resulting from fewer synchronously firing neurons. On-scalp MEG could thus achieve higher spatial resolution compared to conventional MEG.
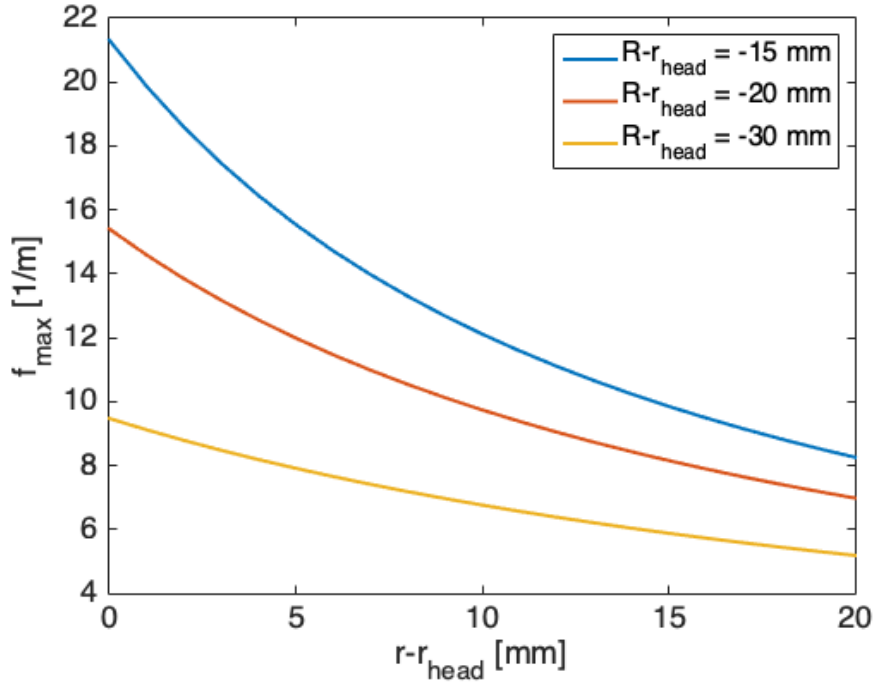

Figure 3.4: Maximum spatial frequency as a function of sensor distance from the scalp ($r - r_{head}$) for different source depths $R - r_{head}$.

However, high spatial frequencies also means that on-scalp MEG systems require higher spatial sampling than conventional systems if they are to resolve field patterns on the same level or better. Similar to signal sampling in the temporal domain, the spatial sampling frequency f_s needs to equal to or exceed the Nyquist frequency, i.e.,

$f_s \geq 2f_{max}$, in order to avoid aliasing. In the example shown here, this means that sampling the field of a current dipole located 15 mm below the scalp (Fig. 3.4, blue line) at 1 mm distance from the scalp requires a sampling frequency of $>40 \frac{1}{m}$ or a sensor-to-sensor spacing of <25 mm. Resolving closely-separated sources requires even lower sensor-to-sensor spacing.

This phenomenon (i.e., on-scalp MEG requiring higher spatial sampling as compared to conventional MEG) is supported by previous theoretical studies that show how using small, densely packed sensors, on-scalp MEG can extract more information from a given subject (even with higher sensor noise), as compared to the state-of-the-art [49].

3.2 Evaluation of full-head on-scalp MEG systems

Because of the aforementioned differences compared to conventional MEG, it is not straightforward to predict how an optimal full-head on-scalp system would look like. Such a system would, for example, have to account for the increased spatial frequencies that are expected and - in case of flexible arrays - the dimensions of sensor housings. Furthermore, since subjects can differ significantly from one another, there is no way to construct an optimal system based on field projections of a known source space (a problem that conventional MEG faces as well). One can instead compare different system designs to each other using a variety of metrics [7, 8].

We therefore designed several distinct full-head systems and compared them to each other as well as to a state-of-the-art conventional MEG system (described in detail in Paper I). In order to see the effects of subject variability, we simulated the systems for two subjects with very different head size: a 35 year old male adult and a 2 year old child.

3.2.1 MEG system designs

The sensor array of the commercial 306-channel TRIUX system (MEGIN Oy, Helsinki, Finland) was used as a point of reference for comparing with our on-scalp designs. For simplicity, we regarded only the magnetometers of the TRIUX, resulting in 102 sensor locations distributed around the surface of a fixed size helmet that was designed to fit the majority of the population. The TRIUX has 26 mm × 26 mm low-T_c SQUID magnetometers (on 28 mm × 28 mm chips) that reach white noise levels of 3 fT/Hz$^{1/2}$ [50]. The sensors are separated from the outer surface of the helmet by approximately 2 cm of thermal insulation.

The on-scalp systems were designed using 8 mm × 8 mm high-T_c SQUID magnetometers (on 10 mm × 10 mm chips). We assumed white noise levels of 50 fT/Hz$^{1/2}$ for the sensors, which was typical for our bicrystal SQUID technology [9]. Since they are high-T_c SQUIDs, thermal insulation and cryostat walls have to be taken into account when designing systems consisting of multiple cryostats (e.g., flexible systems). We assumed 1 mm of vacuum space plus 4 mm of cryostat walls as the minimum distance between sensors in different cryostats, as well as 1 mm minimum distance between sensors in the same cryostat.

Three full-head on-scalp MEG systems were designed based on different guiding ideas. The first system is closely related to the TRIUX system. Sensors were distributed as densely as possible at 1 mm separation from the outer surface of the TRIUX helmet - resulting in a total of 631 sensors. The second system was designed as fully flexible, meaning each sensor was housed in an individual cryostat. Due to the sensor housing, this meant larger distances between sensors. The number of sensors depended on the size of the head - in case of the adult we were able to distribute 214 sensors over the head, in case of the child, 161 sensors. The sensors were separated from the head surface by 1 mm. As a compromise between density and flexibility, the third system used multiple cryostats, each containing seven densely packed sensors. Within each cryostat, the sensors are fixed relative to each other and 1 mm separated them from the subject's head surface. As in the fully flexible system, the number of sensors depends on the size of the subject's head. A total of 30 and 25 such 7-channel cryostats, i.e., 210 and 175 sensors in total, were distributed over the head of the adult and child head, respectively.

The three on-scalp MEG, as well as the reference system sensor layouts, can be seen for the adult and child subjects in Fig. 3.5.
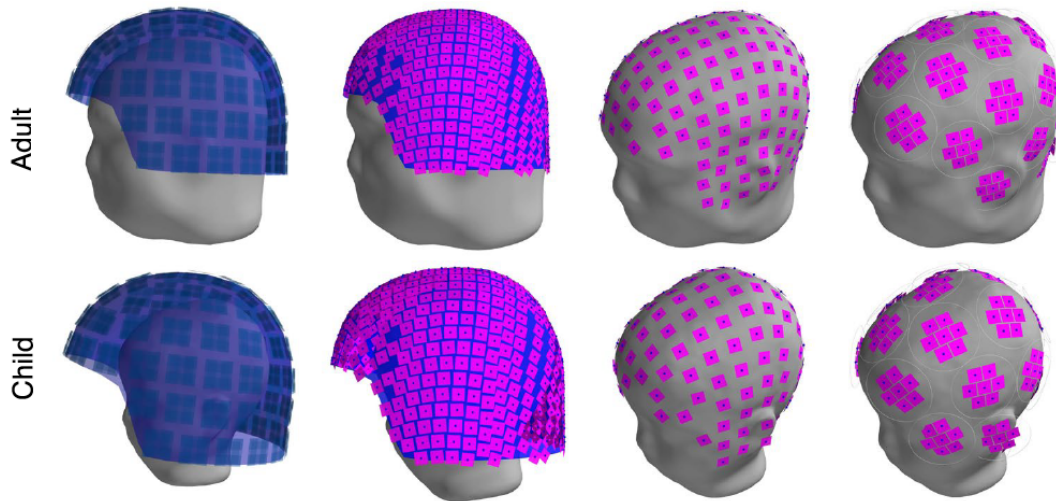

Figure 3.5: Simulated reference and on-scalp full-head MEG systems for adult and child subjects. From left to right: the reference (low-T_c SQUID-based) system, followed by the three on-scalp MEG systems: the helmet-based, fully-flexible, and semi-flexible (7-channel units-based) layouts. The sensors are shown in pink. Helmet-based systems show their respective helmet surface in blue [Paper I].

3.2.2 Total information capacity

Introduced in 1989 by Kemppainen and Ilmoniemi [51], information capacity was among the first methods allowing a direct comparison of different MEG systems and, as such, was used in the development of today's commercial MEG systems [42]. Based on Shannon's theory of communication [52], information capacity characterizes the amount of information a system can extract from a brain. Information

capacity for a given brain depends only on array geometry, i.e. placement, orientation and size of the sensors, and sensor noise.

To be able to sum the contributions of the individual sensors to the total information, their lead fields have to be orthogonal, which is achieved by constructing virtual, orthogonal channels. To this end, the inner product matrix of the lead fields $G_{jk} = \int \mathcal{L}_j \mathcal{L}_k dv'$ is calculated and decomposed as

$$G = U \Lambda U^T \tag{3.5}$$

where $\Lambda = diag(\lambda_k)$ is a diagonal matrix containing the eigenvalues, and U a matrix containing the eigenvectors of G [51]. The channels can then be orthogonalized as $\mathcal{L}'_k = U^T \mathcal{L}_k$. The total information capacity is given as:

$$I_{tot} = \frac{1}{2} \sum_k log_2(P'_k + 1) \tag{3.6}$$

where $P'_k = s^2 \lambda_k / \sum_j (U^T n_j)^2$ is the power signal to noise ratio of the orthogonalized sensor k, s the signal source and n the channel noise [51].

The total information capacity in bits per sample obtained with the different simulated full-head MEG systems with the two subjects can be seen in Table 3.1.

All systems extract significantly more information from the subject than the conventional MEG system used for reference. Interestingly, the on-scalp systems all show higher total information capacity for the child subject as compared to the adult, as opposed to the reference system where the total information capacity is higher for the adult. This is not too surprising as the brain in children is typically closer to the scalp as compared to adults [53]. MEG studies on children are therefore expected to benefit more from the on-scalp approach.

Despite the large difference in the number of sensors, the helmet-based (631 sensors) and semi-flexible (210 sensors for the adult, 175 for the child) show comparable total information capacity values. While the helmet-based system performs slightly better for the adult subject compared to the semi-flexible system, the opposite is the case for the child subject. The highest total information capacity is obtained with the fully-flexible system.

Table 3.1: Total information capacity in bits per sample [Paper I].

	Reference	Helmet-based	Fully-flexible	Semi-flexible
Adult	393	482	547	447
Child	345	535	629	566

3.2.3 Spatial Information Density

Spatial information density (SID), introduced in Paper I, expands total information capacity by a spatial dimension. Whereas total information capacity describes how much information can be sampled from the entire brain at once, SID quantifies the information a given sensor array can extract from an individual source/patch of the

brain. To this end, the total information capacity is calculated for each individual source (i.e., assuming the primary current density J_p is 0 at all but one source locations) as opposed to all sources combined (which is the case for total information capacity where a normal distribution of J_p is assumed). SID can be plotted over the brain surface to show the spatial distribution of information capacity - which can give insights into how well different parts of the brain are sampled by a given MEG system.

The SID was computed for the three on-scalp as well as the reference system with the adult and child subjects. The resulting SIDs mapped onto the subjects' brains can be seen in Fig. 3.6. The SID maps for the two helmet-based systems (the reference and helmet-based on-scalp system) - particularly in the case of the child as subject - show a clear gradient from posterior to anterior, indicating an inhomogeneous spatial distribution of the extracted information over the brain. This can be explained by the position of the subjects' heads. As is usual in MEG studies, the subjects' heads were modeled as rested against the back of the helmet, resulting in a smaller sensor-to-brain distance in the posterior part of the brain - and thus larger signals; at the same time the frontal sensors are far from the brain. Generally, the SID values extracted from the child's brain are higher compared to the adult's - most likely due to the larger scalp-to-brain distance in the latter [53] - and the SID values are higher with all the on-scalp systems compared to the reference. For the adult subject, the helmet-based on-scalp system achieves the highest - if unevenly distributed - SID. For the child subject, on the other hand, the flexible systems perform best. Both show uniform coverage over the brain with comparable SID in the posterior and significantly higher SID in the anterior part of the brain, as compared to the helmet-based on-scalp system.
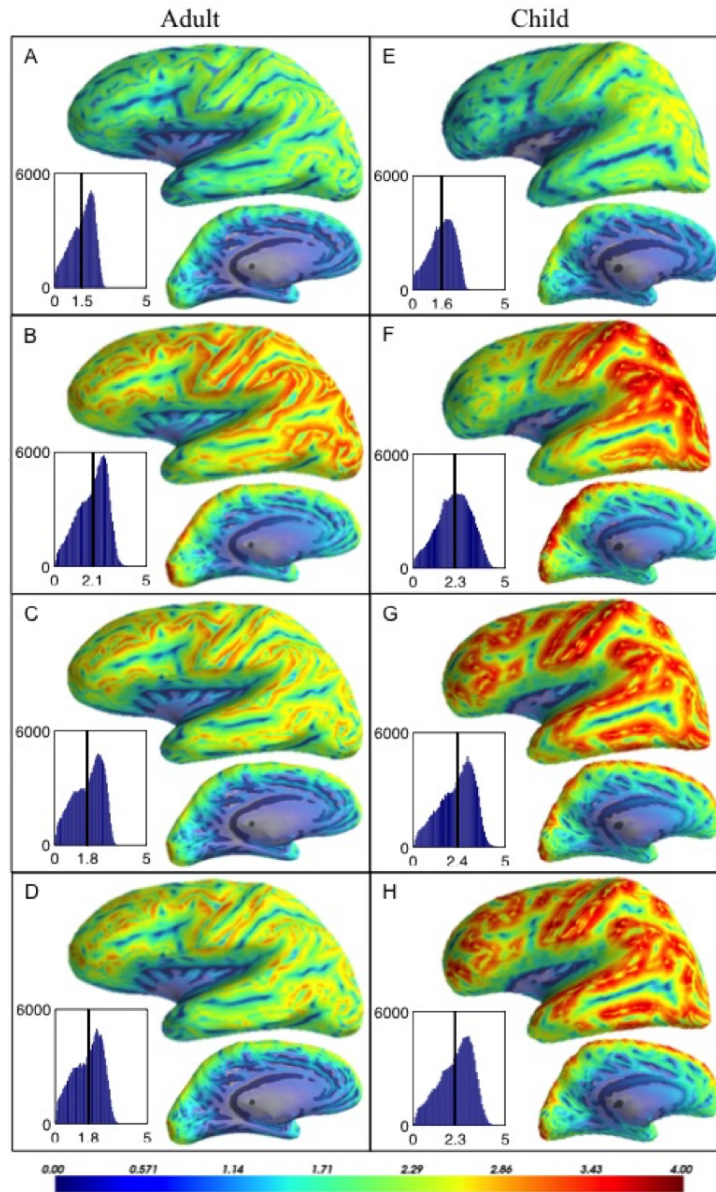
Figure 3.6: SID maps for an adult (left, A-D) and a child (right, E-H) with different sensor arrays. From top to bottom: the reference system (A,E), the helmet-based (B,F), the fully-flexible (C,G) and the semi-flexible (D,H) on-scalp systems. Values are given in bits per sample per mm². [Paper I]

3.3   Sensor localization for on-scalp co-registration

While flexible sensor arrays offer the advantage of improved sampling for subjects with non-standard heads (e.g., children in a system designed for adults), they bring new practical complications. Co-registration of functional (MEG) and structural (MRI) data requires determining the orientation and position of the sensors relative to the subject's head as well as to each other.

In a fixed helmet array, like the ones used in conventional MEG systems, this is simple, as the sensors locations are constant. After an initial calibration of the sensor locations in the helmet, only the head position relative to the sensor array has to be established for each MEG recording - which can be done using HPI coils attached to the subjects head (c.f., §2.2.4 and Fig. 2.4).

Conventional head localization using HPI coils works in the following way. The coils are driven at different frequencies, allowing their amplitudes to be extracted from the sensor signals through spectral analysis (e.g., Fourier transform). For coils modeled as magnetic dipoles, the field that sensor i picks up from HPI coil j can be calculated as:

$$b_{i,j} = \boldsymbol{B}(\boldsymbol{r}_{i,j}) \cdot \boldsymbol{n}_i = \boldsymbol{\mathcal{L}}_m(\boldsymbol{r}_{i,j}, \boldsymbol{n}_i)\boldsymbol{m}_j, \tag{3.7}$$

where $\boldsymbol{r}_{i,j} = \boldsymbol{r}_i - \boldsymbol{r}_j$ describes the position of sensor i relative to the coil/magnetic dipole j, $\boldsymbol{m}$ the magnetic moment of the dipole defined by the magnetic strength $|m|$ and orientation $\hat{\boldsymbol{m}} = \boldsymbol{m}/|m|$, $\boldsymbol{n}$ a vector defining the sensitivity $|n|$ and orientation $\hat{\boldsymbol{n}} = \boldsymbol{n}/|n|$ of the sensor, and $\boldsymbol{\mathcal{L}}_m$ the lead field for magnetic dipoles.

To localize the coils, magnetic dipoles are fitted to the coil amplitudes by minimizing the residual variance between calculated and measured field amplitudes

$$\operatorname*{arg\,min}_{\boldsymbol{r}_j, \boldsymbol{m}_j}\left(\frac{\sum_i (b_{i,j,meas} - \boldsymbol{\mathcal{L}}_m(\boldsymbol{r}_{i,j}, \boldsymbol{n}_i)\boldsymbol{m}_j)^2}{\sum_i (b_{i,j,meas})^2}\right) \tag{3.8}$$

where $b_{i,j,meas}$ is a matrix containing the field amplitudes from the coils j measured by sensors i.

In a flexible sensor array, on the other hand, the relative orientations and positions of the individual sensors change from subject to subject - likely even between recording sessions with the same subject. Co-registration in flexible on-scalp MEG systems therefore needs to include a measurement of the sensor positions and orientations relative to each other for each recording. Such an additional calibration step would add significant time to recording sessions. It would furthermore be practically challenging because of the need to ensure the sensors' positions relative to one another does not change between calibration and the recording on the subject.

In Paper II, we introduced an approach to realizing co-registration in flexible MEG systems by turning around the head localization method used in conventional MEG systems. Instead of using a small set of coils attached to the subject's head, an array of coils on the subject's head can be used to localize the sensors relative to it. If the orientations and positions of the coils relative to each other (on the individual subject's head for a given recording session) are known, a sensor's location and orientation can be determined from the measured coil amplitudes. Fortunately, it is common for the positions of the coils to be established for each individual and session, as this is part of standard MEG head localization routines. However, the

orientations are not typically measured (a practical solution to this issue is presented in §5.3.3 and Fig. 5.15).

To fit the sensors to the data instead of the coils, the minimization in Eq. (3.8) is replaced by

$$\arg\min_{\boldsymbol{r}_i, \boldsymbol{n}_i} \left(\frac{\sum_j (b_{i,j,meas}^T - \boldsymbol{\mathcal{L}}_m(-\boldsymbol{r}_{i,j}, \boldsymbol{m}_j)\boldsymbol{n}_i)^2}{\sum_j (b_{i,j,meas}^T)^2} \right). \tag{3.9}$$

This method has the advantage that it can use existing hardware and routines. Further, if the coil signals are sufficiently separated from neural activity in the frequency domain, the measurement can be run in parallel to the experiment, thereby providing continuous co-registration. This is advantageous because it allows registering and compensating for head movements relative to the sensors, which would otherwise result in measurement errors.
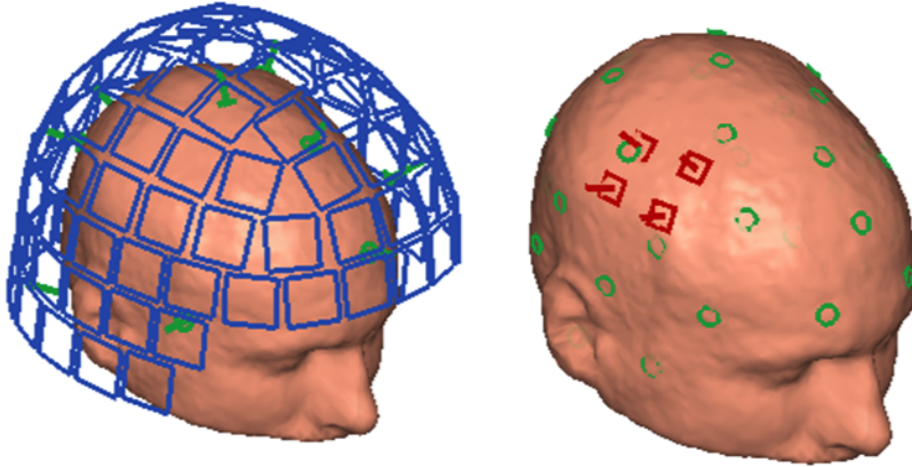

Figure 3.7: Co-registration in conventional and on-scalp MEG. Left: Localizing head position indicator (HPI) coils (green) on the subject's head with a full-head conventional MEG system (blue). Right: Localizing on-scalp MEG sensors (red) with an array of HPI coils (green) on the subject's head [Paper II].

As accurate co-registration is even more important in on-scalp MEG than in conventional MEG (due to the increased proximity between sensors and sources [8, 54]), the sensors should be localized with high accuracy. The feasibility of the method presented here for use in on-scalp MEG was therefore tested in simulations.

To make the simulations as realistic as possible, head models (T1-weighted MRI of a 40-year-old male) and coil configurations (10 evenly distributed HPI coils, driven with 218-288 Hz, 10 nAm^2 magnetic moment) from a set of actual MEG recordings were used. For comparison, the method was tested for a conventional, as well as an on-scalp, MEG sensor array. Sensor locations for the conventional MEG system were based on the sensor array of the commercial TRIUX system (see Fig. 3.8-left). In the on-scalp case, the TRIUX sensor locations were projected to the subjects head (with 1 mm distance; see Fig. 3.8-right). The on-scalp and conventional MEG sensors were assumed to be 8 mm × 8 mm high-T_c SQUID magnetometers with 20 fT/Hz$^{1/2}$ white noise and 26 mm × 26 mm low-T_c SQUID magnetometers

with 3 fT/Hz$^{1/2}$ white noise, respectively. The sensor signals were simulated as a combination of the magnetic fields generated by sinusoidally driven magnetic dipoles approximating the coils, and Gaussian noise approximating the white noise of the sensor. Only white noise was considered here since the coil driving frequencies are typically chosen to be higher than the neuromagnetic signals of interest (in order to avoid interference with them), and thus well above the 1/f-knee of the sensors (typically below 10 Hz, c.f., §4.3 and Fig. 4.7). Finally, the coil amplitudes were extracted from the simulated sensor signals with fast Fourier transform (FFT) and used to individually fit the sensor locations. The sensor fits were performed with non-linear unconstrained optimization in MATLAB using the FieldTrip toolbox [55].
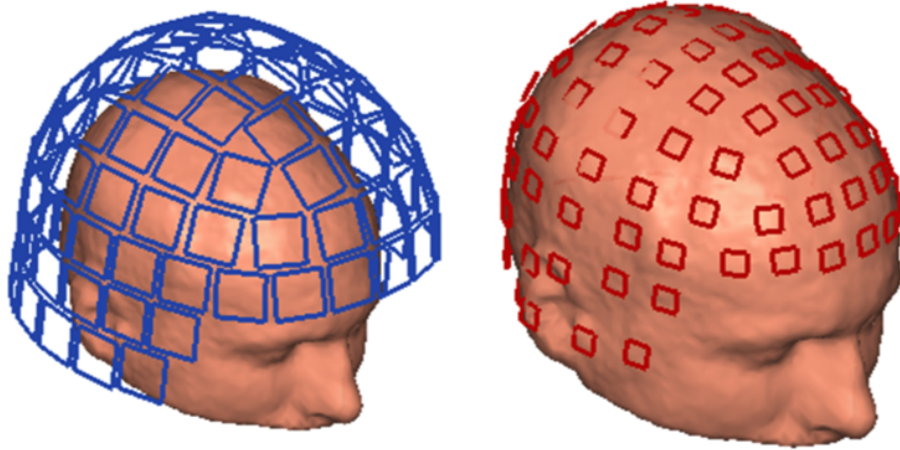

Figure 3.8: Sensor arrays used in simulations. Left: Conventional MEG sensor positions (blue) around the subject's head. Right: On-scalp MEG sensor positions (red) around the subject's head [Paper II].

With <0.1 mm and <0.01 mm average error between the fitted sensor locations and the true locations, both the on-scalp and conventional MEG systems showed errors well below the 4 mm on-scalp co-registration error limit recommended by Zetter et al. [54]. Testing the method with different sensor noise levels and coil magnetic moments revealed a strong dependence of the accuracy on SNR (Fig. 3.9). Since sensor noise is typically fixed, SNR can be primarily affected through the coil magnetic moment (in the form of the coil driving current) and coil placement (the closer to the sensor, the higher the signal). Further simulations also showed improved accuracy with increasing coil recording time. However, for continuous co-registration, the coil recording time should be as short as possible as it determines the frequency/time-resolution at which head movements can be detected.

The results described above were generated based on the assumption that the positions, orientations and magnetic moments of the coils are known precisely. In practice, however, one has to assume errors in the definition of the coil array. The sensor localization was therefore also tested with different levels of coil position, orientation and calibration errors. The localization error was strongly affected by such coil-specific errors, requiring ≤10 % calibration, <2 mm position (typical HPI coil and digitization systems are below these values), and <3 degrees orientation errors to reach <4 mm in head position localization error (see Fig. 3.10).
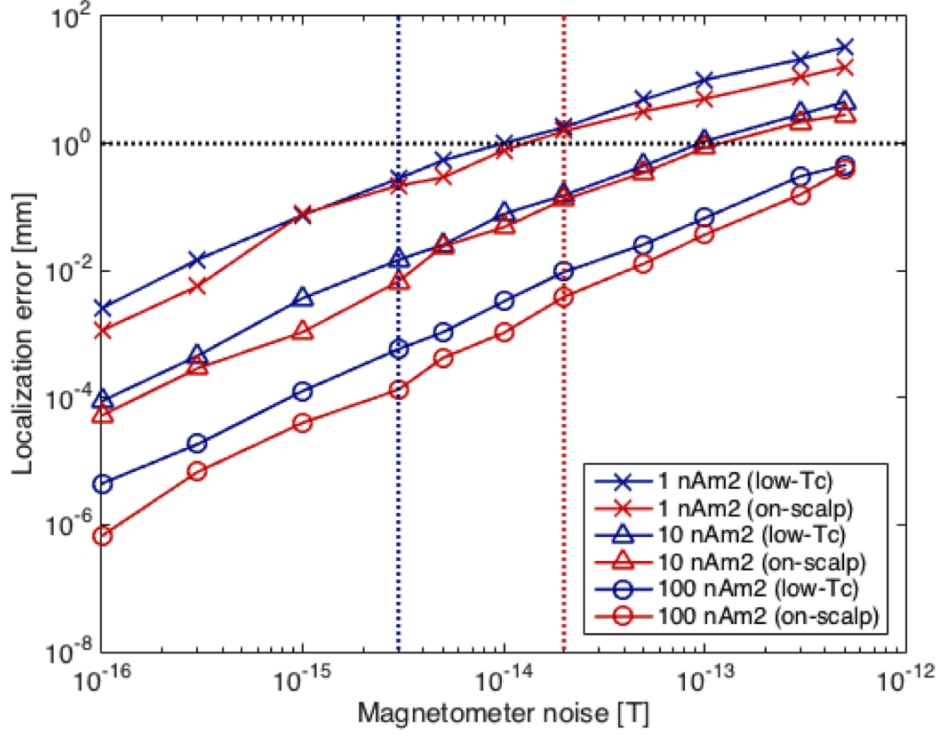
Figure 3.9: Average localization error as a function of sensor noise for different coil magnetic moments with on-scalp (red) and conventional MEG (blue) sensor arrays [Paper II].

Simulations with different numbers of coils also showed that the accuracy of the method increases with the number of coils. If the sensors are only placed within a small region of interest, then arranging the coils closely around that region proved beneficial, since few coils suffice to accurately localize the sensors (four coils were sufficient for <4 mm localization error).

Finally, semi-flexible on-scalp MEG systems that consist of multiple individually movable units containing multiple sensors (like the one described in §3.2) offer additional possibilities for localizing the sensors. Taking advantage of the fact that multiple sensors are fixed relative to each other in a common housing, it is possible to localize these sensors jointly in a single fitting procedure. To this end the sensor positions and orientations are described by a single rigid rotation and translation applied to the known layout of the set of sensors within a unit. The joint optimization thus becomes

$$\arg\min_{\mathbf{T},\mathbf{R}}(\sum_k \frac{\sum_j (b_{i,j,meas}^T - \boldsymbol{\mathcal{L}}_m(-\boldsymbol{r}_{i,j}', \boldsymbol{m}_j)\boldsymbol{n}_i')^2}{\sum_j (b_{i,j,meas}^T)^2}) \tag{3.10}$$

where $\mathbf{T}$ and $\mathbf{R}$ are the 3-dimensional translation and rotation matrices applied to the sensors, $\boldsymbol{n}_i' = \mathbf{R}\boldsymbol{n}_i$ the rigidly rotated sensor sensitivity vector, and $\boldsymbol{r}_{i,j}' = \mathbf{R}\boldsymbol{r}_i + \mathbf{T} - \boldsymbol{r}_j$ the rigidly rotated and translated relative sensor locations. Increasing the number of sensors means the optimization procedure becomes more over-determined. The localization should therefore become more accurate when increasing the number of jointly localized sensors (if the individual sensors' noise is independent). This was
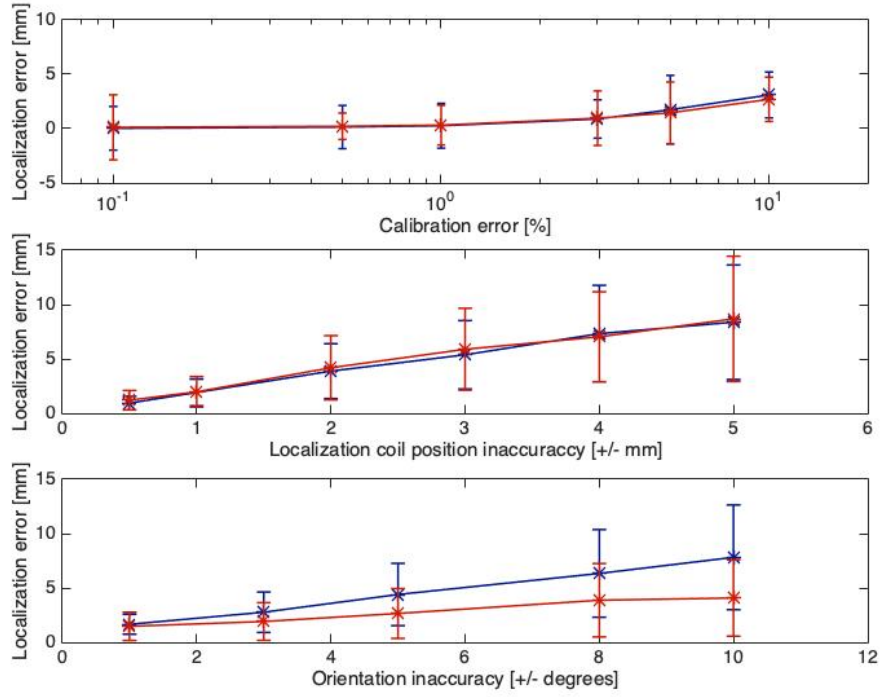
33

Figure 3.10: Average localization error with on-scalp (red) and conventional MEG (blue) sensor arrays as a function of errors in the coil calibrations (top), position (middle), and orientation (bottom) [Paper II].

confirmed in a simulation where jointly localizing up to 10 magnetometers resulted in a significant decrease in localization error. Fitting 10 sensors jointly resulted in a reduction of the localization error by a factor of 27 (on-scalp) and 9 (conventional MEG), respectively [Paper II].

4

On-scalp MEG systems based on high-T_c SQUIDs

In this chapter a 7-channel on-scalp MEG system based on high-T_c SQUID magnetometers is presented along with its single-channel predecessor.

4.1 Introduction

Only a few years after the discovery of high-T_c superconductivity [30] and the subsequent development of high-T_c SQUIDs [56], high-T_c SQUIDs were first used to record neuromagnetic activity [57]. However, these early recordings did not yet take advantage of the reduced need for thermal insulation that resulted from the higher operating temperature. In 2012, Öisjöen et al. performed the first on-scalp MEG recordings using high-T_c SQUIDs [9]. They used two single-channel cryostats containing single-layer YBCO SQUID magnetometers to record induced visual and somatosensory alpha activity at 1 mm distances from the scalp. The same single-channel systems were used in subsequent on-scalp MEG recordings by our group, including the ones presented in Paper V.

4.2 Single-channel systems

The single-channel system employ bicrystal YBCO SQUID magnetometers with 9 mm × 9 mm directly coupled pickup loops. The SQUIDs are read out with single-channel commercial SQUID electronics units SEL-1 from Magnicon (Magnicon GmbH, Berlin, Germany). The SEL-1 includes bias reversal operation for improved 1/f-noise (c.f., §2.3.5). With bias reversal the SQUID field noise stays flat at approximately 50 fT/Hz$^{1/2}$ down to 10 Hz.

The single-channel systems are based on commercial, liquid nitrogen cooled dewars from ILK Dresden (ILK Dresden gGmbH, Dresden, Germany). The cryostat body is made from non-metallic epoxy-reinforced fiberglass. An inner 0.4 L liquid nitrogen (LN$_2$) container is surrounded by super insulation and vacuum to provide the required thermal insulation. The vacuum space is enclosed by an outer shell that can be moved relative to the LN$_2$ container. Activated charcoal is attached to the bottom of the LN$_2$ container to provide additional cryopumping of the vacuum insulation volume. A sapphire rod holding the SQUID magnetometer thermally connects it to the LN$_2$ bath. The SQUID is positioned in close proximity to a thin,

transparent sapphire window at the tail end of the cryostat's vacuum shell. The distance between the window and sensor can be adjusted to <1 mm by moving the vacuum shell relative to the LN_2 container. An LN_2 inlet flange on the top of the cryostat can be used to fill the LN_2 container as well as pump on the LN_2 tank. Pumping on the LN_2 tank reduces the vapor pressure of the LN_2, which in turn lowers its boiling temperature. A schematic of the cryostat can be seen in Fig. 4.1.
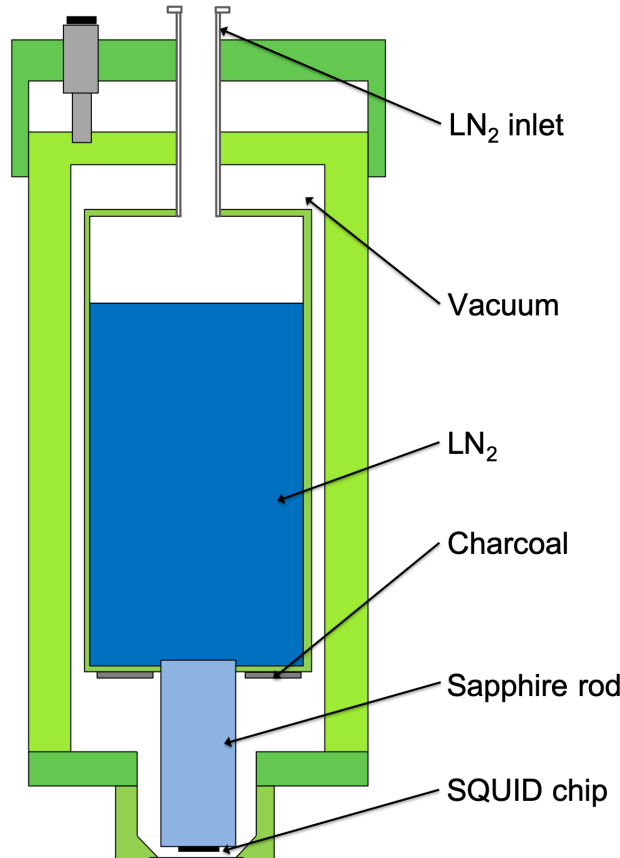

Figure 4.1: Schematic of the cryostat employed in single-channel measurements (ILK Dresden gGmbH, Dresden, Germany).

4.3   7-channel system

While single-channel system recordings have given valuable insights into neural activity in the early years of MEG [58, 59], shown the feasibility of on-scalp MEG [9], and helped quantify the gain of coming closer to the scalp [10], the majority of MEG applications strongly benefit from, or even require, multichannel recordings. Accurately localizing neural activity, for example, requires sampling the neuromagnetic field at multiple locations around the subject's head to map the field pattern. Although evoked activity can be localized with sequential single-channel recordings of the same experimental paradigm [60, 61], this requires significantly longer measurement time and works only under the strict assumption that the brain response is consistent from one recording to another. There is always a risk that the neural

response will change between recordings as a result of changes in the stimulation (e.g., a stimulation electrode moves) or perception thereof (e.g., habituation) - which would violate the assumption. However, it is worth noting that many successful neuroimaging experiments are executed under this assumption. More importantly, only evoked activity can be reliably localized in such a way. To accurately localize spontaneous activity, such as interictal spikes in epilepsy, the main clinical application of MEG to date [3], the magnetic field should be sampled simultaneously at multiple locations around the head. Similarly, analyzing functional connectivity between different brain regions is only possible with multichannel recordings. In addition, single-channel recordings suffer from the small coverage. Since the field is only measured at a single point, measuring unknown neural responses (i.e., without roughly knowing how the resulting magnetic field pattern will look) is impractical, as one could easily miss or misinterpret features of the neuromagnetic field. Finally, multichannel MEG systems are able to use novel noise reduction techniques like signal space separation (SSS) to reduce artifacts. From these issues it becomes apparent that in order for on-scalp MEG to become truly useful for clinical and neuroscience applications, multichannel systems are needed.

It is not feasible to build a full-head on-scalp MEG system from scratch. Similar to the process that took place in the early days of MEG (1980s and 90s), when groups started to go from single-channel systems towards successively bigger systems [42, 43, 62–70], we developed a limited-size multichannel on-scalp MEG system with seven magnetometers as a first step towards full-head coverage. In order to capitalize on the potential advantages of on-scalp MEG, this 7-channel system was designed with the aim of achieving both minimal sensor-to-room temperature distance and dense spatial sampling. The 7-channel system is presented in Paper III.

4.3.1 Cryostat

A schematic of the cryostat can be seen in Fig. 4.2-a. The cryostat contains a 0.9 l LN$_2$ tank in a cylindrical vacuum enclosure. The tank and vacuum enclosure are both made from glass-fiber reinforced epoxy. The tank is connected to the outer shell at the top end via a flexible bellow (which also serves as the LN$_2$ inlet) and at the tail via a small triangular plate (for low thermal contact). Super insulation and vacuum surrounding the nitrogen tank provide thermal insulation. Two strips of activated charcoal are attached to the side of the nitrogen tank to provide additional cryopumping on the vacuum volume when the system is cooled. With an adapter to the nitrogen inlet, it is possible to pump on the nitrogen tank in order to reach lower temperatures.

Seven 11 mm × 11 mm sapphire wedges holding the SQUIDs are glued to a sapphire disc that is fixed into the sidewall of the nitrogen tank close to the tail end. In combination with the sapphire disc, these wedges provide high thermal contact to the nitrogen bath. The sapphire wedges are densely packed (1 mm edge-to-edge) in a hexagonal pattern with one in the center (see Fig. 4.2-b). The outer SQUIDs are tilted towards the center to align them to a surface of a sphere with radius 8 cm, which roughly corresponds to the average curvature of an adult head. A thin (0.4 mm), concave window made from glass fiber reinforced epoxy is set into the

vacuum shell next to the SQUIDs. This window closes the vacuum enclosure which also allows for control of the distance between all of the SQUIDs and the room temperature environment of the head (see Fig. 4.2-c). The window can be adjusted with a screw connection to sit <1 mm from the SQUIDs.

When pumping on the LN_2 with -850 mbar vacuum gauge pressure (corresponding to $\sim$150 mbar on the LN_2 bath), the cryostat reaches 70.1 K ($\sim$ 80 K without pumping) on the sapphire wedges. At 1-2 mm distance from the SQUIDs, the temperature on the outer window settles at $\sim$279 K in air (in a 293 K room temperature environment). However, with the weak thermal connection to the cold head (due to the vacuum insulation) the window temperature quickly (<30 seconds) adjusts to skin temperature when a subject places his or her head on the window - without significantly warming the sensors nor a sensation of cooling on the head thereafter.
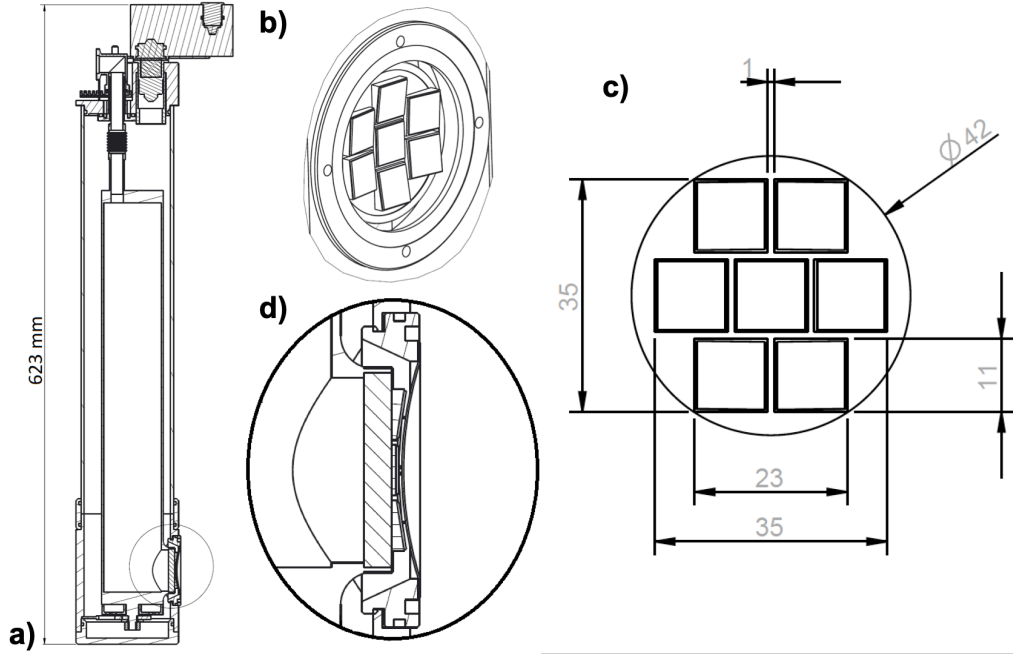

Figure 4.2: Schematic of the 7-channel cryostat. *a)* Cut through the full cryostat. *b)* Detail of the sapphire wedges holding the SQUIDs and *c)* their placement on the sapphire disk (dimensions in mm). *d)* Detail of the curved window next to the SQUIDs on the sapphire wedges. (adapted from [Paper III])

4.3.2 Sensors

The system employs seven high-T_c SQUIDs with directly coupled, 8.6 mm $\times$ 9.2 mm pickup loops made from YBCO on 10 mm $\times$ 10 mm STO bicrystal substrates (see Fig. 4.3). Each SQUID chip contains two hairpin SQUIDs with grain boundary Josephson junctions. The better performing of these two SQUIDs is selected for use on a chip-by-chip basis by bonding it to the output pads on the chip, which are then connected to the SQUID electronics. The junctions are obtained by growing a

140-200 nm thick YBCO film on a bicrystal substrate with a misorientation angle of 22.6° (Shinkosha, Japan). Pickup loop linewidths of 1 and 3 mm were used.
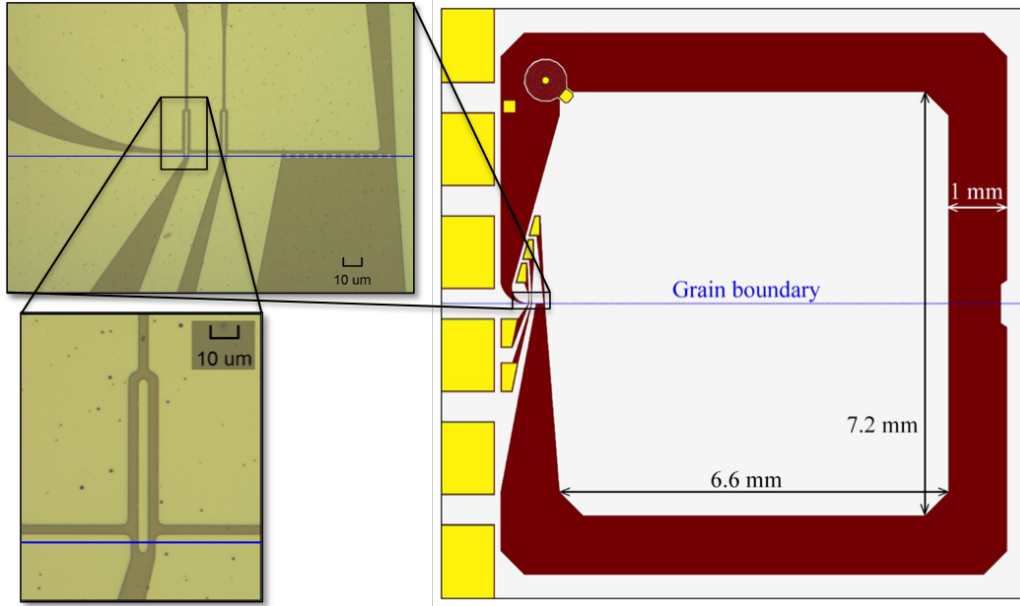

Figure 4.3: Design of the high-T_c SQUID magnetometers used in the 7-channel system. The SQUIDs and pickup loops are made from YBCO (red) on STO (white) with titanium/gold contact pads (yellow). The 9.2 mm × 8.6 mm pickup loop directly couples to the two hairpin SQUID loops, which are located on the substrate grain boundary (blue line). Josephson junctions are formed where the YBCO film crosses the grain boundary. The insets show photomicrographs of the hairpin SQUIDs.

The SQUIDs are controlled by three 3-channel SEL-1 SQUID electronics units from Magnicon (Magnicon GmbH, Berlin, Germany). A breakout box containing shunt resistors and diodes (to protect against current spikes generated by electrostatic discharge or other potentially dangerous sources) connects the SEL-1 units to a vacuum-tight 48-pin LEMO output connector on the top end of the cryostat. Six wires (three twisted pairs) per SQUID lead down to the tail end of the cryostat: two for biasing the SQUID and measuring the voltage, two to provide the feedback, and two reserved for on-chip heaters. In order to reduce their thermal load on the SQUID chips, the wires are wound around –and thus thermally anchored to– the LN$_2$ tank (see Fig. 4.4-a). At the cold head (sapphire disk) the wires are connected to the edges of a printed circuit board (PCB) with cut-outs for the wedges/SQUID supports. On the PCB, copper traces lead to the outer sapphire wedges. The central wedge is connected by wires (in twisted pairs) that are glued to the PCB (see Fig. 4.4-b/d). Silver wires soldered to the PCB lead to gold contact pads on the edges of the sapphire wedges (see Fig. 4.4-b). The silver wires are glued to the contact pads with conductive silver glue. In order to avoid the need to bond to the SQUIDs, the edges of the SQUIDs chip used for contacting are rounded. A bendable mask in combination with sputtering of titanium/gold allows us to make contact pads that lead from the top of the SQUID chip over the edge to the side. The rounded

contacts are connected to the wedge contacts with a droplet of conducting silver glue (see Fig. 4.4-d). Short, flat bonds on the SQUID chips connect the outer pads to one of the two SQUIDs on the chip.
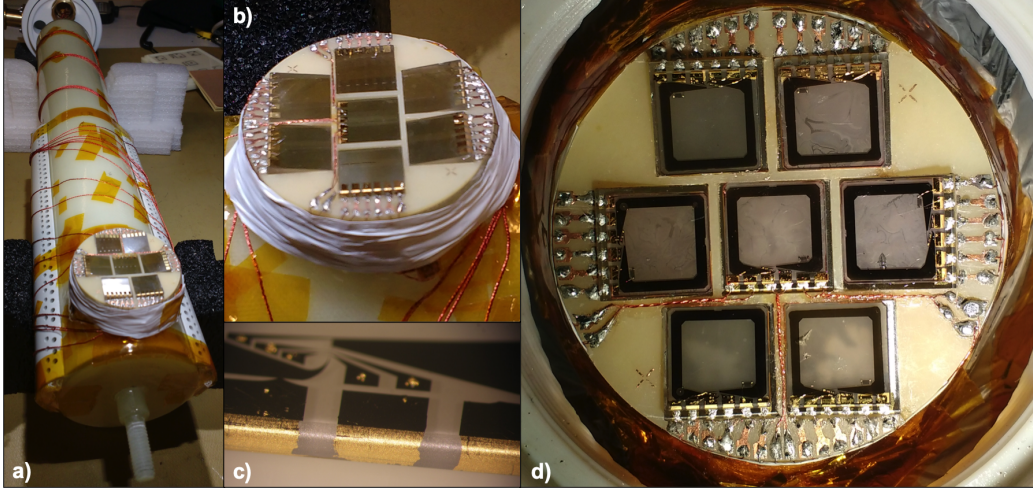

Figure 4.4: Photographs of the cryostat wiring. a) SQUID leads wrapped around the LN$_2$ tank. b) Cold head with gold-contacted wedges and PCB. c) Rounded, gold edges with gold contacts of the SQUID chips. d) Assembled cold head with SQUIDs and PCB.

When packing the sensors densely as we do in this system, crosstalk between the sensors can be an issue and the feedback used to operate each SQUID in a FLL can be especially problematic. Traditionally, small coils on the SQUID chip were used to inductively couple the feedback flux to the pickup loop of the SQUID. The fields produced by such a coil will, however, also couple to nearby sensors, thereby resulting in measurement errors. To reduce feedback crosstalk, we directly inject feedback current into the SQUID loop (see Fig. 4.5-a). Thus, instead of generating a field to cancel changes in external flux, a current is applied directly to the SQUID to cancel changes in circulating current inside the SQUID loop. Alternatively, one can imagine that the current going through part of the SQUID loop generates the feedback flux that compensates changes in external flux. With the sensors used here, < 0.5 % feedback crosstalk can be achieved by using this feedback scheme - compared to 5 % feedback crosstalk with a small, superconducting coil [Paper VII].

We measured the feedback crosstalk in the 7-channel system by applying 1 Φ_0 feedback to one (exciting) SQUID and measuring the generated field with the other (sensing) SQUIDs. Table 4.1 shows the pairwise feedback crosstalk in the 7-channel system. The majority of pairs showed crosstalk below 0.1 %. Channel 4 showed above average crosstalk to Channels 3 and 6. The high values can, however, be explained by the wiring on the PCB: the feedback leads for channel 4 pass between channels 3 and 6. There is no obvious cause for the above average feedback crosstalk from channel 7 to channel 6. Because the inverse case is significantly lower (channel 6 to channel 7: 0.011 %), this is likely also caused by the feedback wires of channel 7 passing close to channel 6.
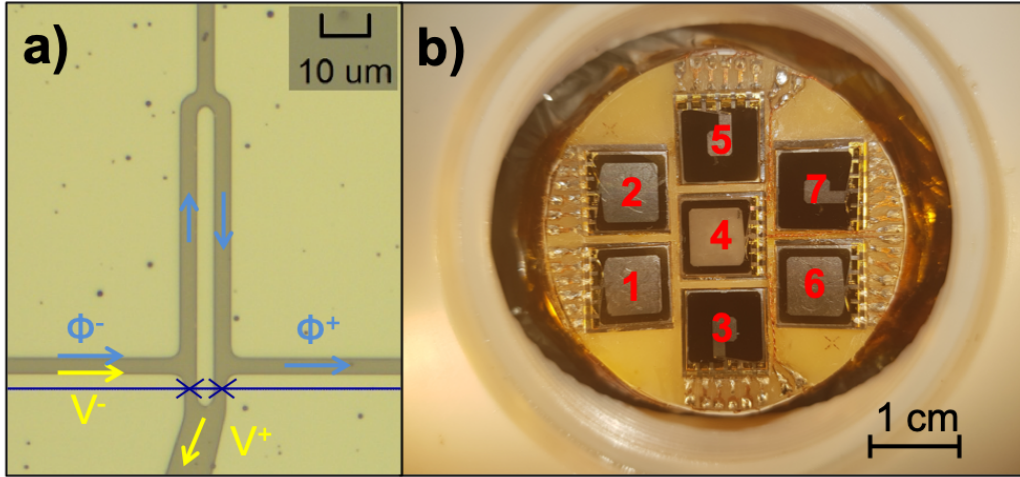
Figure 4.5: a) Microphotograph of a SQUID showing the direct injection feedback concept. Connections and current paths for bias current and voltage readout (V^+/V^-) as well as feedback current (Φ^+/Φ^-) are indicated in yellow and light blue, respectively. The bicrystal junctions are marked by dark blue crosses where the superconducting film crosses the grain boundary (dark blue line). b) Photograph of the assembled cold head (cryostat tail pointing left) showing the SQUID array. Channel numbers are shown in red.

Table 4.1: Feedback crosstalk from exciting (rows) to sensing (columns) channels in parts per thousand [Paper III].

Ex.\Sen.	Ch1	Ch2	Ch3	Ch4	Ch5	Ch6	Ch7
Ch1	-	0.95	0.14	0.17	0.04	0.03	0.01
Ch2	0.35	-	0.03	0.13	0.04	0.02	0.03
Ch3	0.49	0.02	-	0.03	0.01	0.06	0.04
Ch4	0.32	0.05	3.96	-	0.18	5.88	1.09
Ch5	0.07	0.03	0.04	0.14	-	0.04	0.48
Ch6	0.13	0.08	0.54	0.41	0.08	-	0.11
Ch7	0.33	0.04	0.77	1.36	0.67	4.57	-

4.3.3 Calibration

The finished system (Fig. 4.6-a) was calibrated inside the 2-layer magnetically shielded room (MSR) at Chalmers (consisting of two layers of mu-metal and one layer of copper-coated aluminum; Vacuumschmelze GmbH, Hanau, Germany) using a Helmholtz coil placed around the sensor array (see Fig. 4.6-b) to generate well-defined magnetic fields (c.f., [34]). The coil's input voltage-to-field conversion was measured using a fluxgate magnetometer. To minimize measurement errors resulting from low frequency drifts in the remnant magnetic field that is present inside the MSR, an arbitrary waveform generator (Fluke 282, Fluke Co., Everett, WA, USA) was used to drive the coil with a 108 Hz sinusoidal wave. A sinusoid was then fitted to the recorded data to extract the signal amplitudes. From the measured amplitudes the responsivity, R, of the sensors (including electronics gain) can be calculated as

the output voltage, dV, per applied magnetic field, dB: R = dV/dB. To account for the different angle of the sensors, the system was rotated while recording the signals repeatedly in order to find the maximum amplitudes. The maximum amplitude of each sensor is obtained when its sensitive axis is aligned with the applied field. Table 4.2 shows the responsivity of the sensors inside the 7-channel system. The responsivities remained stable within $< 0.5\%$ over multiple cooldowns as well as for different applied fields (0.2 to 10 nT_{pp}). The gain of the SQUID electronics SEL-1 was always set to the maximum of 4000 (in all measurements throughout this work).

Table 4.2: Sensor responsivity measured 10 times (spread over four separate cooldowns) with different applied fields (0.2-10 nT_{pp}) [Paper III].

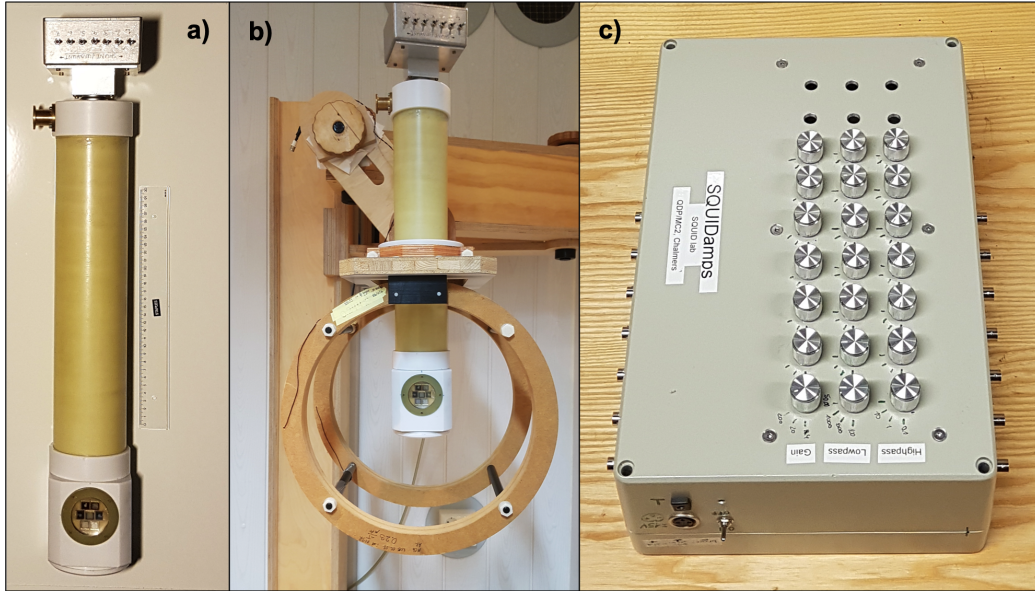| Responsivity	Ch1	Ch2	Ch3	Ch4	Ch5	Ch6	Ch7
Mean [µV/fT]	0.124	0.124	0.154	0.129	0.154	0.119	0.151
Range [±%]	0.26	0.21	0.40	0.19	0.43	0.22	0.25

Figure 4.6: Photographs of the system. a) Finished cryostat with SQUIDs. b) 7-channel system with Helmholtz coil (used for calibration and field cancellation). c) 7-channel SQUID amplifier/filters (with space for up to 10 channels); schematic and bill of materials of the amplifier/filter circuit boards can be found via the following link: https://github.com/cpfeifferGH/SQUIDamps

4.3.4 Amplifiers/Filters

When recording MEG signals, it can be necessary to amplify more than the gain of the electronics preamplifier, e.g., in order to overcome a high input noise at the digitizer. In case of the 7-channel system, the analog output signals from the SEL-1 electronics are analog-to-digital converted and read in using a 16-bit data acquisition (DAQ) system, typically a DAQ NI-USB6259 or NI-USB6258 (National Instruments,

Austin, TX, USA). Recording, e.g., neuromagnetic signals on the order of 100 fT with a sensor responsivity of 0.13 µV/fT would require <13 µV sensitivity - which is not feasible with the NI-USB6259 [71]. Additional dedicated low-noise amplifiers were therefore developed for the system. Because low frequency drifts of the magnetic field (∼0.01-0.1 Hz with magnitudes of 1-2 nT inside a typical MSR with two layers of mu-metal [45]) would limit the possible maximum gain, the amplifiers were combined with hardware high-pass filters. Finally, hardware low-pass filters are used to avoid aliasing when digitally sampling the sensor signals. Amplifiers, together with the high- and low-pass filters for seven channels are combined in a common unit seen in Fig. 4.6-c. Each channel consists of a 5 stage circuit that looks as follows:

- Input buffer (unity gain amplifier)
- 1st order high-pass filter (f_c = 0.1, 1, or 10 Hz)
- 1st amplification (gain = 2)
- 1st order low-pass filter (f_c = 100, 500, 1000, or 5000 Hz)
- 2nd amplification (gain = 2, 10, or 100).

Different options for the cutoff frequencies f_c of the high- and low-pass filters, as well as the gain of the final amplification stage, can be chosen for each channel manually using control knobs (see Fig. 4.6-c).

The input noise of the amplifier/filter circuits was measured as ∼15-35 nV/Hz$^{1/2}$ depending on the filter cut-off (the noise is dominated by the thermal noise of a resistor used in the high-pass filter), which is well below the output noise of the SEL-1 (4000×0.4 nV/Hz$^{1/2}$ = 1.6 µV/Hz$^{1/2}$ [72]). The amplifiers/filters (hereafter called "SQUIDamps") are powered by a ±15 V, ≥200 mA supply.

4.3.5 Noise

Since neuromagnetic signals are expected to span ∼0.5 to at least 1000 Hz [2] an optimal MEG system should be sensitive over that whole frequency band. SQUIDs typically perform best at frequencies >100 Hz, showing 1/f-like noise at lower frequencies. However, steps can be taken to avoid excess 1/f-noise.

Standard 2-layer MSRs, which are used in many MEG facilities, provide high shielding factors at high frequencies (>100 Hz). However, at low frequencies they shield only moderately - in some cases showing remnant fields of several tens of nT (with drifts on the order of pT) [45]. To minimize the risk of the SQUIDs trapping flux during cooldown in the presence of such relatively high magnetic fields (which can considerably increase their 1/f-noise [73–75]), the 7-channel system should be cooled while the field is reduced as close to zero as possible. To this end, a Helmholtz coil is placed around the sensor array with coil loops parallel to the sensor array (see Fig. 4.6-b). A current is then applied to the coil to cancel the remnant DC field component that is normal to the SQUID array. More details on this procedure can be found in Appendix A.

Operating the SQUIDs with bias reversal is furthermore favorable to DC bias due to the resulting suppression of 1/f-noise. However, we observed strong crosstalk of the bias current to neighboring channels. The crosstalk was in fact so high that it proved impossible to lock all seven SQUIDs at the same time with bias

reversal, however, the problem could be solved by synchronizing the bias clocks. This is because the bias current is modulated by a square wave, i.e., the current jumps between two discrete levels in bias reversal mode. Bias crosstalk consequently manifests itself in neighboring SQUIDs as an external flux that jumps between two discrete levels. If the neighboring SQUID uses the same clock (i.e., the biases are switched simultaneously), then the flux jumps are synchronized with the bias reversal, resulting in a constant offset in flux between positive and negative bias. Fortunately, such an offset can be compensated by the electronics with a bias flux [72]. Within a single SEL-1 unit, synchronizing bias clocks is straightforward - the electronics includes an option for the three channels to share a clock. However, synchronizing clocks between different SEL-1 electronics required additional changes to both hard- and software. By bypassing the shunt resistors of the electronics' clock inputs and adding a global slave mode to the software (SQUID viewer, Magnicon GmbH, Berlin, Germany) we were able to share a single bias clock between all three SEL-1 units.

The noise spectra of the seven SQUIDs when cooled down in a low magnetic field environment (roughly ± 1 nT, limited by the low-frequency resolution of the flux gate we use to compensate the remnant field inside the MSR) and operated in an FLL with synchronized bias reversal can be seen in Fig. 4.7. The SQUIDs reach noise levels between 50 and 130 fT/Hz$^{1/2}$ down to $\sim$8 Hz. Several peaks can be seen at 50 Hz and harmonics. These are the result of power line noise.

4.4 Support

In order to be able to record on-scalp MEG, the sensors have to be placed on the subject's head. With the comparatively small coverage of the 7-channel system (even more so for the single channel system), being able to flexibly place (and orient) the sensor array on the subject's head is of great importance. At the same time, the system should not rest on or be fixed to the subject's head for safety and subject comfort as well as to avoid movements of the system in the remnant fields within the MSR. To allow both flexible positioning and rigidity, the system needs to be mounted to an adjustable support structure. To avoid magnetic disturbances, the support should furthermore not contain magnetic materials.

We use a wooden stand with flexible arm (seen in Fig. 4.8) to flexibly support and position the 7-channel system. The base of the wooden stand consists of a rectangular wooden pole attached to a large wooden plate that serves to stabilize the entire construction. We have two wooden arms that can be mounted to the stand at variable height. Each arm contains 3 horizontal and two vertical (one with sliding connection) hinge joints to allow maximum freedom of movement. Each joint contains a screw that allows locking/releasing it. Cryostats are mounted to the end of the arm using a circular wooden clamp (see Fig. 4.8-b). Clamping (as opposed to fixed screw connections) the cryostat enables additional flexibility in rotation and height. The clamp was constructed to fit the previously described single-channel cryostat 4.2. A plastic ring (cut in half) is used to adapt the clamp to the diameter of the 7-channel cryostat because it has a lower outer diameter, as compared to the single-channel cryostats for which the support was originally designed.
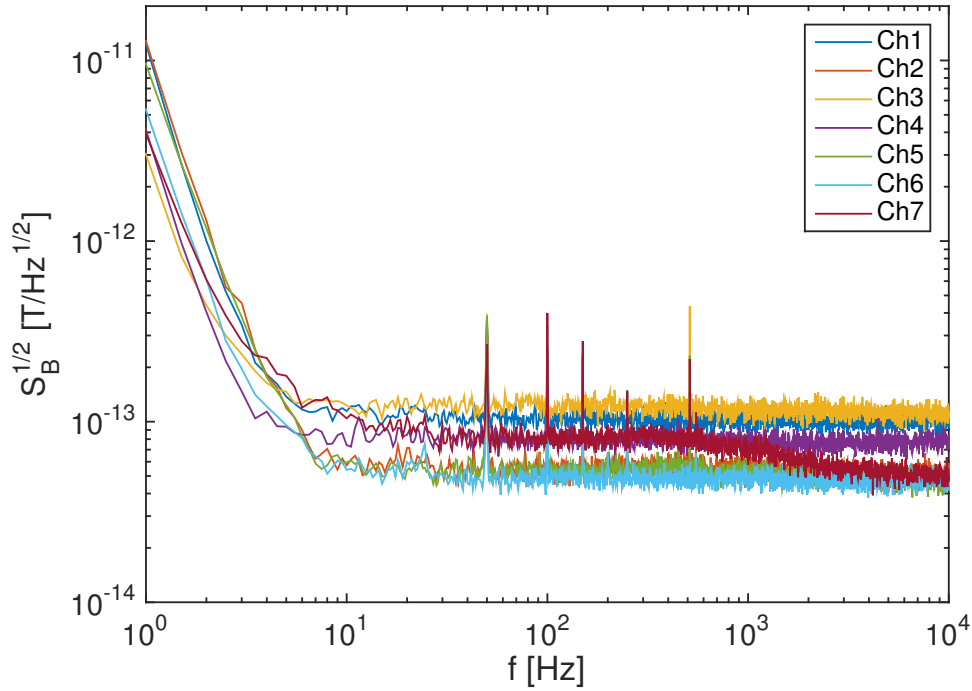
Figure 4.7: Noise spectra of the SQUID magnetometers inside the 7-channel system, as measured in the 2-layer MSR we have at Chalmers [Paper III]. White noise levels and the transition from 1/f- to white noise ('1/f-knee') vary in the range of 40-130 fT/Hz$^{1/2}$ and 3-10 Hz, respectively, from SQUID to SQUID and cool-down to cool-down.
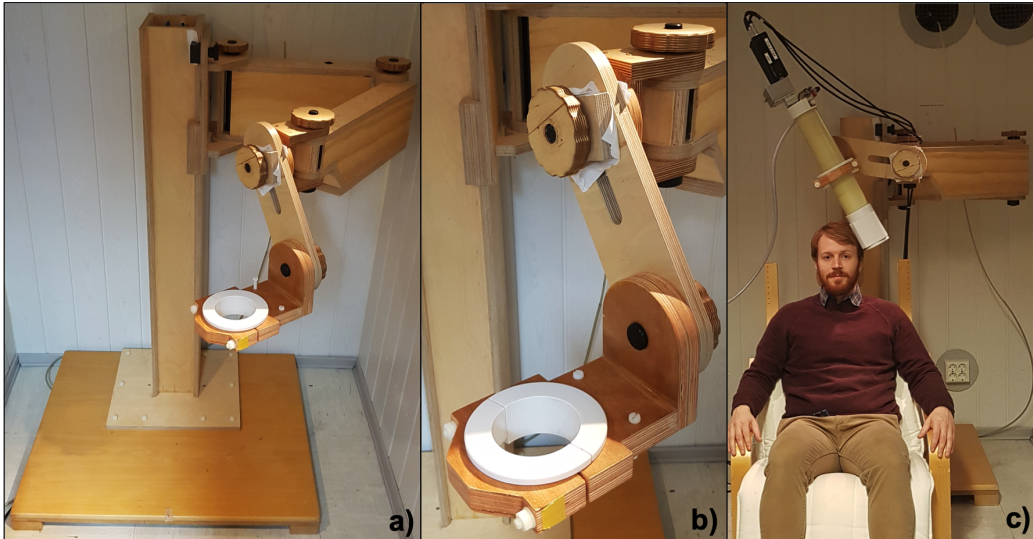

Figure 4.8: Photographs of the cryostat holder. a) Wooden support structure with one arm assembled. b) Close-up of a wooden arm and cryostat mount with plastic adapter (white) for the 7-channel cryostat. c) Example setup for MEG recordings with the 7-channel cryostat positioned on the head of a seated subject (the author).

45

5

On-scalp MEG recordings

In this chapter, results from MEG recordings with the two on-scalp MEG systems described in the previous chapter are presented. The recordings can be separated into two main groups according to their purpose: proof-of-principle and benchmarking.

5.1 Introduction

The first MEG recordings were performed using simple paradigms whose neural responses were more or less known from EEG and/or brain anatomy, thereby allowing accurate predictions of their magnetic manifestation. Thus, early recordings primarily served as proofs-of-principle, showing the feasibility of MEG and laying the foundation for subsequent experiments. With the emergence of multichannel MEG systems, focus shifted towards source analysis, where MEG was able to reveal and localize previously unknown sources. These recordings, however, were still performed using mainly basic sensory stimulation and were often only accepted after being verified with the more established EEG [1]. As systems and analysis improved, experiments became increasingly more complex. Full-head systems allowed accurate localization of spontaneous activity (e.g., epileptic interictal spikes [76]), as well as connectivity between different brain regions. As a result, research focus shifted towards higher level cognitive functions, such as learning, language and - in recent years - social interaction.

On-scalp MEG has to follow a similar path to the one that conventional MEG has taken in the past. Start with basic, proof-of-principle recordings to demonstrate its feasibility; validate it with an established neuroimaging modality (in this case, e.g., conventional MEG); and, finally, try to show its unique capabilities compared to other modalities.

The recordings that were performed as part of this work have taken us a long way along that path. Here, I present these experiments in two groups: proof-of-principle recordings that were aimed at demonstrating the feasibility of high-T_c SQUID-based on-scalp MEG and benchmarking recordings where recordings with conventional and high-T_c SQUID-based on-scalp MEG were compared both to validate on-scalp findings with conventional MEG, but also to demonstrate its advantages and unique capabilities.

5.2 Proof-of-principle recordings

To demonstrate the feasibility of on-scalp MEG using high-T_c SQUIDs, we recorded well established paradigms with the 7-channel on-scalp MEG system. The recordings were presented in Paper III, but will be described here in more detail. The recordings were performed inside a 2-layer MSR consisting of two layers of mu-metal and one layer of copper-coated aluminum (Vacuumschmelze GmbH, Hanau, Germany).

The recordings were done in compliance with national legislation and the code of ethical principles (Declaration of Helsinki) and were approved by the regional ethical authority in Gothenburg, Sweden (Regionala etikprövningsnämnden i Göteborg, dnr 1143-16). All subjects gave informed consent.

5.2.1 Alpha activity

Using the recently developed EEG, Hans Berger first reported neural oscillatory activity at ∼10 Hz in humans, naming them alpha waves [77, 78] (sometimes called Berger waves in his honor). Alpha activity, a result of neuronal synchronization occurring in the frequency band 8-12 Hz [12] (sometimes defined as 7-14 Hz [79, 80]), was also recorded by David Cohen in the first MEG recording in 1968 [4]. Both Berger and Cohen recorded alpha activity that occurs spontaneously in the occipital part of the head when subjects are relaxed, yet alert, with their eyes closed. Due to its high amplitude and spontaneous, widespread occurrence, such alpha activity was well suited for these early recordings. It is furthermore easily modulated by the subjects simply opening their eyes, which reduces the magnitude of the alpha activity significantly.
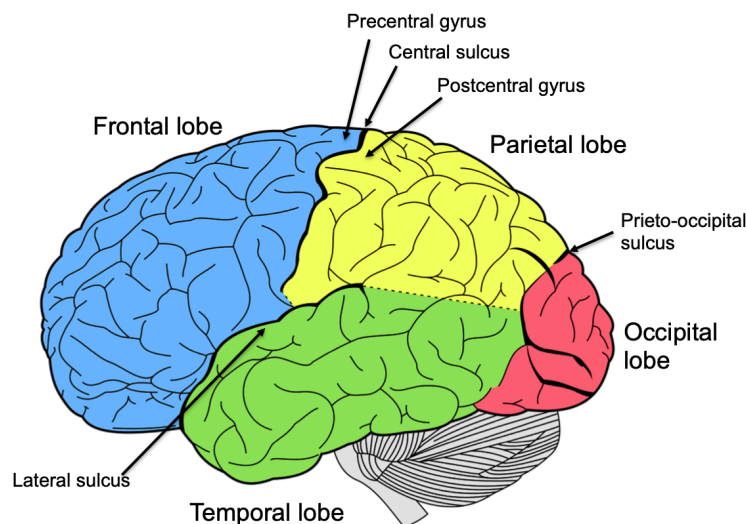

Figure 5.1: Drawing of a human cerebral cortex showing important regions. Adapted from [81]. This work focuses on studies of visual alpha modulation from the occipital lobe, auditory evoked activity generated near the lateral sulcus, and somatosensory evoked activity generated near the postcentral gyrus and central sulcus.

MEG recordings of occipital alpha activity have shown its sources to be located primarily in the parieto-occipital sulcus (see Fig. 5.1), near the longitudinal fissures that separates the brain hemispheres, and the calcarine fissure in the visual cortex [3, 82]. Alpha activity in humans has also been observed in the somatosensory, auditory, and prefrontal cortices [83]. Due to its occurrence in relaxed, resting subjects, alpha activity was originally believed to indicate a resting state. Today, alpha rhythms are thought to represent an active inhibition of sensory processing [12, 80]. Occipital/visual alpha, for example, has also been shown to decrease when attention shifts from auditory to visual [80, 84] or is focused inward [85]. Generally, alpha that is related to one type of sensory input decreases when attention is focused on that input [80]. Conversely, alpha increases with memory demand, indicating a suppression of potentially distracting information [12, 86].
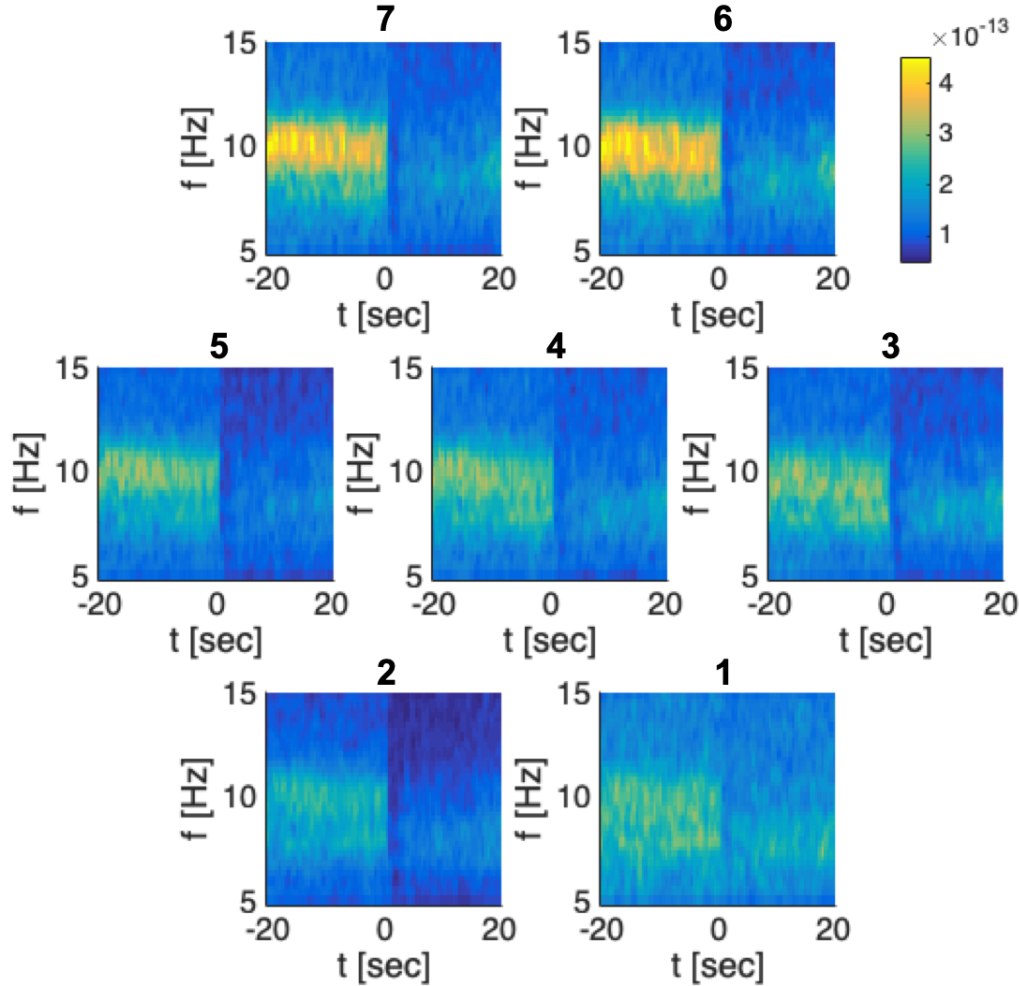

Figure 5.2: Averaged time frequency spectra of induced alpha activity recorded with the 7-channel system. The subject opened his eyes at t=0.

A healthy subject (male, 39 years old) was recorded while seated with the 7-channel cryostat window aimed at the occipital part of the head, close to the occipital protuberance (between O1 and O2 in the 10-20 electrode EEG system [87]).

Every 30 seconds the subject was verbally instructed to open or close his eyes (alternating). When opening his eyes, the subject looked at a large picture of a wooded nature scene. Multiple recordings of 10 to 30 trials were performed. The sensor signals were amplified (gain = 200) and band-pass filtered (1 - 1000 Hz) with the SQUIDamps before being digitized (5000 Hz sampling rate) and read in using a LabVIEW-controlled NI-USB6259 (National Instruments, Austin, Texas, USA) DAQ. A timed digital trigger signal was generated using a second DAQ NI-USB6258. Data analysis was performed in MATLAB (MATLAB R2015a, Mathworks, Natick, MA, USA) using the FieldTrip toolbox [55]. The data was band-pass filtered between 5 and 15 Hz. Time-frequency spectra were estimated with a multitaper frequency transform (using DPSS tapers) and averaged over the trails.

Average time-frequency spectra of 30 trials can be seen in Fig. 5.2. A clear suppression of activity in the alpha band can be observed after the subject opened his eyes. The suppression of alpha activity was in fact strong enough to be observed on the single trial level in the form of a drop in amplitude (see Fig. 5.3).
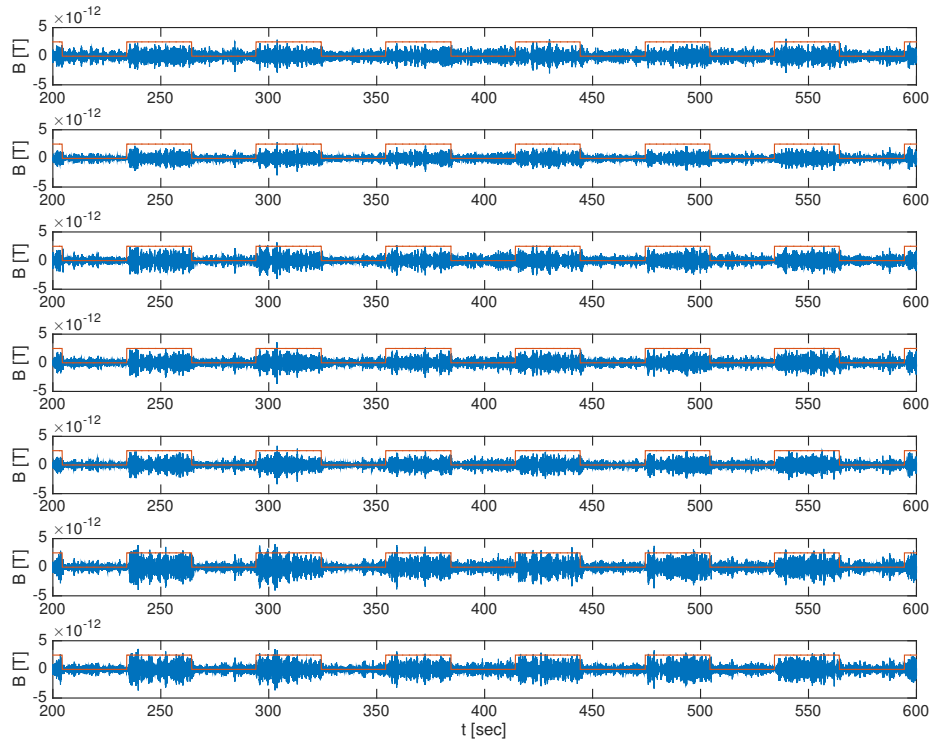

Figure 5.3: Band-pass (8-12 Hz) filtered alpha recording (blue) showing modulation of alpha activity. The trigger signal is shown in red. High signal level of the trigger indicates eyes closed and low signal level eyes open.

In the time-frequency spectra, alpha power seems to be concentrated at two distinct frequencies, ~8 and ~10 Hz, that appear to be modulated to a different extend by the eyes closed/eyes open paradigm. The frequency spectra of the data before

and after the subject opens his eyes support this observation (Fig. 5.4 and in more detail in Fig. 5.5) where two distinct peaks can be observed in the alpha range. While the upper alpha seems to be completely suppressed when the subject opens his eyes, the lower alpha is only partially decreased. Two independent frequency components have been observed before. In EEG recordings, Klimesch et al. found distinct lower (∼7-9.5 Hz) and upper (∼9.5-12 Hz) alpha components that they believed to be related to attention and semantic memory processes, respectively [88]. While the connection between lower alpha and attention is not clearly established, it could explain why the lower alpha frequency was less affected by eyes open versus eyes closed as well as the short, sharp suppression of the lower alpha power at ∼1 sec when the subject is instructed to open his eyes and his attention is this likely to be modulated (c.f., Fig. 5.2).
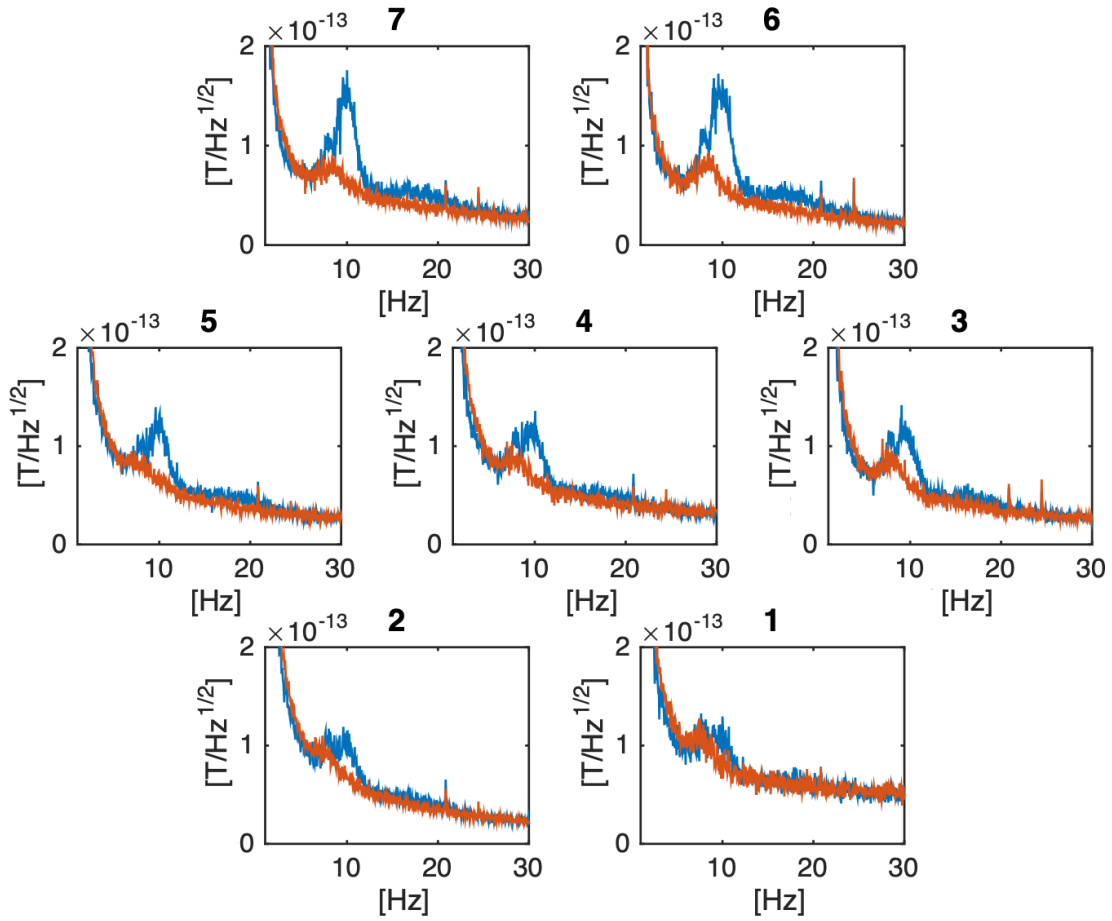

Figure 5.4: Frequency spectra of the data recorded with the 7-channel system before (blue) and after (red) subject opened his eyes. The spectra were obtained with fast Fourier transform (FFT), averaged over 30 trials.

In addition to the alpha activity, an increase in activity over a wider frequency band (up to 25 Hz) can be observed during the eyes closed period in Fig. 5.4 and 5.5. Furthermore, several channels exhibit what appears to be another peak in the beta band (12-30 Hz) at ∼17 Hz (most prominently seen in channel 6).

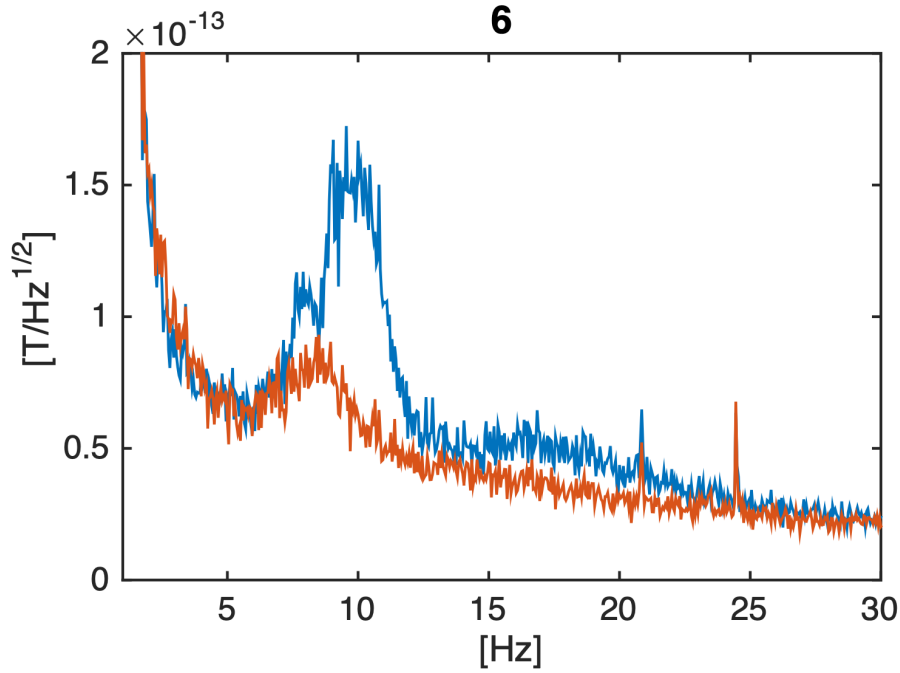Fig. 5.6 shows topographies of the recorded power spectral densities for the two

Figure 5.5: Frequency spectrum of the data recorded by channel 6 of the 7-channel system before (blue) and after (red) subject opened his eyes. The spectra were obtained with fast Fourier transform (FFT), averaged over 30 trials. Channel 6 was chosen here

alpha bands before (left) and after the subject opened his eyes (right). The upper alpha band shows higher power in the superior located sensors (channels 6 and 7) compared to the inferior ones (see Fig. 5.6), indicating it may have been advantageous to place the cryostat at a higher position on the subject's head in order to ensure we sampled the highest power alpha signals. However, the same trend is not observed in the lower alpha band wherein higher power is sampled in the lower sensors. This may point to different locations of the neural sources underlying the two alpha bands.

The observed splitting of the alpha band into two independent components merits further investigation with additional recordings. With higher placement of the cryostat on the subject's head, the observed alpha amplitude, which was already sufficient to see alpha modulation on the single trial level, might increase further. Similarly, additional recordings with a lower cryostat position may be better suited for studying the lower-alpha band we observed.
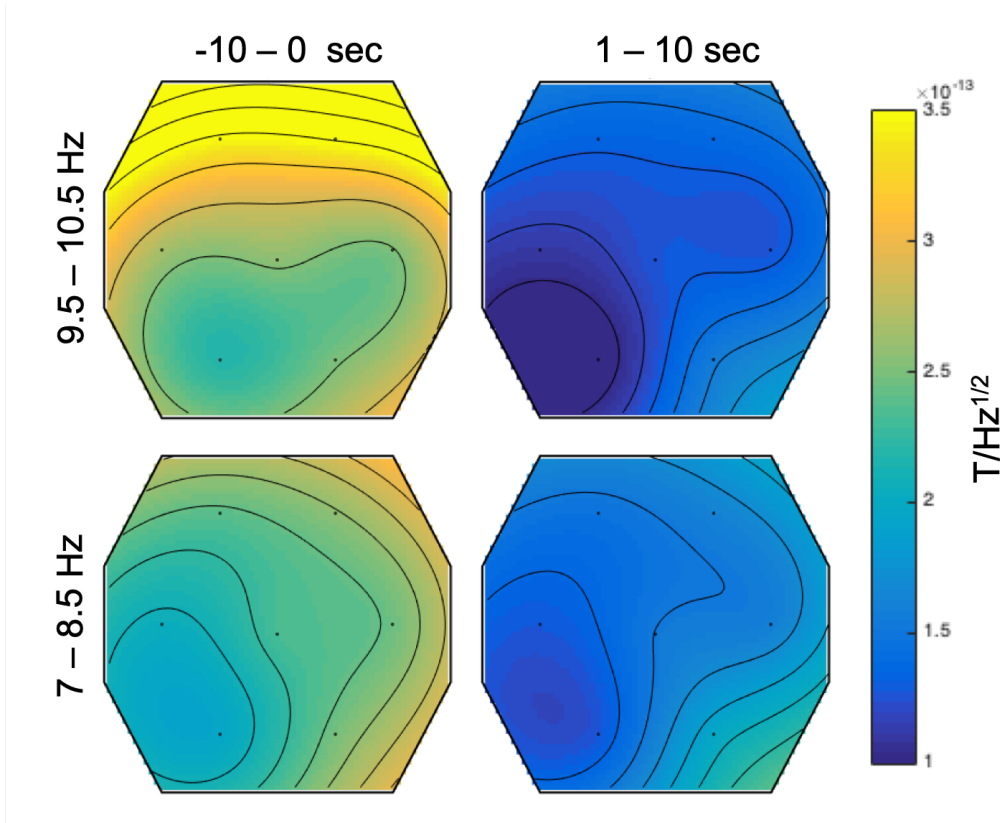
Figure 5.6: Topographies of the alpha amplitude spectral densities recorded with the 7-channel system. Topographies are shown for the upper (top) and lower (bottom) alpha bands with the subject's eyes closed (left) and open (right).

5.2.2 Auditory evoked fields

Auditory evoked activity was among the first to be studied with MEG [1, 89]. Due to the strong, robust response, relatively simple stimulation paradigm, and vast prior knowledge from EEG and MEG recordings [1, 12], auditory evoked responses are well suited for proof-of-principle recordings with on-scalp MEG. They are furthermore clinically relevant, as they are used for pre-surgical mapping of the auditory cortex and diagnosing effects of brain injury on temporal lobe function [3].

In the auditory pathway, sound travels into the ear, where their spectral content is decomposed in the cochlear. From there, the frequency-mapped (tonotopic) information travels through the brainstem and to the auditory cortex on both hemispheres [12]. From the auditory cortex, the information passes on to higher function multimodal areas. While it is possible, yet challenging, to record auditory activity from the brainstem [90], the majority of MEG recordings of auditory activity focuses on the auditory cortex, which is much easier to record [3]. The auditory cortex is located on the superior temporal plane roughly in the lateral sulcus just posterior to the central sulcus (c.f., Fig. 5.1).

Auditory evoked responses are characterized by three prominent peaks that occur with a post-stimulus onset timing of approximately 50 ms (P50m), 100 ms (N100m) and 150-250 ms (P200m) [12, 91] - of which the N100m is typically the strongest.

The main components of an evoked response are traditionally named according to their manifestation in EEG: the labels consist of a letter indicating the voltage potential polarity (N and P for negative and positive, respectively) followed by their latency in milliseconds, and an 'm' to specify that we record the magnetic component. The polarity is defined for one peak of the electric or, in the case of MEG, magnetic field. In this work the component names are used for both peaks interchangeably (i.e., P50m refers to both P50m and N50m). The P50m is believed to be generated in Heschl's gyrus in the primary auditory cortex (AI) [12], while the N100m originates in the planum temporale just posterior to AI [3]. The N100m can be observed in both hemispheres, although approximately 22% higher and 9 ms earlier in the contralateral, as compared to the ipsilateral hemisphere [92]. The P200m is believed to be generated anterior to the N100m [12]. For tones of duration longer than 50 ms, the P200m is followed by a long lasting negative deflection (called sustained field, SF) whose duration depends on the stimulus duration [12]. Both P50m and N100m are subject to adaptation, meaning that the amplitude is reduced if the same sound is presented frequently. Adaptation is stronger the more frequent the sound is presented, i.e., the shorter the inter-stimulus interval (ISI). To record P50m and N100m, the ISI should thus be at least 500 ms (up to 8 s) [12]. Adaptation can be reduced by presenting different tones - the more different, i.e., the further apart in frequency, the less adaptation [93]. Tonotopy is maintained in the auditory cortex [94]. This means that different tones activate different sources and therefore different AEFs.

AEFs were recorded in a healthy subject (female, 30 years old) while seated with the cryostat positioned at the left temporal region slightly above the left preauricular point (approximately T3 in the 10-20 electrode EEG system [87]). A LabVIEW program was used to generate digital trigger signals (using an NI-USB6258 DAQ), as well as the auditory stimulation through a desktop loudspeaker. Sound from the speaker was transferred into the MSR and to the right ear of the subject via plastic tubes with an ear inset at the end. The latency of the sound presentation was estimated as 30 ms, which was corrected for in the data analysis. The experimental paradigm consisted of 1 kHz tones (400 ms duration) presented at an ISI of 1 second (with ±10 ms jitter). One in five stimulations was replaced by a 1.2 kHz tone oddball (with a different trigger marker in order to distinguish them in the data processing) to reduce adaptation.

After amplification and filtering with the SQUIDamps (gain = 200, band-pass 1 to 1000 Hz), the SQUID signals, along with the digital trigger signals, were sampled with an NI-USB6259 DAQ at 5000 Hz. The data was read in with a LabVIEW program that also computed online time-locked averages of the sensor signals using the digital triggers (see Fig. 5.7). Online averages offer the advantage that the operator gets an idea of the signals that are picked up at the time of recording. If the sensors do not pick up the desired signal (e.g., because the cryostat position is not optimal or a SQUID is functioning improperly), the operator can see it early on during the recording and has the chance to stop the measurement and fix the detected problem. The online averages were computed by localizing trigger signals in the latest data block that was read in, extracting a data set around the trigger

according to a user-defined pre- and post-stimulus period, subtracting the mean of the signal during the pre-stimulus period (baseline), and averaging the trials as they are sampled.
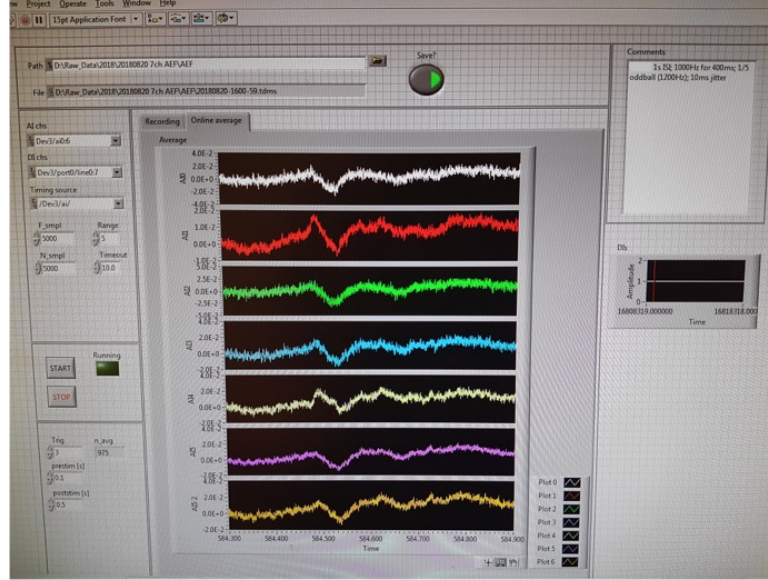

Figure 5.7: Data acquisition software with online averaging used in AEF recordings. All channels show clear negative deflection ∼100 ms after the stimulus onset (i.e., the N100m of interest).

Offline data analysis was performed in FieldTrip [55]. The data was band-pass filtered from 3 to 60 Hz and epoched between 100 ms before and 400 ms after stimulus onset. DC offsets were removed based on a baseline period from 100 to 0 ms before the trigger.

The averaged epochs can be seen in Fig. 5.8 (blue lines). To get a better idea of the noise in the recording, time-locked averages of the differences between odd and even epochs were also computed (Fig. 5.8, red lines).

All channels show peaks at approximately 50, 100 and 150 ms with alternating polarity. The polarity and latency of these peaks matches those expected for the P50m, N100m, and N200m components. The peak amplitudes can be found in table 5.1.

Table 5.1: AEF peak amplitudes in femtotesla measured with the 7-channel system.

	Ch1	Ch2	Ch3	Ch4	Ch5	Ch6	Ch7
P50m	321	359	368	340	390	213	242
N100m	-698	-453	-709	-553	-417	-517	-486
P200m	311	143	356	246	90	287	149

The channels that exhibit a clear P200m also show a subsequent negative deflection at ∼220-240 ms (c.f., Fig. 5.8) that could correspond to the onset of the SF. In order to properly record such low-frequency components in AEFs, the data should not be high-pass filtered above 0.5 Hz [12]. However, such a low cutoff frequency was
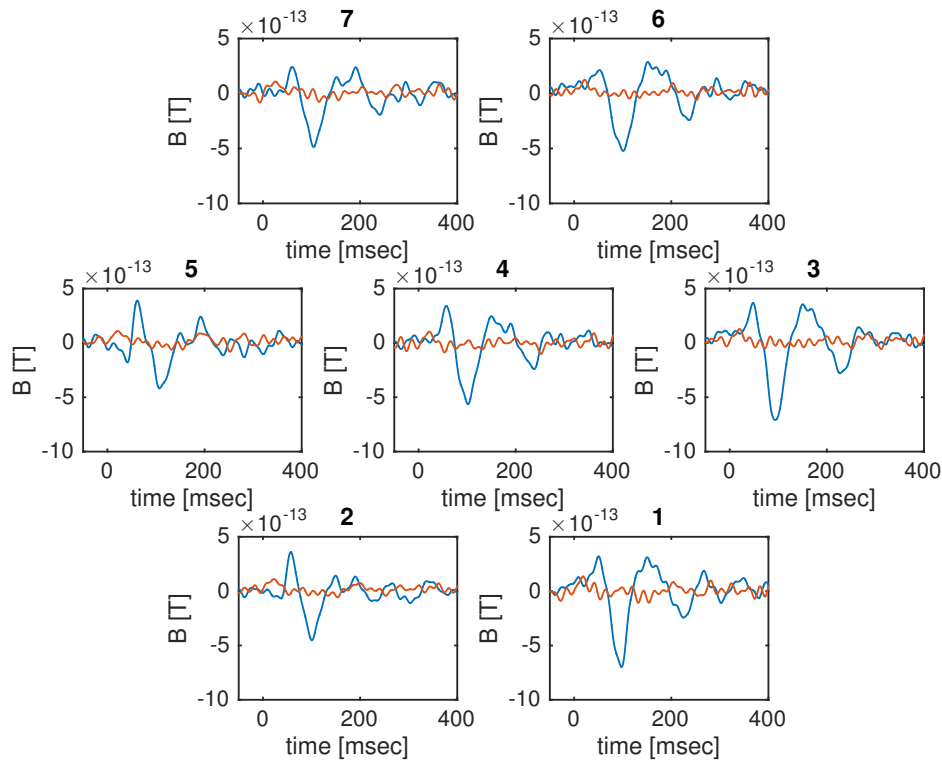
Figure 5.8: Time-locked average of auditory evoked activity recorded with 7-channel system (in blue) showing prominent deflections at ∼50, 100, and 150 ms. Time-locked averages of the difference between odd and even trials are shown in red.

impractical here due a combination of sensor 1/f-noise and low frequency field fluctuations inside the MSR. With a higher cutoff frequency, as done here, fast changes in the signal level, such as the onset of the SF, appear as a peak.

Topographic representations of the three main peaks can be seen in Fig. 5.9. The N100m as well as the P200m appear strongest in inferior, anterior channels (1 and 3), indicating the system was not optimally placed to record from the field minima/-maxima of the corresponding sources. Interestingly, while the two later peaks are lower in magnitude for the more posterior channels, especially the inferior, posterior channels (2 and 5), the early peak appears strongest in these and is generally higher in the inferior channels (1-5) compared to the superior ones (6 and 7). This variation in the positions of the field maxima points to different locations (or orientations) of the underlying sources, which is supported by literature [12].

Auditory evoked activity was recorded with the 7-channel system showing prominent P50m, N100m, and P200m components. The topographies of the main signal components indicate that the system may not have been ideally placed to capture the peak amplitudes. Additional recordings at multiple locations on the head (in order to map the neuromagnetic field over a larger area) could give a better idea of the the sources and the true peak amplitudes of the main auditory components.
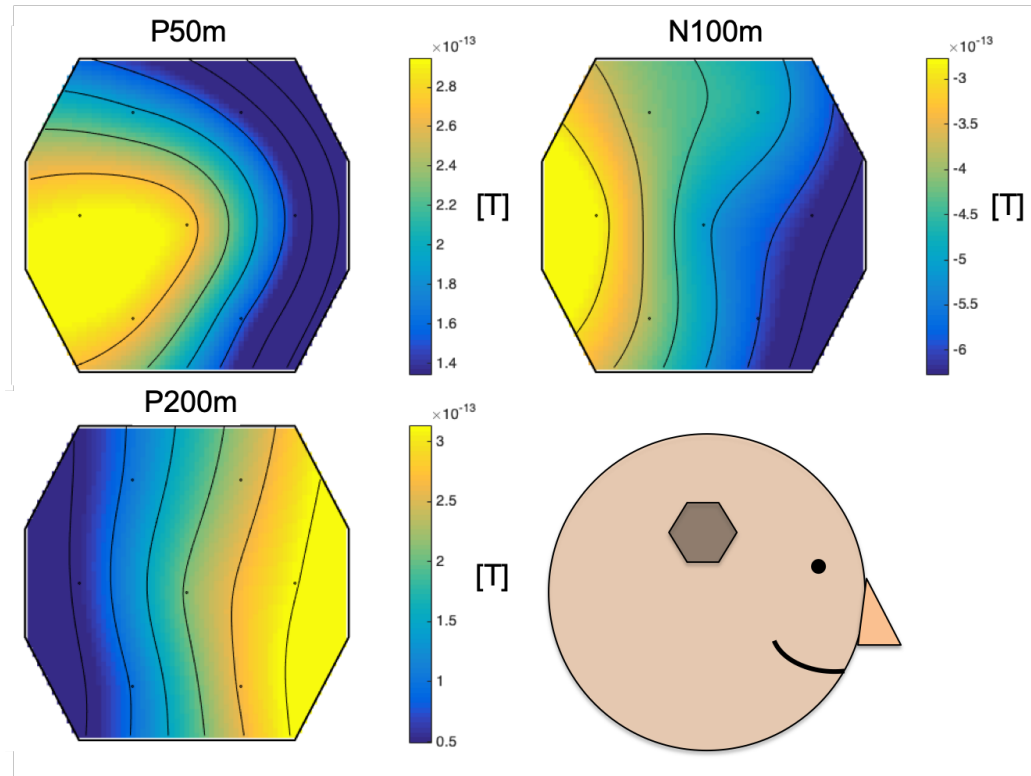
Figure 5.9: Topographic plots of the P50m (∼50 ms; top-left), N100m (∼100 ms; top-right), and P200m (∼150 ms; bottom-left) recorded with the 7-channel on-scalp MEG system. A sketch of the approximate recording position is shown at the bottom-right.

5.3 Benchmarking recordings

Objectively comparing high-T_c SQUID-based on-scalp MEG to conventional, low-T_c SQUID-based MEG is difficult in practice due to the large difference in coverage and channel count of available systems. Even with vastly superior sensor noise, a single-channel system could not compete with full-head systems sampling the field at hundreds of locations around the head. Comparisons are therefore mostly limited to the sensor level.

It is furthermore important to keep in mind that field patterns change at different distances from the scalp. As mentioned in §3.1, field patterns become more focal when moving closer to the sources. A simple radial projection of the sensor location from a conventional MEG recording to the scalp will therefore not necessarily give a fair comparison in terms of sampling of a given source/neural activation. A more unbiased comparison of the modalities can be achieved by recording the same features of the neuromagnetic field with both sensor technologies, e.g., the peaks of a dipolar field pattern [10].

To facilitate measurement of specific features of the magnetic field pattern, information from a conventional, full-head MEG recording can be used to guide the positioning of a single- or small multichannel on-scalp MEG system. Recording neu-

romagnetic responses with a conventional full-head system allows localization of the underlying neural sources by solving the inverse problem. Based on these sources, the field on the scalp can be calculated (by solving the forward problem) and used to aim the on-scalp MEG system [10]. Similarly, the projected field distribution can help guide the mapping of entire field patterns (e.g., a dipolar field) that can be used to localize activity. Because evoked activity is repeatable, the field can be sampled at different locations successively. However, as mentioned above, the neural response can change over time - as a result of changes in the stimulation (e.g., movement of an electrode in case of electric stimulation) or perception thereof (e.g., habituation or change in sleepiness). Minimizing the number of recording positions, and thereby the recording time, when capturing magnetic field patters is therefore crucial. By guiding on-scalp recordings with scalp-projected fields, components of interest can be sampled as efficiently as possible, i.e., with as few successive recordings as possible.

The benchmarking recordings were done in collaboration with neuroscientists at the Swedish National Facility for Magnetoencephalography (NatMEG) at the Karolinska Institute in Stockholm, Sweden. We compared our high-T_c SQUID-based single- and 7-channel on-scalp MEG systems (described in §4.2 and §4.3) to the conventional state-of-the-art, full-head system TRIUX (MEGIN Oy, Helsinki, Finland) at NatMEG. The TRIUX employs 306 sensors arranged in triplets at 102 fixed locations (∼35 mm distance between locations) inside a large, helmet-shaped liquid helium dewar. Each sensor triplet consists of two orthogonal planar gradiometers and one magnetometer on ∼28 mm ×28 mm chips. The sensors are separated from the inner wall of the helmet by approximately 2 cm of vacuum, radiation shielding, and super-insulation foil. The dewar can be rotated to allow measurements on subjects in seated as well as supine positions. Sensor data is sampled in the TRIUX with an internal 24-bit data acquisition system that allows up to 5 kHz sampling rate for all 306 channels, plus 12 auxiliary and many other input channels (e.g., for trigger, EEG, and physiological signals). Sensor signals from the on-scalp systems were recorded through the auxiliary analog input channels of the TRIUX data acquisition. The data was sampled at 5 kHz with 1.65 kHz anti-aliasing and 0.1 Hz high-pass filters. All recordings were performed inside the 2-layer MSR (two layers of mu-metal and 1 layer of copper-coated aluminum) at NatMEG (AK3b, Vacuumschmelze GmbH, Hanau, Germany).

In all of the recordings, 64-channel EEG was recorded in parallel, which allowed us to detect whether significant changes in the neural activity had occurred between the recordings as well as have an independent and consistent measure of the neural signals during both the TRIUX and the on-scalp MEG recordings. In most recordings, however, some of the electrodes had to be removed in order for them not to obstruct the placement of the on-scalp system on the head surface.

The TRIUX system contains a special, non-magnetic chair that allows rolling the subjects in and out of the MEG helmet. To minimize movement of the subject between TRIUX and on-scalp recordings, and thus the risk of the stimulation changing or EEG cap moving, the recordings were done in the same chair with an experimenter moving the chair with the seated subject between the two systems

Figure 5.10: Photographs showing the setup for benchmarking recordings. Left: 7-channel on-scalp MEG system with the full-head, conventional MEG system TRIUX (MEGIN Oy, Helsinki, Finland). Middle: A subject recorded in the TRIUX system. Right: A subject recorded with the 7-channel system. A vacuum pillow at the back of the subject's head stabilizes his head and neck in order to comfortably minimize head movement with respect to the on-scalp MEG system.

(Fig. 5.10). To minimize head movements during the on-scalp recordings, the subject's head was stabilized with vacuum pillows at the back and neck (see Fig. 5.10 - right).

Before each benchmarking recording, a shortened version of the same paradigm was run in the TRIUX system in order to localize the underlying sources and compute the subject-specific projected field pattern on the subject's scalp (see Fig. 5.11). The on-scalp measurement locations were chosen based on the projected field patterns. With the EEG electrode positions as a simple head surface coordinate system, the measurement locations were identified and marked with vinyl tags on (individually fitted) EEG caps to guide the positioning of the on-scalp system.

All experiments were approved by the Swedish Ethical Review Authority (EPN 2018-571-31-1) and conducted in compliance with national legislation and the code of ethical principles defined in the Declaration of Helsinki. The participants gave informed consent.
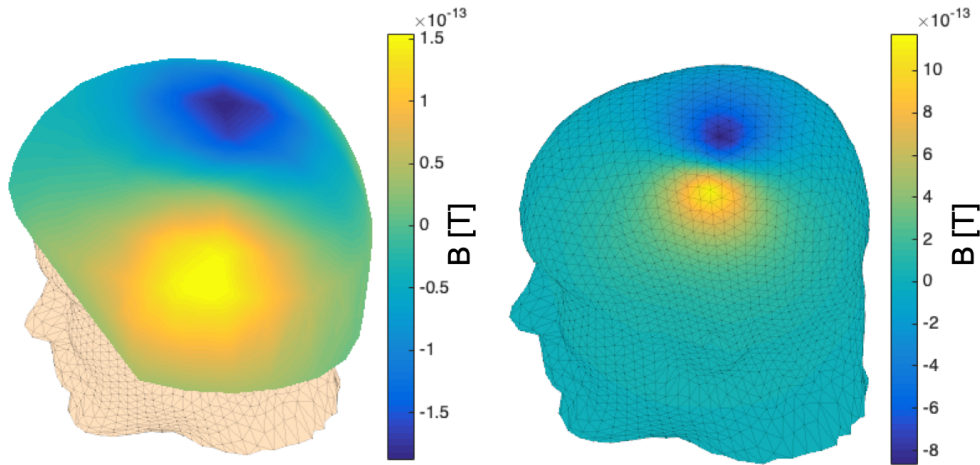
Figure 5.11: Field pattern (N20m) recorded with the TRIUX system (left) and projection onto a subject's scalp surface (right).

5.3.1 Somatosensory evoked fields - Part 1

Brenner et al. first recorded magnetic evoked responses of the somatosensory system with electrical stimulation of a finger in 1978 [95]. The somatosensory system, which is responsible for our sense of touch and pain, has since been intensively studied with MEG. Due to the variety of sensory receptors in the skin and the extent of the somatosensory system, evoked responses can be elicited in a number of different ways and at many different locations on the body. Directly stimulating sensory neurons electrically - something that is usually not possible for other senses - allows stable stimulation with high temporal accuracy, making it an ideal paradigm for evoked response averaging.

Inputs from sensory receptors travel through the spinal cord, brainstem, and thalamus before arriving at the contralateral primary somatosensory cortex (SI) [96]. Later activity can be observed bilaterally in the secondary somatosensory cortex (SII) and the posterior parietal cortex (PPC) [3], although it is not clear whether this activity is driven by the SI or represents parallel processing of the sensory inputs [97].

In the recordings included in this work, we focused on activity from SI, which is located in the walls of the central sulcus and parts of the postcentral gyrus [3] (c.f., Fig. 5.1). As Jasper and Penfield found already in 1954 [98] and later MEG recordings confirmed [99], the SI is somatotopically organized, that is, sensory inputs from different body parts connect to different parts of the SI. Roughly speaking, the more caudal body parts (e.g., legs) are represented more lateral in SI, while the more cranial ones (e.g., tongue) are more medial. The size of the cortical area (which can roughly be associated with the number of neurons therein) to which a given body part connects to is related to its sensitivity (c.f., Fig. 5.12).

Electrical stimulation of the median nerve is commonly used to evoke somatosensory activity due to its simple generation and large, robust cortical activation. Early components of electrical nerve stimulation responses in the SI can be seen after ∼20
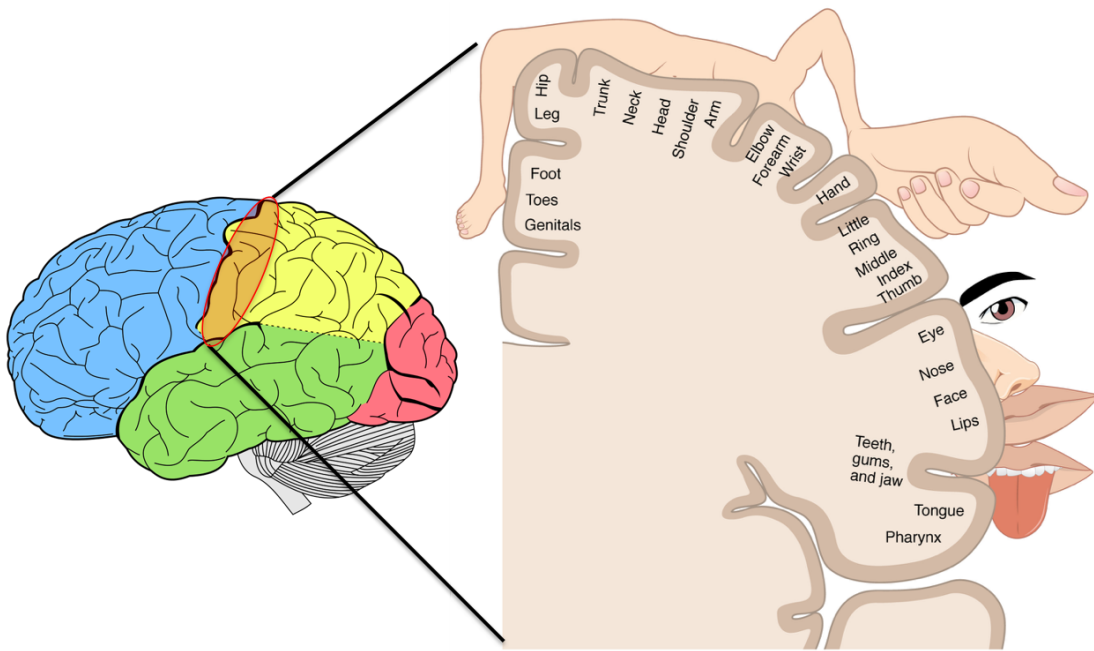
Figure 5.12: Sensory humunculus showing the regions of the primary somatosensory cortex that receive sensory signaling originating from different body parts. The relative size of the body parts indicate their relative sensitivity (i.e., the size of the cortical patch representing that body part). Adapted from [81] and [100].

ms (N20m) for upper limb and ∼40 ms, respectively, for lower limb. Evoked activity in SI continues up to approximately 200 ms with prominent deflections at ∼35 (P35m), 40 (N40m), and 60 ms (P60m) [101]. To record the early components of the somatosensory evoked response, the ISI should be 0.2 to 1 s [3]. The N20m is usually followed by a peak of opposite polarity around 35 ms after stimulus (P35m). The P35m is generated by a source more anterior than that of the N20m and is suppressed at short ISIs [102].

Somatosensory evoked fields with electrical median nerve stimulation were recorded with the single-channel system sampling from 10 head locations and with the full-head TRIUX in one male, neurotypical subject (presented in Paper V). The measurement locations were chosen evenly spaced on a line through the projected positive and negative field maxima of the N20m component to capture the dipolar pattern (see Fig. 5.11). The spacing between recording positions (12 mm) was chosen to emulate the sensor-to-sensor spacing of the 7-channel system (which was not operational at the time of these recordings). At each measurement location, the subject was presented with 1000 electrical pulses (6 mA, 200 µs duration) to the median nerve with a frequency of 2.8 Hz, corresponding to an ISI of ∼360 ms. Because of the high bit-depth, low input noise, and variable filter options of the TRIUX system's data acquisition, the on-scalp data was acquired directly, without additional analog amplification or filtering.

The recordings were segmented into epochs from 50 ms pre- to 200 ms post-stimulus, band-pass (5-200 Hz) and notch filtered (50 Hz and multiples up to

250 Hz). Before applying the filters, a window ($w(n) = 1 - hann(n) = 1 - sin^2(\pi n/N), 0 \leq n \leq N$) from -5 to 5 ms was applied to the TRIUX data in order to attenuate the large stimulus artifact. If the artifact were left untreated, it would have led to ringing artifacts throughout the dataset. The epochs were demeaned based on the pre-stimulus baseline. After rejecting noisy epochs (∼10 per recording position), they were averaged.

Time-locked averages of the evoked response can be seen in Fig. 5.13. The recordings show clear dipolar activity at ∼20 ms with ∼3.3-3.8 times higher peak amplitudes in the on-scalp MEG recording (∼920-950 fT) than in the conventional MEG recording (∼220-270 fT) - which is expected for this paradigm [10]. The measured fields showed slight temporal differences in peak latency whose origins could not be clearly identified [Paper V]. The field distribution might hint at a more complex underlying source [103], though that needs to be verified in further recordings.

In addition to the N20m, both recordings show a second deflection of the same polarity approximately 5 ms after the N20m. At about 40 ms the TRIUX recording shows a peak with opposite polarity that appears to be the P35m. At the same latency some of the on-scalp traces also show activity but it is not clear whether it corresponds to the P35m. Having recorded only at a few positions aimed at measuring activity from the N20m component, it is not surprising that activity from the P35m was not optimally sampled. As described above, the P35m is generated by a different, more anterior (∼10 mm) source than the N20m [102]. Since field patterns are more focal close to the head, the spatial overlap between field distributions from N20m and P35m are likely to become smaller when coming closer to the head surface.

The recordings clearly showed the limitations of recording MEG with a single-channel system. Even after recording nearly 10×1000 repetitions of the stimulus (which took several hours) the field was sampled only at 10 points along a thin line. With such a long duration, there is also the danger of the neural response changing between positions, which would have significant impact on the measurement.
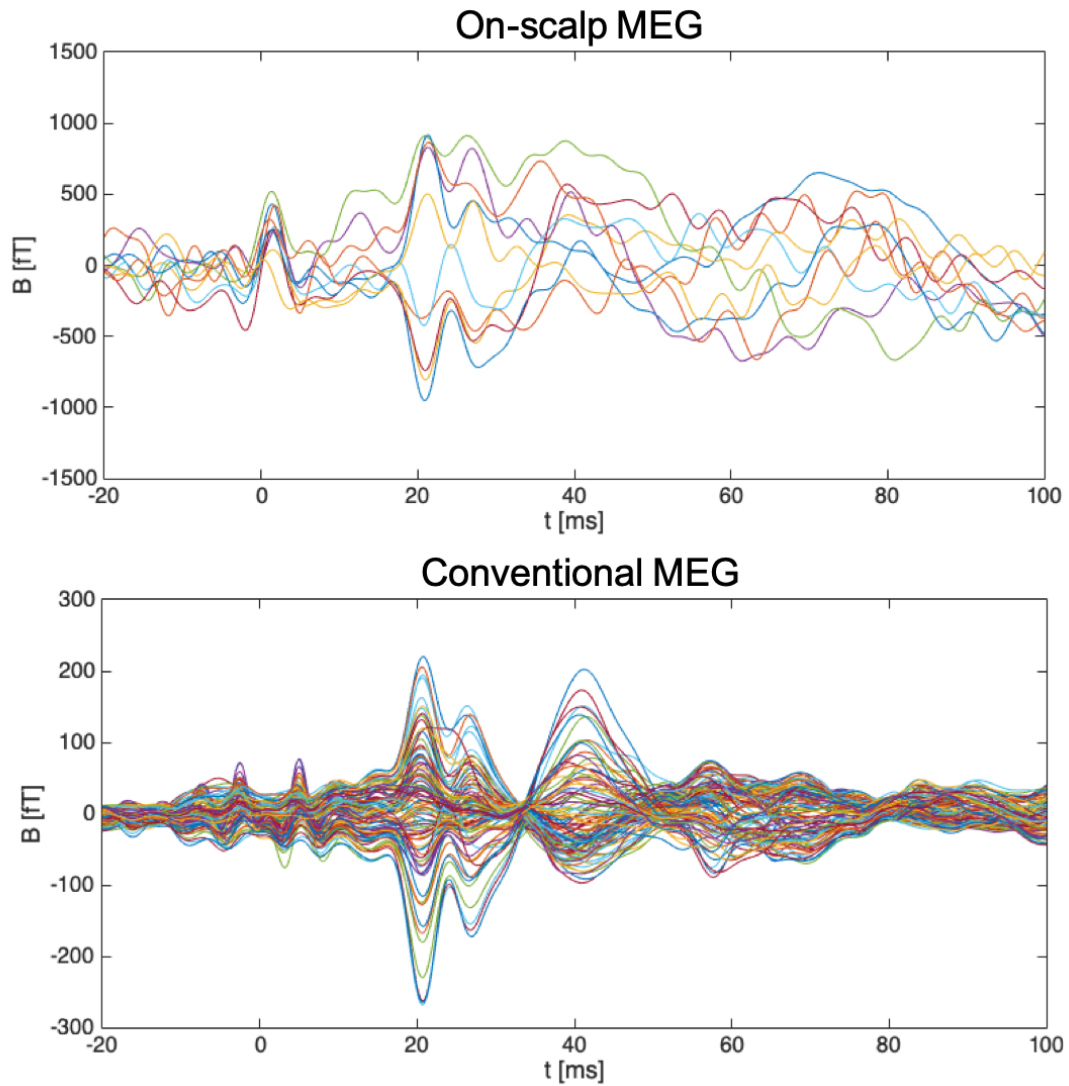
Figure 5.13: Somatosensory evoked responses to electrical stimulation of the median nerve recorded with the single-channel on-scalp MEG system at 10 positions (top) and recorded with the TRIUX MEG system (bottom). Only the magnetometers of the TRIUX system are shown for better comparability.

5.3.2 Somatosensory evoked fields - Part 2

Higher spatial sampling combined with closer proximity to the brain should, in theory, allow on-scalp MEG to better discriminate sources that are in close proximity to one another better as compared to conventional MEG (c.f., §3.1). One set of sources that are in close proximity to one another (while also being relatively easy to stimulate) are on the hand area of SI. Due to the somatotopic representation of the body, and thus the hand, on SI, stimulating different fingers is known to activate closely located sources in the primary somatosensory cortex that are discernible with conventional MEG [99]. Earlier components are significantly weaker in responses to tactile stimulation compared to electric stimulation. The first major activation (P50m) can be seen after ∼30-70 mm depending on the location of the stimulation site [99]. With the aim to investigate how well on-scalp and conventional MEG can discriminate between nearby sources, we recorded evoked responses to stimulation of different fingers as well as different phalanges on the same finger - which should activate even closer situated sources - with the 7-channel and the TRIUX systems. The recordings are presented in Paper VI, but will be briefly described here.

Four subjects (male, ages 30, 34, 39, and 49) were recorded with the TRIUX conventional MEG and the 7-channel on-scalp MEG systems. The underside of three phalanges on the subjects' right index finger (I1-3 with I1 the most distal and I3 the most proximal) as well as the most distal phalange of their right thumb (T1) and little finger (L1) were stimulated. A custom-built tactile stimulator using pneumatic valves controlling air flow to inflatable membranes attached to the subjects' phalanges was used to mechanically stimulate the individual phalanges with a very brief "tap" like sensation. The phalanges were stimulated 5000 times (1000 per phalange) interleaved in a pseudo-random order at a rate of 3 Hz (i.e., with an ISI of 333 ms). A full-head pre-recording of 1000 stimulations of I1 was used to project the P60m component onto the scalp surface (as described in §5.3). On-scalp MEG was then recorded with the 7-channel cryostat aimed (in succession) at the maximum and minimum of the scalp-projected fields for that P60m response to the pre-recording set of stimuli on I1. The signals from the 7-channel system were amplified (gain = 200) and filtered (1-5000 Hz) with the SQUIDamps before being digitized with the TRIUX system data acquisition. The recorded data was preprocessed in FieldTrip [55]. Two channels were excluded from the on-scalp MEG recordings due to high noise. The data was segmented into epochs from 30 ms pre- to 300 ms post-stimulus. To account for latency in the presentation of the stimulus, the data was time shifted 41 ms. The data was then filtered between 5 and 200 Hz. Trials with high variance were visually identified and rejected (∼50 trials with the significantly above average variance per recording). After rejecting noisy trials, the time-locked average response was calculated.

Because all four subjects showed similar responses, only the results for one subject (the 30-year-old) are presented here. For results from the other subjects see [Paper VI].

The time-locked responses for the five phalanges recorded with the on-scalp and conventional MEG systems are shown in Fig. 5.14. The magnetometers of the TRIUX system that recorded the highest negative (a) and positive (b) fields as well
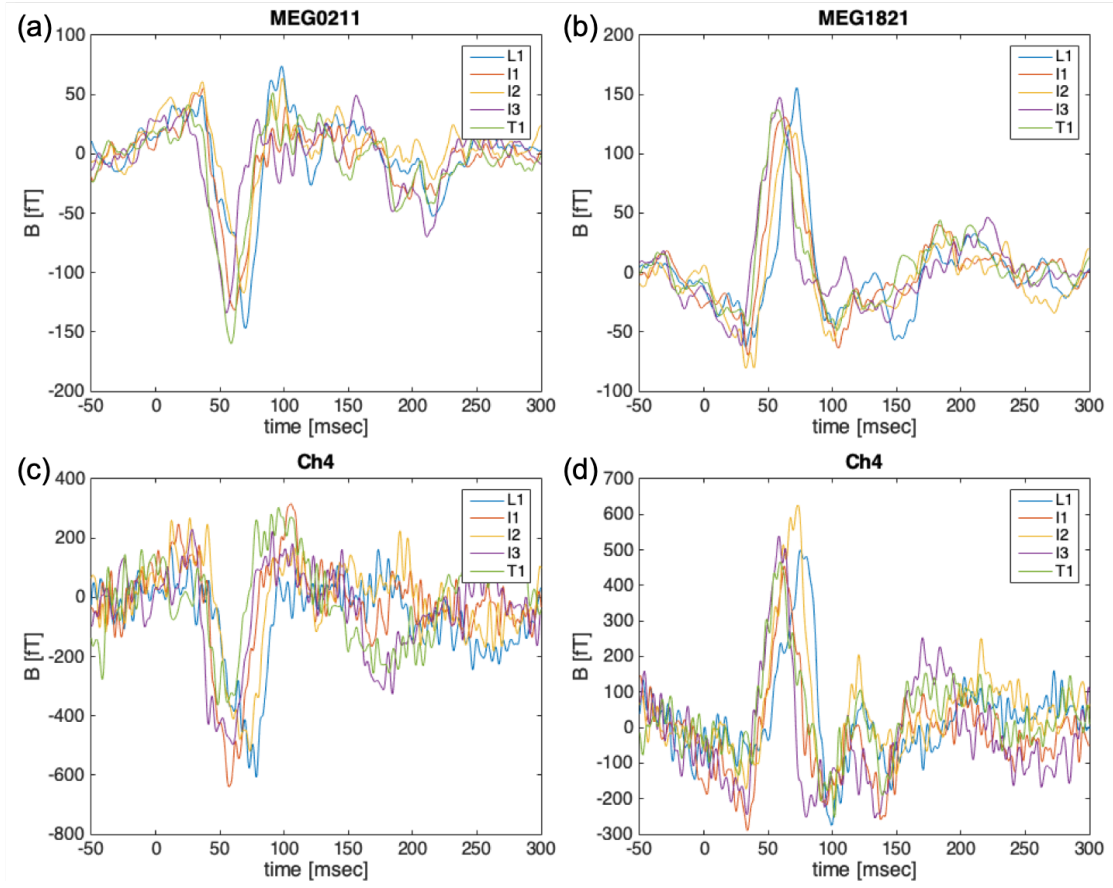
Figure 5.14: Evoked responses to tactile stimulation of different phalanges. *a) and b):* Evoked responses recorded with with the maximum (negative and positive, respectively) field sensing magnetometers of the TRIUX. *c) and d):* Evoked responses for five different phalanges recorded with the central magnetometer of the 7-channel system positioned on the negative and positive, respectively, field maxima.

as the central magnetometer (channel 4) of the 7-channel system for the recording at the negative (c) and positive (d) peak are shown. Clear P50m peaks can be seen ∼50-80 ms after stimulus. The P50m is preceded and followed by weaker activity with opposite polarity at ∼30 and ∼ 100 ms. The on-scalp recordings show similar signal shapes to the conventional MEG recording with comparable latencies and ∼3-5 times higher peak amplitudes (c.f., table 5.2). However, the on-scalp recordings also exhibit higher noise.

While both systems show clear differences between the responses for the different phalanges, it is difficult to conclude with certainty whether on-scalp MEG can better discriminate close sources than conventional MEG based solely on the recorded sensor signals. Properly comparing their ability to distinguish nearby sources would require source localization, for which proper co-registration is also necessary.

Table 5.2: Latencies and amplitudes of the negative (top) and positive (bottom) P60m peaks recorded with the 7-channel on-scalp and TRIUX conventional MEG systems.

		L1	**I1**	**I2**	**I3**	**T1**
CH4(N)	**Latency [ms]**	78	57	73	60	56
	Amplitude [fT]	-608	-640	-520	-497	-356
MEG0211	**Latency [ms]**	70	61	69	55	59
	Amplitude [fT]	-147	-132	-117	-134	-160
CH4(P)	**Latency [ms]**	75	62	73	58	59
	Amplitude [fT]	499	455	626	540	466
MEG1821	**Latency [ms]**	72	63	65	59	57
	Amplitude [fT]	156	131	124	148	137

5.3.3 On-scalp MEG co-registration

As with all MEG systems, accurate source localization with the 7-channel on-scalp MEG system requires co-registration of the neuromagnetic data with structural information of the subject's brain (c.f., §2.2.4). As part of the benchmarking recordings, we therefore tested the on-scalp co-registration using sensor localization described in §3.3. The results are presented in more detail in PAPER IV.

As mentioned in §3.3, localizing the on-scalp MEG sensors with an array of magnetic dipole-like coils requires knowledge of the coils' positions, orientations, and magnetic dipole moments. The position is straightforward as it is obtained as part of the head digitization process that is normally performed with MEG (described in §2.2.4). The actual magnetic dipole moment is furthermore only relevant for determining the sensitivity of the sensors themselves. If, for example, the coils are all geometrically identical and driven by equal magnitude currents (i.e., they have the same magnetic strength $|m|$), then this term is a constant prefactor in the localization procedure that can effectively be dropped. This is not, however, the case for the orientations of the coils. More specifically, since $\mathcal{L}_m(-r_{i,j}, m_j)$ depends linearly on $|m_j|$, the term for the calculated field in equation (3.9) is only scaled by the magnetic strength and the sensor sensitivities:

$$\mathcal{L}_m(-r_{i,j}, m_j)n_i = |m||n_i|\mathcal{L}_m(-r_{i,j}, \hat{m}_j)\hat{n}_i. \tag{5.1}$$

If the sensor sensitivity is known beforehand, then the magnetic strength can be ignored. The orientations of the coils (which are important in this procedure) are, however, more complicated to determine. Fortunately, as the benchmarking recordings included recordings with a full-head system, it was possible to use the coil orientations obtained from conventional head localization [104] with the TRIUX system (the HPI coils were kept in position on each subject's head for both the TRIUX and on-scalp MEG recordings). In the future, this could be circumvented by using coils that are designed to enable easy determination of their orientation based on their geometry (c.f., Fig. 5.15).

In each of the recordings, 10 HPI coils were attached to the subject's head. To ensure high signals, the coils were arranged closely around a rough region of interest
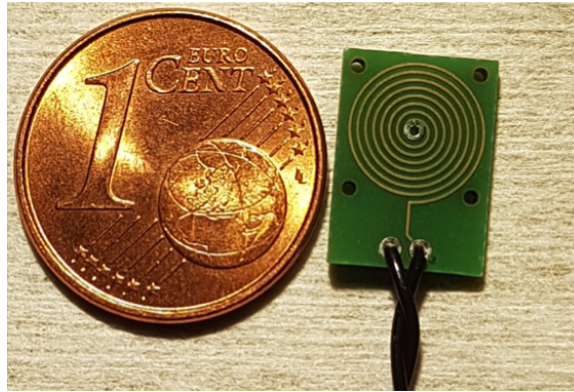
Figure 5.15: A flat, dipole-like PCB coil that could be used to digitize both the position and orientation of the coils used for on-scalp MEG co-registration (coil orientation is difficult to determine with conventional HPI coils). Digitizing the four indentions near the edges allows determining the PCB surface along with the center of the coil. The normal of the PCB surface would then correspond to the orientation of the coil.

for the on-scalp recording. Nine coils were fixed in triplets to small plastic plates that were curved to match the subject's head. The tenth coil was fixed to the head individually. We fixed multiple coils to a common plate in order to minimize their movements relative to each other - which would corrupt the sensor localization. The coils were driven with sine waves at 537 to 987 Hz in steps of 50 Hz. The relatively high coil frequencies allow measurement of neural activity up to ∼500 Hz without direct interference from the coil signals. As a result of the 50 Hz separation, intermittent-frequency artifacts fall onto the (50 Hz) power line harmonics that are normally filtered in preprocessing. The coils were powered for 10 to 30 seconds before and after each set of stimulations during the on-scalp recordings (longer recordings were split into multiple shorter sets). The subjects were instructed to keep their head still during the stimulation and coil recording sets, but were free to move their head during breaks. We decided not to run the coils during stimulation as a cautionary measure to ensure integrity of the neural recordings. As the frequency spectrum of such a coil recording (Fig. 5.16) shows, this step was most likely not necessary as no artifacts from the coils were seen below 500 Hz.

The coil amplitudes were extracted from the signals using multitaper frequency transform (DPSS tapers). The sensors were then fitted to the data (as described in §3.3) in MATLAB R2015a (Mathworks, Natick, MA, USA) using FieldTrip [55]. The fits were carried out in two steps; first, a grid search was performed to get a rough fit, then the rough fit was refined with a non-linear search (using a Quasi-Newton algorithm). Fig. 5.17 shows an example of one of the resulting sensor fits.

During the recordings, the subjects' heads were stabilized with vacuum pillows and the subjects were instructed to keep their head still. We therefore assume head movements during the recording of the coil signals to be negligible (<1 mm). To estimate the accuracy of our sensor localization method, a 30-second recording of the coil signals was split into multiple, shorter trials and the sensor localization was run on each trial individually. Without head movements, the spread of the resulting
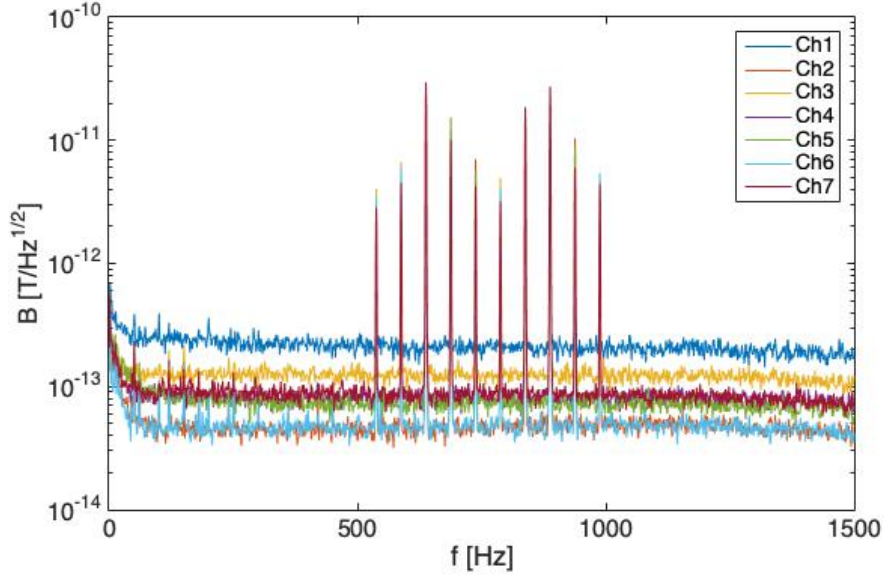
Figure 5.16: Frequency spectrum of the magnetic fields recorded when the HPI coils were powered for co-registration. Strong peaks can be seen at the coil driving frequencies. [Paper IV]

sensor positions and orientations corresponds to the random error in the localization. We therefore define $MD(\boldsymbol{r}_{i,k}) = ||\boldsymbol{r}_{i,k} - \bar{\boldsymbol{r}}_i||$ as the deviation of the k-th fitted position of sensor i from the mean. Analogously, we define the angular deviation of the k-th fitted orientation of sensor i from the mean $aMD(\boldsymbol{n}_{i,k}) = 2 \arcsin(||\boldsymbol{n}_{i,k} - \bar{\boldsymbol{n}}_i||)/2$. MD and aMD for different lengths of coil recording trials can be seen in Fig. 5.18 a) and b).

Random localization errors decrease - especially in the noisy channel 1 - with increasing trial length. This agrees with the finding from simulations (described in §3.3), where longer coil recordings improved localization accuracy. Even with just 1-second trials, the localization errors were well below the 4 mm and 10 degrees thresholds recommended by Zetter et al. for accurate source reconstruction with on-scalp MEG [54]. All channels showed average MD below 2 mm and aMD below 3 degrees.

As the recordings were performed with the 7-channel on-scalp MEG system, which employs seven sensors fixed relative to each other in a common housing, it is possible to localize the sensors jointly based on the known geometry of the sensor array. As shown in §3.3, jointly fitting the sensors should provide improved accuracy. Fig. 5.18 c) and d) shows MD and aMD for the same data when fitting the sensors jointly. The noisy channel 1 shows greatly reduced localization errors. However, the localization errors increased slightly for the channels with the lowest noise (2 and 6). It is thus apparent that such a joint localization procedure induces a noise normalization-like process wherein the accuracy with which low- and high-noise sensors are localized is pushed towards the mean. However, on average, random localization errors decrease as expected, showing average MD <1 mm and aMD <2 degrees with 1-second trials.
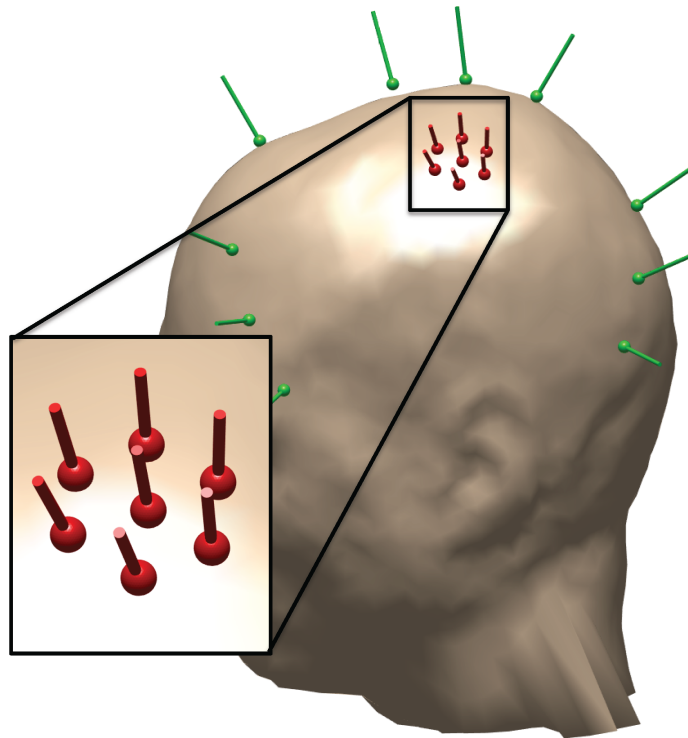
Figure 5.17: Co-registration results of the 7-channel system for an on-scalp MEG recording. Localized on-scalp sensors (red dots mark their positions, lines indicate their orientations) on the head of a subject. HPI coils are shown in green. [Paper IV]

Even on-scalp systems consisting of multiple, movable single sensor units could benefit from joint sensor localization. If the sensors stay fixed during the recording, the sensor array can be calibrated by running an individual localization procedure over a longer period (e.g. 10 seconds). The resulting sensor array can then be used as the basis for jointly fitting the sensors at subsequent times (assuming the coils do not move with respect to the head or each other in between), thereby enabling high accuracy with shorter trials. We tested this approach with the 7-channel on-scalp MEG system. This resulted in a localization accuracy improvement over individual localization that was on the same order as when using the known geometry of the sensor array.

To conclude, the sensor localization method described in §3.3 was implemented in MEG recordings with the 7-channel on-scalp MEG system. The method enables localizing the sensors with high accuracy in position (<2 mm) and orientation (<3 degrees) with 1-second trials. High accuracy with short trials means the sensor locations relative to the head can be sampled at a high rate. Combined with the ability to record in parallel to neural recordings (although this remains to be verified), this makes the method suitable for continuous co-registration, which is highly advantageous when recording with the subject's head is free to move during a given session, as was the case for our benchmarking recordings. The sensor array can furthermore
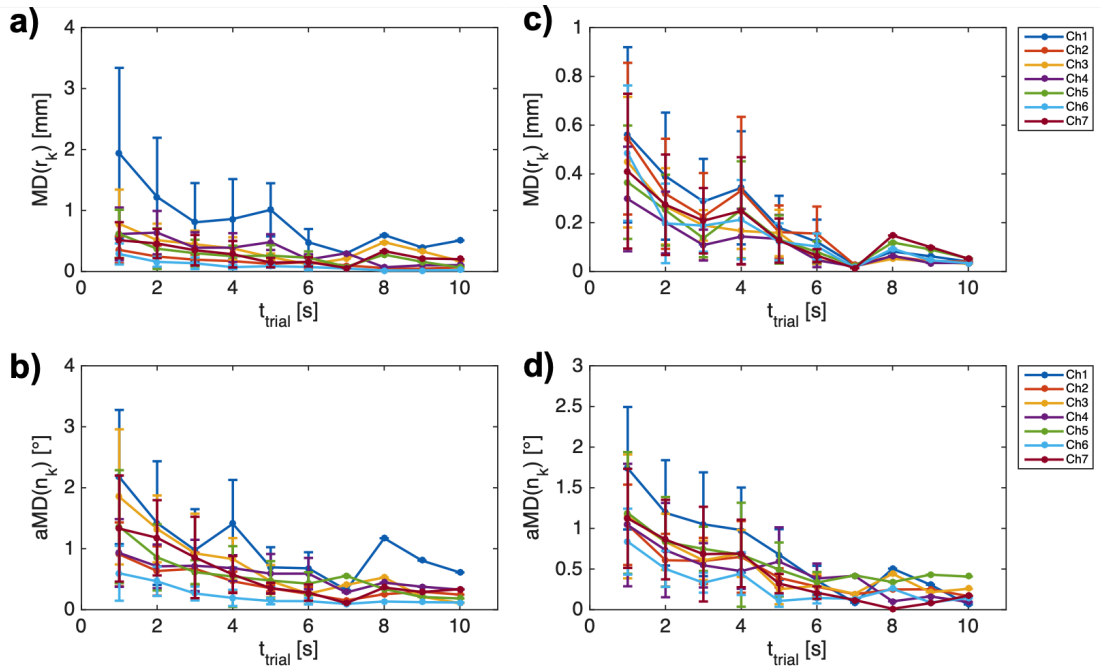
Figure 5.18: Random localization errors in on-scalp MEG co-registration. a) and b) deviation of position MD and orientation aMD of individually fitted sensors from the mean as a function of trial length. c) and d) deviation of position MD and orientation aMD of jointly fitted sensors from the mean as a function of trial length. Error bars indicated one standard deviation.

be calibrated with a longer recording, which enables a significant improvement in the co-registration accuracy (<1 mm and <2 degrees errors in sensor position and orientation, respectively).

5.3.4 Somatosensory evoked fields - Part 3

With a practical method for on-scalp co-registration in place, somatosensory responses to electrical stimulation of the median nerve were recorded with the 7-channel on-scalp MEG and TRIUX systems in a healthy subject (male, 39 years old). The paradigm comprised of >1000 electrical pulses delivered to the right median nerve with an ISI of 360 ms. To ensure strong responses, the amplitude of the electrical stimulation was chosen just below the motor threshold of each subject. The evoked fields were recorded with the 7-channel system positioned at four locations along the line spanned by the projected positive and negative field extrema (c.f., Fig. 5.20-left). Recording the evoked fields at four different locations was done with the intention of localizing the neural activity - specifically the neural source generating the N20m. The SQUIDamps were used to amplify (gain = 200) and filter (1 - 5000 Hz) the signals from the 7-channel system before data acquisition. With FieldTrip [55] the sensor signals were band-pass filtered between 5 and 200 Hz with notch filters applied at multiples of 50 Hz. As in the single-channel recording, the stimulus artifact had to be manually attenuated in the TRIUX recording. The signals were then epoched relative to the trigger input (-50 to 200 ms), demeaned

according to the pre-stimulus baseline (-50 to -5 ms), and averaged.

Fig. 5.19 shows time-locked averages of the evoked responses recorded with the 7-channel on-scalp MEG system positioned at four different head locations (top) as well as with the TRIUX system (bottom; single, full-head recording) in one subject. When recording with the 7-channel system, one sensor (channel 3) showed excessive noise as a result of flux trapping and was therefore excluded (from all four recordings). Only the magnetometers of the TRIUX system are shown here for better comparability.
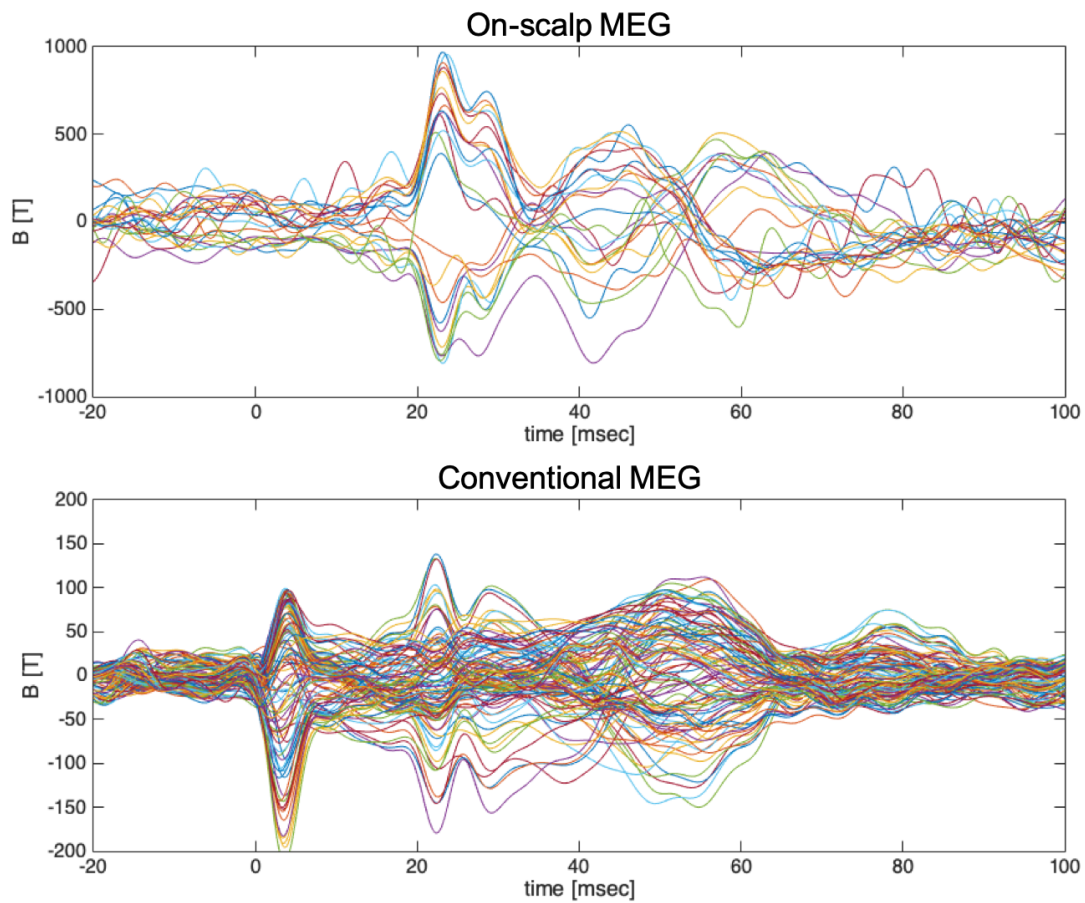

Figure 5.19: Evoked responses to electrical median nerve stimulation. Top: 24 SEF traces recorded with the 7-channel on-scalp MEG system at four head locations (channel 3 was excluded at all four locations due to excessive sensor noise). Bottom: 102 SEF traces recorded with the magnetometers of the TRIUX conventional MEG system.

Both recordings show clear N20m peaks at 22 ms (TRIUX) and 23 ms (7-channel system), respectively, relative to the stimulus. As before with the single-channel recordings, a second deflection with the same polarity can be seen shortly after the N20m (both at 29 ms). Thereafter, both recordings show weaker activations (with the same polarity) at around 40 ms. At a post-stimulus latency of approximately 50-60 ms, both recordings show deflections with opposite polarity relative to the

N20m, which could match the P60m. Ranging between -810 and 970 fT, the N20m peaks in the on-scalp recording are approximately 4-7 times higher than the ones recorded with conventional MEG (roughly -180 to 140 fT). This gain exceeds the one expected for somatosensory activity, which is 3.4-4.2 [10]. However, the comparatively large size of the TRIUX sensors could lead to a blurred observation of the field (a SQUID magnetometer measures the integral of the field over the loop area), which would result in a distorted gain. Also worthy of note is that, in contrast to the TRIUX recording, the 7-channel data does not show a stimulation artifact at 0 ms.

Using the method described in §5.3.3, the sensors of the 7-channel system were localized in order to co-register the recorded data with a structural MRI of the subject's head. The positions and orientations of the sensors can be seen in Fig. 5.20-left. Different recording locations are indicated by color (red, blue, green, and black). Channel 3, which was excluded due to high noise, is marked grey at all four locations. The positions and orientations of the TRIUX sensors relative to the subjects head are shown in Fig. 5.20-right. The TRIUX data was co-registered using conventional head localization.
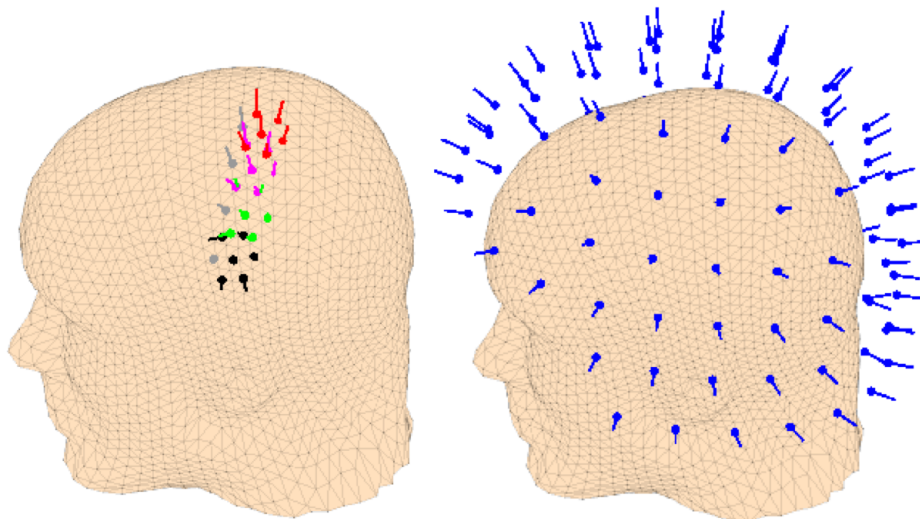

Figure 5.20: Sensor locations. *Left*: Sensor locations and orientations from four consecutive recordings with the 7-channel on-scalp MEG system. Colors indicate the different recording positions. The excluded channel 3 is marked grey in all four locations. *Right*: Sensor positions and orientations of the TRIUX magnetometers. Two planar gradiometers are positioned at each magnetometer location (not shown here).

The obtained on-scalp sensor locations were used to visualize the topographies of the activations at $\sim$22, 29, 40, and 60 ms (Fig. 5.21). The two early deflections show similar, dipolar topographies in both systems. The location of the dipole-like pattern matches the expected location of the N20m for median nerve stimulation. At 40 ms, the position and/or orientation of the dipolar activity appears to have shifted. Both in the TRIUX and the 7-channel recording, the field minimum seems to have moved anterior. The TRIUX topography shows additional activity in the
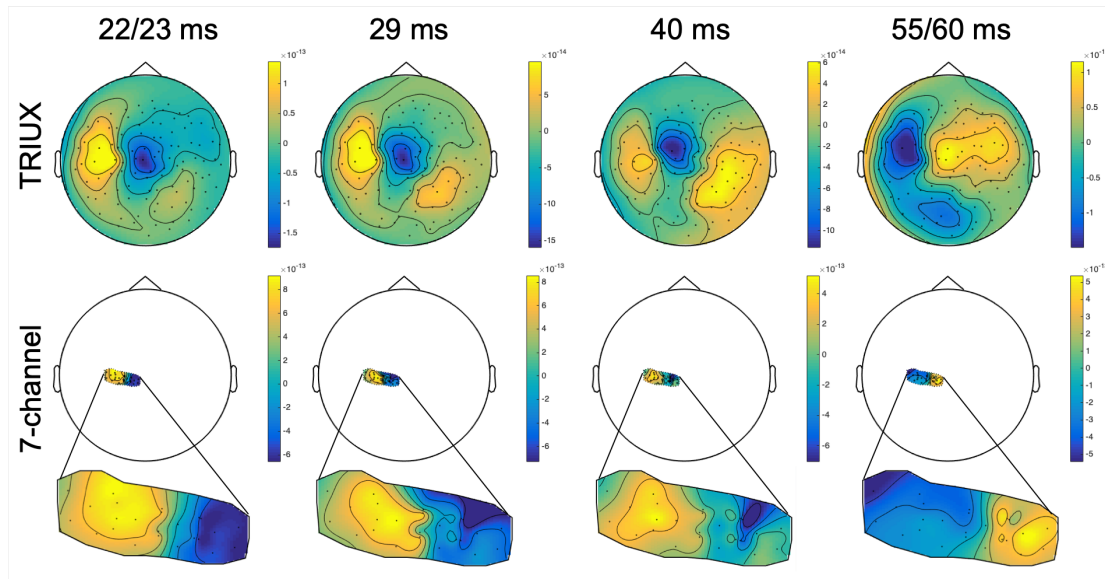
Figure 5.21: Topographies (polar projection) of the somatosensory evoked fields recorded with the TRIUX (top) and 7-channel (bottom) systems at 22/23, 29, 40, and 55/60 ms (left to right).

right posterior part of the head. At 55 and 60 ms, respectively, both systems show dipolar field patterns in the same area as at 22-29 ms, but with opposite polarity. Generally, the on-scalp topographies show similar trends compared to the topographies recorded with the full-head system. However, direct comparison is complicated by the differences in sensor-to-scalp distances.

Projecting the N20m fields recorded with the full-head system to the locations of the on-scalp measurement furthermore shows that the recorded fields match well with theory (c.f., Fig. 5.22). The projection was obtained by computing the forward solution of an ECD that had been fitted to the N20m component recorded by the TRIUX system.

Finally, the co-registered evoked data (4×6 channels) from the on-scalp recordings was combined and used to fit a current dipole source for the N20m component. Analogously, a current dipole was fit to the N20m component recorded with the TRIUX system. The two fitted current dipoles can be seen in Fig. 5.23. Both dipoles are located in the primary somatosensory cortex and are thus within the expected brain region for median nerve stimulation (c.f., Fig. 5.12); The Euclidean distance between them was 4.2 mm, which is well within that between different conventional full-head systems (8-11 mm [105]).

In general, the temporal evolution of the fields and corresponding topographies at latencies of interest matched well with those recorded with the state-of-the-art full-head system. Furthermore, the on-scalp MEG co-registration method described in §5.3.3s was critical for source localization with our 7-channel system, yielding a source whose position was only ∼4 mm from that which was obtained with the full-head system. This is remarkable considering the significantly smaller coverage of the 7-channel system.
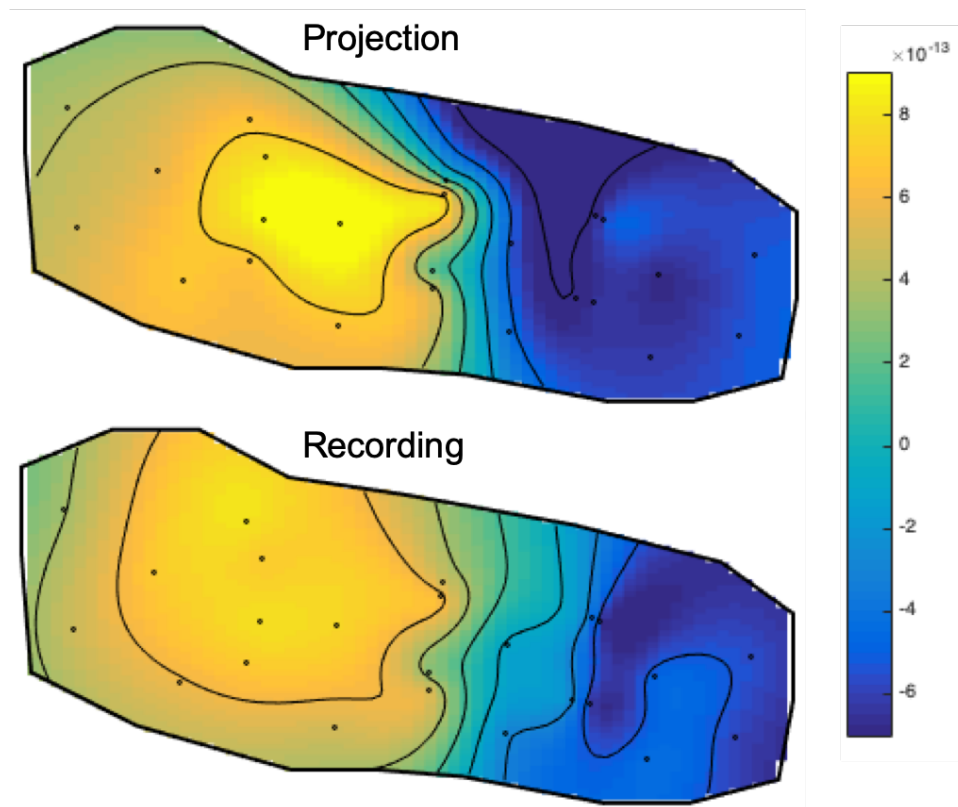
Figure 5.22: Topographies (polar projection) of the N20m field at the on-scalp measurement locations. *Top:* The on-scalp field calculated from the TRIUX (full head) recording. *Bottom:* The onscalp field recorded with the 7-channel system.

Three additional subjects (in total, we recorded the same four subjects as in §5.3.2) were recorded using the same stimulus paradigm (but only two on-scalp recording positions each). The data from these recordings and those described in the following require further analysis.
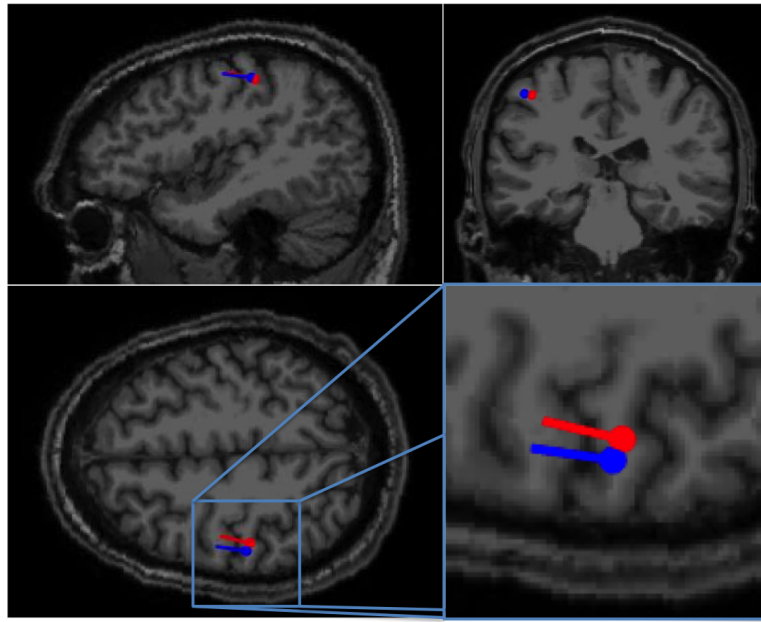
Figure 5.23: Source localization of N20 component recorded with on-scalp (red, 4×6 channels) and conventional, full-head MEG (blue, 306 channels) [PAPER IV].

5.3.5 Additional recordings

Several other benchmarking recordings targeting different neural activities were performed in addition to the previously mentioned ones. Analysis of the recorded data is ongoing. A short summary of the recorded paradigms is given below.

- Electric median nerve stimulation with high ISI and large number of stimulations ($\sim$15 000) in four subjects to investigate high frequency oscillations (HFOs) superimposed on the evoked N20m peak. HFOs at $\sim$600 Hz have been recorded with conventional MEG [106, 107] as well as EEG [108]. Their sources have been localized in the SI close to the source of the N20m [106] showing similar somatotopic arrangement [107]. HFOs may be generated by action potentials [17].

- Auditory stimulation at a fixed ISI and with eventual omission of individual stimuli in three subjects to investigate AEFs and expectation. Omission of expected auditory stimulation is known to evoke activity in the same region of the auditory cortex as actual stimulation [109].

- Visual stimulation with concentric, moving rings at different speeds in four subjects to investigate visual gamma activity. Gamma activity is modulated by visual motion with both frequency and power of the induced gamma depending on the speed of motion [110]. Preliminary analysis of the recorded data was promising and additional gamma recordings are planned.

- Resting state (i.e., without stimulation) activity in an epileptic patient to investigate spontaneously occurring interictal spikes. Hereto a patient with regularly occurring interictal spikes was recruited in order to record as many spikes as possible in the limited recording time. Interictal spikes are used to localize epileptic foci, the origin of epileptic seizures. Along with presurgical

mapping, the localization of interictal spikes is to date the main clinical application of MEG [3]. To our knowledge, the recording marks the first on-scalp MEG recording of epileptic activity in humans. A manuscript (first author: Karin Westin) on this data is in preparation.

6

Conclusions

To guide the design of future systems ,different layouts for full-head on-scalp MEG were evaluated and compared to each other. Even with inferior sensor noise levels ($\sim$10$\times$ worse) all the simulated on-scalp MEG systems tested extracted significantly more information than the conventional MEG system. Spatial information density (SID) - a metric for evaluating the spatial origin of information in full-head MEG systems - was developed. SID revealed a spatially inhomogeneous distribution of the obtained information that was especially pronounced for a child subject. This work has been continued in a master's thesis project wherein a number of additional system designs were compared [111]. Both SID and information capacity are independent of the sensor type, making them also useful for the optimization of OPM-based on-scalp MEG systems. Such theoretical work not only produced interesting results, but also helped us verify that we were on the right track regarding the design of the 7-channel on-scalp MEG system, the construction of which was ongoing while this work was performed. It also laid the foundation for the practical steps and important concepts in relation to the basis of MEG recordings and analysis that supported the following, more practical developments.

A method for localizing MEG sensors in on-scalp MEG was devised, evaluated in simulations, and tested in MEG recordings on human subjects. The method overcomes the co-registration problem in flexible on-scalp MEG systems wherein localizing each sensor with respect to the head was challenging. With high accuracy (<1 mm and <2 degrees) for short averaging times (1 second), it can also be used for continuous co-registration, allowing compensation for head movements during MEG recordings. The method is also independent of sensor technology, making it suitable also for, e.g., OPM-based on-scalp MEG. The code implemented in MATLAB will be published along with Paper IV.

In parallel, a 7-channel high-T_c SQUID-based on-scalp MEG system was developed. It is the first integrated multichannel high-T_c SQUID-based on-scalp MEG system and marks the latest step towards full-head on-scalp MEG with high-T_c SQUIDs. The sensors are placed at millimeter distance from the head. Because field patterns are more focal closer to the head (c.f., §3.3), the system was designed for high spatial sampling ($\sim$12 mm sensor center-to-center spacing). Good field sensitivity ($\sim$50-130 fT/HZ$^{1/2}$ down to $\sim$ 8 Hz; c.f., Fig. 4.7) combined with low cross-talk (<0.5%) allows us to record neuromagnetic fields reliably.

Proof-of-principle recordings of alpha and auditory evoked activity were performed with the 7-channel system to test its feasibility for on-scalp MEG. In addition to the expected modulation of the alpha power, the alpha recording revealed two distinct alpha bands that showed different behavior. Topographic plots furthermore point

to different locations for the neural sources of these bands. The two bands could correspond to the ones observed with EEG by Klimesch et al. [88]. Additional recordings with more subjects could help shed more light on the nature of these two alpha bands.

The auditory recording clearly showed the expected neural signal components (P50m, N100m, and P200m). The onset of the sustained field was furthermore observed in several channels, although this could not be verified. Topographies of the main signal components showed that the measurement location was not optimally placed to record the maximum field amplitudes. In future recordings, it would be advantageous to record at more locations to map a larger area. With such a larger field map, one could get a better idea about the location of the underlying sources.

Having demonstrated successful proof-of-principle on-scalp MEG recordings, we performed a number of benchmarking recordings against a commercial, state-of-the-art conventional MEG system in collaboration with scientists at the Karolinska Institute in Stockholm, Sweden. A first set of benchmarking recordings with the single-channel on-scalp MEG system was done early on, giving us a chance to get familiar with and optimize the necessary and rather complicated procedures. Here, we recorded somatosensory responses to electrical stimulation of the median nerve. Both recordings showed a clear N20m peak with the on-scalp one being approximately 3.5 times higher in field magnitude.

Subsequently, we performed a number of benchmarking recordings with the 7-channel on-scalp MEG system using different simulation paradigms. By comparing recordings of tactile stimulation to different phalanges, we found clear P60m components with comparable latencies and ∼3-5 higher field amplitude with the 7-channel system, as compared to the conventional system.

New recordings with the same median nerve stimulation paradigm as that which we used for the single-channel system, clear N20m and P60m components were observed with both systems. Thanks to the improved coverage of the 7-channel system, we could visualize the field topographies of the main components of the neural responses and found that they matched well with expectations. Combining multiple recordings with the 7-channel system and using the previously developed on-scalp co-registration method enabled source localization on par with the commercial, full-head system (<5 mm disagreement).

Recordings of four additional paradigms are presently being analyzed by collaborators at the University of Gothenburg and the Karolinska Institute. Manuscripts about several of these are currently in preparation. The recording of epileptic activity is, to my knowledge, the first of its kind with on-scalp MEG. It is of especially high interest due to the fact that localizing epileptic foci is, to date, the main clinical application of MEG.

6.1 Outlook

The 7-channel on-scalp MEG system is a first step on the path to full-head on-scalp MEG. Experiences from its construction and use in MEG recordings can help guide the design of future generations of high-T_c SQUID-based on-scalp MEG systems. Such systems should cover a larger area (ultimately the whole head) without com-

promising on dense spatial sampling or sensor-to-head separation - which were both shown to be critical in on-scalp MEG (c.f., §3.1). High-T_c SQUID magnetometers with flux transformers could further improve the sensor noise.

The sensor localization method should also be further refined to be useful for future systems. Most importantly, the problem of establishing the orientation of the coils in a standalone setup needs to be addressed. Coils specially designed to enable digitizing their orientation as part of the standard head digitization step could solve this issue (c.f., Fig. 5.15). Such coils along with a driver have been designed and built but still need to be tested.

The results from the on-scalp recordings look very promising for the technology. The recorded signals were rich in detail. In addition to the features that were expected based on knowledge from conventional MEG recordings, we observed unpredicted details in several of the experiments, the origins of which could not be clearly explained. For example, the two alpha bands we identify (c.f., §5.2.1) seemed to originate in spatially separate brain regions. While small, the non-negligible differences in the timing of early neural responses to somatosensory stimuli (c.f., §5.3.1 and §5.3.2) indicate on-scalp MEG may provide a more fine-grained picture of brain activity in both space and time. And while preliminary and thus not presented herein, initial analysis of both visual gamma and epileptic interictal spikes have produced entirely unexpected results. These unexpected results (preliminary and otherwise) may reflect some to date undocumented brain activity. We theoretically predicted that a full-head on-scalp MEG system can reveal new information about the inner workings of the brain (c.f., §3.2); perhaps our 7-channel is doing so already. The next steps in investigating and understanding such open questions are thus less technical and more analytical and neurophysiological in nature.

The recordings presented in this work only scratch the surface of the possibilities that on-scalp MEG offers. Future work should put effort into the search for, and investigation of, novel information by means of more MEG recordings. In this respect, it is essential to continue and expand collaboration with neuroscientists and clinicians. In order for on-scalp MEG to transition from mere proof-of-concept to having a real world impact, the technology needs to mature to the point where neuroscientists and clinicians are the drivers for future experiments.

Acknowledgements

Bibliography

[1] R. Hari and R. Salmelin, "Magnetoencephalography: from SQUIDs to neuro-science: Neuroimage 20th anniversary special edition," *Neuroimage*, vol. 61, no. 2, pp. 386–396, 2012.

[2] S. Baillet, "Magnetoencephalography for brain electrophysiology and imaging," *Nat. Neurosci.*, vol. 20, no. 3, p. 327, 2017.

[3] R. Hari, S. Baillet, G. Barnes, R. Burgess, N. Forss, J. Gross, M. Hämäläi-nen, O. Jensen, R. Kakigi, F. Mauguière, *et al.*, "IFCN-endorsed practical guidelines for clinical magnetoencephalography (MEG)," *Clin. Neurophysiol.*, 2018.

[4] D. Cohen, "Magnetoencephalography: evidence of magnetic fields produced by alpha-rhythm currents," *Science*, vol. 161, no. 3843, pp. 784–786, 1968.

[5] T. S. Lee, Y. R. Chemla, E. Dantsker, and J. Clarke, "High-Tc SQUID micro-scope for room temperature samples," *IEEE Trans. Appl. Supercond.*, vol. 7, no. 2, pp. 3147–3150, 1997.

[6] F. Öisjöen, J. F. Schneiderman, A. P. Astalan, A. Kalabukhov, C. Johans-son, and D. Winkler, "A new approach for bioassays based on frequency-and time-domain measurements of magnetic nanoparticles," *Biosens. Bioelectron.*, vol. 25, no. 5, pp. 1008–1013, 2010.

[7] J. Iivanainen, M. Stenroos, and L. Parkkonen, "Measuring MEG closer to the brain: Performance of on-scalp sensor arrays," *Neuroimage*, vol. 147, pp. 542–553, 2017.

[8] E. Boto, R. Bowtell, P. Krüger, T. M. Fromhold, P. G. Morris, S. S. Meyer, G. R. Barnes, and M. J. Brookes, "On the potential of a new generation of magnetometers for MEG: a beamformer simulation study," *PLoS One*, vol. 11, no. 8, p. e0157655, 2016.

[9] F. Öisjöen, J. F. Schneiderman, G. Figueras, M. Chukharkin, A. Kalabukhov, A. Hedström, M. Elam, and D. Winkler, "High-Tc superconducting quantum interference device recordings of spontaneous brain activity: Towards high-Tc magnetoencephalography," *Appl. Phys. Lett.*, vol. 100, no. 13, p. 132601, 2012.

[10] M. Xie, J. F. Schneiderman, M. L. Chukharkin, A. Kalabukhov, B. Riaz, D. Lundqvist, S. Whitmarsh, M. Hämäläinen, V. Jousmäki, R. Oostenveld,

et al., "Benchmarking for on-scalp MEG sensors," *IEEE Trans. Biomed. Eng.*, vol. 64, no. 6, pp. 1270–1276, 2017.

[11] M. Hämäläinen, R. Hari, R. J. Ilmoniemi, J. Knuutila, and O. V. Lounasmaa, "Magnetoencephalography—theory, instrumentation, and applications to non-invasive studies of the working human brain," *Rev. Mod. Phys.*, vol. 65, no. 2, p. 413, 1993.

[12] S. Supek and C. J. Aine, *Magnetoencephalography.* Springer, 2014.

[13] M. S. Hämäläinen and R. J. Ilmoniemi, "Interpreting magnetic fields of the brain: minimum norm estimates," *Med. Biol. Eng. Comput.*, vol. 32, no. 1, pp. 35–42, 1994.

[14] S. Baillet, J. C. Mosher, and R. M. Leahy, "Electromagnetic brain mapping," *IEEE Signal Process. Mag.*, vol. 18, no. 6, pp. 14–30, 2001.

[15] S. Murakami and Y. Okada, "Contributions of principal neocortical neurons to magnetoencephalography and electroencephalography signals," *J. Physiol.*, vol. 575, no. 3, pp. 925–936, 2006.

[16] P. Hansen, M. Kringelbach, and R. Salmelin, *MEG: an introduction to methods.* Oxford university press, 2010.

[17] R. Hari and L. Parkkonen, "The brain timewise: how timing shapes and supports brain function," *Philos. Trans. Royal Soc. B*, vol. 370, no. 1668, p. 20140170, 2015.

[18] P. Adjamian, "The application of electro-and magneto-encephalography in tinnitus research–methods and interpretations," *Front. Neurol.*, vol. 5, p. 228, 2014.

[19] M. Scherg, *Auditory evoked magnetic fields and electric potentials. Advances in audiology*, vol. 6. S Karger, Basel, 1990.

[20] R. Schmidt, "Multiple emitter location and signal parameter estimation," *IEEE Trans. Antennas Propag.*, vol. 34, no. 3, pp. 276–280, 1986.

[21] J. C. Mosher, P. S. Lewis, and R. M. Leahy, "Multiple dipole modeling and localization from spatio-temporal MEG data," *IEEE Trans. Biomed. Eng.*, vol. 39, no. 6, pp. 541–557, 1992.

[22] J. C. Mosher and R. M. Leahy, "Source localization using recursively applied and projected (RAP) MUSIC," *IEEE Trans. Signal Process.*, vol. 47, no. 2, pp. 332–340, 1999.

[23] K. Uutela, S. Taulu, and M. Hämäläinen, "Detecting and correcting for head movements in neuromagnetic measurements," *Neuroimage*, vol. 14, no. 6, pp. 1424–1431, 2001.

[24] T. Bardouille, S. V. Krishnamurthy, S. G. Hajra, and R. C. D'Arcy, "Improved localization accuracy in magnetic source imaging using a 3-d laser scanner," *IEEE Trans. Biomed. Eng.*, vol. 59, no. 12, pp. 3491–3497, 2012.

[25] S. Vema Krishna Murthy, M. MacLellan, S. Beyea, and T. Bardouille, "Faster and improved 3-d head digitization in MEG using kinect," *Front. Neurosci.*, vol. 8, p. 326, 2014.

[26] E. Urban and R. T. Wakai, "Optical sensor position indicator for neonatal MEG," *IEEE Trans. Biomed. Eng.*, vol. 59, no. 1, pp. 255–262, 2012.

[27] L. Engels, X. De Tiege, M. O. de Beeck, and N. Warzée, "Factors influencing the spatial precision of electromagnetic tracking systems used for MEG/EEG source imaging," *Clin. Neurophysiol.*, vol. 40, no. 1, pp. 19–25, 2010.

[28] D. Cohen, "Magnetoencephalography: detection of the brain's electrical activity with a superconducting magnetometer," *Science*, vol. 175, no. 4022, pp. 664–666, 1972.

[29] J. Bardeen, L. N. Cooper, and J. R. Schrieffer, "Microscopic theory of superconductivity," *Phys. Rev.*, vol. 106, no. 1, p. 162, 1957.

[30] J. G. Bednorz and K. A. Müller, "Possible high-Tc superconductivity in the Ba-La-Cu-O system," *Z. Phys. B*, vol. 64, no. 2, pp. 189–193, 1986.

[31] C. Poole, R. Prozorov, H. Farach, and R. Creswick, *Superconductivity.* Elsevier, 2014.

[32] V. V. Schmidt, *The physics of superconductors: Introduction to fundamentals and applications.* Springer Science & Business Media, 2013.

[33] B. D. Josephson, "Possible new effects in superconductive tunnelling," *Phys. Lett.*, vol. 1, no. 7, pp. 251–253, 1962.

[34] J. Clarke and A. I. Braginski, *The SQUID handbook: Applications of SQUIDs and SQUID systems.* John Wiley & Sons, 2006.

[35] R. P. Feynman, R. B. Leighton, and M. Sands, *Feynman lectures on physics : Vol. 3. Quantum Mechanics.* Addison-Wesley, 1965.

[36] D. Drung, "High-Tc and low-Tc dc SQUID electronics," *Supercond. Sci. Technol.*, vol. 16, pp. 1320–1336, Oct 2003.

[37] M. Xie, M. Chukharkin, S. Ruffieux, J. Schneiderman, A. Kalabukhov, M. Arzeo, T. Bauch, F. Lombardi, and D. Winkler, "Improved coupling of nanowire-based high-Tc SQUID magnetometers—simulations and experiments," *Supercond. Sci. Technol.*, vol. 30, no. 11, p. 115014, 2017.

[38] F. Ludwig, E. Dantsker, D. Koelle, R. Kleiner, A. Miklich, and J. Clarke, "Multilayer magnetometers based on high-Tc SQUIDs," *Appl. Supercond.*, vol. 3, no. 7-10, pp. 383–398, 1995.

[39] M. Chukharkin, A. Kalabukhov, J. F. Schneiderman, F. Öisjöen, O. Snigirev, Z. Lai, and D. Winkler, "Noise properties of high-Tc superconducting flux transformers fabricated using chemical-mechanical polishing," *Appl. Phys. Lett.*, vol. 101, no. 4, p. 042602, 2012.

[40] M. Faley, U. Poppe, K. Urban, D. Paulson, and R. Fagaly, "A new generation of the HTS multilayer dc-SQUID magnetometers and gradiometers," in *Journal of Physics: Conference Series*, vol. 43, p. 1199, IOP Publishing, 2006.

[41] D. Drung, F. Ludwig, W. Müller, U. Steinhoff, L. Trahms, H. Koch, Y. Shen, M. Jensen, P. Vase, T. Holst, *et al.*, "Integrated YBa2Cu3O7-x magnetometer for biomagnetic measurements," *Appl. Phys. Lett.*, vol. 68, no. 10, pp. 1421–1423, 1996.

[42] J. E. Knuutila, A. I. Ahonen, M. Hamalainen, M. J. Kajola, P. P. Laine, O. Lounasmaa, L. Parkkonen, J. Simola, and C. Tesche, "A 122-channel whole-cortex SQUID system for measuring the brain's magnetic fields," *IEEE Trans. Magn.*, vol. 29, no. 6, pp. 3315–3320, 1993.

[43] S. Della Penna, C. Delgratta, C. Granata, A. Pasquarelli, V. Pizzella, R. Rossi, M. Russo, K. Torquatiand, and S. Erné, "Biomagnetic systems for clinical use," *Philos. Mag. B*, vol. 80, no. 5, pp. 937–948, 2000.

[44] Y. Okada, M. Hämäläinen, K. Pratt, A. Mascarenas, P. Miller, M. Han, J. Robles, A. Cavallini, B. Power, K. Sieng, *et al.*, "BabyMEG: a whole-head pediatric magnetoencephalography system for human brain development research," *Rev. Sci. Instrum.*, vol. 87, no. 9, p. 094301, 2016.

[45] J. Iivanainen, R. Zetter, M. Grön, K. Hakkarainen, and L. Parkkonen, "On-scalp MEG system utilizing an actively shielded array of optically-pumped magnetometers," *Neuroimage*, vol. 194, pp. 244 – 258, 2019.

[46] T. P. Roberts, D. N. Paulson, G. Hirschkoff, K. Pratt, A. Mascarenas, P. Miller, M. Han, J. Caffrey, C. Kincade, W. Power, *et al.*, "Artemis 123: development of a whole-head infant and young child MEG system," *Front. Hum. Neurosci.*, vol. 8, p. 99, 2014.

[47] Y. Okada, K. Pratt, C. Atwood, A. Mascarenas, R. Reineman, J. Nurminen, and D. Paulson, "BabySQUID: a mobile, high-resolution multichannel magnetoencephalography system for neonatal brain assessment," *Rev. Sci. Instrum.*, vol. 77, no. 2, p. 024301, 2006.

[48] B. Lutkenhoner, "Current dipole localization with an ideal magnetometer system," *IEEE Trans. Biomed. Eng.*, vol. 43, no. 11, pp. 1049–1061, 1996.

[49] J. F. Schneiderman, "Information content with low-vs. high-Tc SQUID arrays in MEG recordings: The case for high-Tc SQUID-based MEG," *J. Neurosci. Methods*, vol. 222, pp. 42–46, 2014.

[50] Elekta Neuromag Oy, Helsinki, Finland, *Elekta Neuromag System Hardware User's Manual*, 2005.

[51] P. Kemppainen and R. Ilmoniemi, "Channel capacity of multichannel magnetometers," in *Advances in Biomagnetism*, pp. 635–638, Springer, 1989.

[52] C. E. Shannon, "A mathematical theory of communication," *Bell system technical journal*, vol. 27, no. 3, pp. 379–423, 1948.

[53] M. S. Beauchamp, M. R. Beurlot, E. Fava, A. R. Nath, N. A. Parikh, Z. S. Saad, H. Bortfeld, and J. S. Oghalai, "The developmental trajectory of brain-scalp distance from birth through childhood: implications for functional neuroimaging," *PLoS One*, vol. 6, no. 9, p. e24981, 2011.

[54] R. Zetter, J. Iivanainen, M. Stenroos, and L. Parkkonen, "Requirements for coregistration accuracy in on-scalp MEG," *Brain Topogr.*, vol. 31, no. 6, pp. 931–948, 2018.

[55] R. Oostenveld, P. Fries, E. Maris, and J.-M. Schoffelen, "FieldTrip: Open source software for advanced analysis of MEG, EEG, and invasive electrophysiological data," *Comput. Intell. Neurosci.*, vol. 2011, pp. 1–9, 2011.

[56] R. Koch, C. Umbach, G. Clark, P. Chaudhari, and R. Laibowitz, "Quantum interference devices made from superconducting oxide thin films," *Appl. Phys. Lett.*, vol. 51, no. 3, pp. 200–202, 1987.

[57] Y. Zhang, Y. Tavrin, M. Mück, A. I. Braginski, C. Heiden, S. Hampson, C. Pantev, and T. Elbert, "Magnetoencephalography using high temperature rf SQUIDs," *Brain Topogr.*, vol. 5, pp. 379–382, Jun 1993.

[58] R. Hari, K. Aittoniemi, M.-L. Järvinen, T. Katila, and T. Varpula, "Auditory evoked transient and sustained magnetic fields of the human brain localization of neural generators," *Exp. Brain Res.*, vol. 40, no. 2, pp. 237–240, 1980.

[59] R. Hari, M. Hämäläinen, E. Kaukoranta, K. Reinikainen, and D. Teszner, "Neuromagnetic responses from the second somatosensory cortex in man," *Acta Neurol. Scand.*, vol. 68, no. 4, pp. 207–212, 1983.

[60] R. Hari, E. Kaukoranta, K. Reinikainen, T. Huopaniemie, and J. Mauno, "Neuromagnetic localization of cortical activity evoked by painful dental stimulation in man," *Neurosci. Lett.*, vol. 42, no. 1, pp. 77–82, 1983.

[61] J. Dammers, H. Chocholacs, E. Eich, F. Boers, M. Faley, R. E. Dunin-Borkowski, and N. Jon Shah, "Source localization of brain activity using helium-free interferometer," *Appl. Phys. Lett.*, vol. 104, no. 21, p. 213705, 2014.

[62] R. Ilmoniemi, R. Hari, and K. Reinikainen, "A four-channel SQUID magnetometer for brain research," *Electroencephalogr. Clin. Neurophysiol.*, vol. 58, no. 5, pp. 467–473, 1984.

[63] P. Carelli, C. Del Gratta, V. Foglietti, I. Modena, A. Pasquarelli, V. Pizzella, M. Pullano, G. Romani, and G. Torrioli, "A nine channel dc SQUID system for biomagnetism," in *Advances in Biomagnetism*, pp. 665–668, Springer, 1989.

[64] H. Ohta, M. Takahata, Y. Takahashi, K. Shinada, Y. Yamada, T. Hanasaka, Y. Uchikawa, M. Kotani, T. Matsui, and B. Komiyama, "Seven-channel rf SQUID with 1/f noises only at very low frequencies," *IEEE Trans. Magn.*, vol. 25, no. 2, pp. 1018–1021, 1989.

[65] C. Guy, A. Cayles, S. Walker, and K. Leedham-Green, "A multi-channel bio-magnetometer," in *Advances in Biomagnetism*, pp. 661–664, Springer, 1989.

[66] O. Dossel, B. David, M. Fuchs, W. Kullmann, and K. Ludeke, "A modular low noise 7-channel SQUID-magnetometer," *IEEE Trans. Magn.*, vol. 27, no. 2, pp. 2797–2800, 1991.

[67] S. Ahlfors, A. Ahonen, G. Ehnholm, M. Hämäläinen, R. Ilmoniemi, M. Kajola, M. Kiviranta, J. Knuutila, O. Lounasmaa, J. Simola, *et al.*, "A 24-SQUID gradiometer for magnetoencephalography," *Physica B*, vol. 165, pp. 97–98, 1990.

[68] V. Foglietti, C. Del Gratta, A. Pasquarelli, V. Pizzella, G. Torrioli, G. Romani, W. Gallagher, M. Ketchen, A. Kleinsasser, and R. Sandstrom, "28-channel hybrid system for neuromagnetic measurements," *IEEE Trans. Magn.*, vol. 27, no. 2, pp. 2959–2962, 1991.

[69] H. Koch, R. Cantor, D. Drung, S. Erné, K. Matthies, M. Peters, T. Ryhanen, H. Scheer, and H. Hahlbohm, "A 37 channel dc SQUID magnetometer system," *IEEE Trans. Magn.*, vol. 27, no. 2, pp. 2793–2796, 1991.

[70] J. Vrba, K. Betts, M. Burbank, T. Cheung, A. Fife, G. Haid, P. Kubik, S. Lee, J. McCubbin, J. McKay, *et al.*, "Whole cortex, 64 channel SQUID biomagnetometer system," *IEEE Trans. Appl. Supercond.*, vol. 3, no. 1, pp. 1878–1882, 1993.

[71] National Instruments, Austin, TX, USA, *NI 6259 Device Specifications*, 2016.

[72] Mangicon GmbH, Hamburg, Germany, *High Performance dc SQUID Electronics SEL1 Manual v3.3.8*, 2011.

[73] S. Tanaka, H. Itozaki, and H. Kado, "Flux trapping of high-Tc dc SQUID," in *Advances in Superconductivity VII*, pp. 1117–1120, Springer, 1995.

[74] A. Miklich, D. Koelle, T. Shaw, F. Ludwig, D. Nemeth, E. Dantsker, J. Clarke, N. McN. Alford, T. W. Button, and M. Colclough, "Low-frequency excess noise in YBa2Cu3O7-x dc superconducting quantum interference devices cooled in static magnetic fields," *Appl. Phys. Lett.*, vol. 64, no. 25, pp. 3494–3496, 1994.

[75] E. Dantsker, S. Tanaka, and J. Clarke, "High-Tc super conducting quantum interference devices with slots or holes: Low 1/f noise in ambient magnetic fields," *Appl. Phys. Lett.*, vol. 70, no. 15, pp. 2037–2039, 1997.

[76] M. Iwasaki, E. Pestana, R. C. Burgess, H. O. Lüders, H. Shamoto, and N. Nakasato, "Detection of epileptiform activity by human interpreters: blinded comparison between electroencephalography and magnetoencephalography," *Epilepsia*, vol. 46, no. 1, pp. 59–68, 2005.

[77] H. Berger, "Über das Elektrenkephalogramm des Menschen," *Eur. Arch. Psychiatry Clin. Neurosci.*, vol. 87, no. 1, pp. 527–570, 1929.

[78] H. Berger, "Über das Elektrenkephalogramm des Menschen," *Eur. Arch. Psychiatry Clin. Neurosci.*, vol. 108, no. 3, pp. 407–431, 1938.

[79] W. Klimesch, "EEG alpha and theta oscillations reflect cognitive and memory performance: a review and analysis," *Brain Res. Rev.*, vol. 29, no. 2-3, pp. 169–195, 1999.

[80] L. Payne and R. Sekuler, "The importance of ignoring: Alpha oscillations protect selectivity," *Curr. Dir. Psychol. Sci.*, vol. 23, no. 3, pp. 171–177, 2014.

[81] pixabay, "pixabay.com," August 2019.

[82] R. Salmelin and R. Hari, "Characterization of spontaneous MEG rhythms in healthy adults," *Electroencephalogr. Clin. Neurophysiol.*, vol. 91, no. 4, pp. 237–248, 1994.

[83] S. Vijayan and N. J. Kopell, "Thalamic model of awake alpha oscillations and implications for stimulus processing," *Proc. Natl. Acad. Sci. U.S.A.*, vol. 109, no. 45, pp. 18553–18558, 2012.

[84] E. D. Adrian, "Brain rhythms," *Nature*, vol. 153, pp. 360–362, Mar 1944.

[85] W. J. Ray and H. W. Cole, "EEG alpha activity reflects attentional demands, and beta activity reflects emotional and cognitive processes," *Science*, vol. 228, no. 4700, pp. 750–752, 1985.

[86] J. J. Foxe and A. C. Snyder, "The role of alpha-band brain oscillations as a sensory suppression mechanism during selective attention," *Front. Psychol.*, vol. 2, p. 154, 2011.

[87] H. H. Jasper, "The ten-twenty electrode system of the international federation," *Electroencephalogr. Clin. Neurophysiol.*, vol. 10, pp. 370–375, 1958.

[88] W. Klimesch, M. Doppelmayr, H. Schimke, and B. Ripper, "Theta synchronization and alpha desynchronization in a memory task," *Psychophysiology*, vol. 34, no. 2, pp. 169–176, 1997.

[89] M. Reite, J. Edrich, J. Zimmerman, and J. Zimmerman, "Human magnetic auditory evoked fields," *Electroencephalogr. Clin. Neurophysiol.*, vol. 45, no. 1, pp. 114–117, 1978.

[90] L. Parkkonen, N. Fujiki, and J. P. Mäkelä, "Sources of auditory brainstem responses revisited: contribution by magnetoencephalography," *Hum. Brain Mapp.*, vol. 30, no. 6, pp. 1772–1782, 2009.

[91] R. Hari, M. Pelizzone, J. Mäkelä, J. Hällström, L. Leinonen, *et al.*, "Neuromagnetic responses of the human auditory cortex to on-and offsets of noise bursts," *Audiology*, vol. 26, pp. 31–43, 1987.

[92] J. P. Mäkelä, A. Ahonen, M. Hämäläinen, R. Hari, R. Llmoniemi, M. Kajola, J. Knuutila, O. Lounasmaa, L. McEvoy, R. Salmelin, *et al.*, "Functional differences between auditory cortices of the two hemispheres revealed by whole-head neuromagnetic recordings," *Hum. Brain Mapp.*, vol. 1, no. 1, pp. 48–56, 1993.

[93] R. Näätänen, M. Sams, K. Alho, P. Paavilainen, K. Reinikainen, and

E. Sokolov, "Frequency and location specificify of the human vertex N1 wave," *Electroencephalogr. Clin. Neurophysiol.*, vol. 69, no. 6, pp. 523–531, 1988.

[94] G. L. Romani, S. J. Williamson, and L. Kaufman, "Tonotopic organization of the human auditory cortex," *Science*, vol. 216, no. 4552, pp. 1339–1340, 1982.

[95] D. Brenner, J. Lipton, L. Kaufman, and S. Williamson, "Somatically evoked magnetic fields of the human brain," *Science*, vol. 199, no. 4324, pp. 81–83, 1978.

[96] G. Tortora and B. Derrickson, *Introduction to the human body: the essentials of anatomy and physiology.* J. Wiley & Sons, 2007.

[97] R. Hari and N. Forss, "Magnetoencephalography in the study of human somatosensory cortical processing," *Philos. Trans. Royal Soc. B*, vol. 354, no. 1387, pp. 1145–1154, 1999.

[98] W. Penfield and H. Jasper, *Epilepsy and the functional anatomy of the human brain.* Little, Brown & Co., 1954.

[99] A. Nakamura, T. Yamada, A. Goto, T. Kato, K. Ito, Y. Abe, T. Kachi, and R. Kakigi, "Somatosensory homunculus as drawn by meg," *Neuroimage*, vol. 7, no. 4, pp. 377–386, 1998.

[100] *Anatomy and Physiology.* http://cnx.org/content/col11496/1.6/: OpenStax College, 2013.

[101] R. Kakigi, M. Hoshiyama, M. Shimojo, D. Naka, H. Yamasaki, S. Watanabe, J. Xiang, K. Maeda, K. Lam, K. Itomi, *et al.*, "The somatosensory evoked magnetic fields," *Prog. Neurobiol.*, vol. 61, no. 5, pp. 495–523, 2000.

[102] J. Tiihonen, R. Hari, and M. Hämäläinen, "Early deflections of cerebral magnetic responses to median nerve stimulation," *Electroencephalography and Clinical Neurophysiology/Evoked Potentials Section*, vol. 74, no. 4, pp. 290–296, 1989.

[103] B. Riaz, *Bringing MEG towards clinical applications.* PhD thesis, University of Gothenburg, 2018.

[104] S. Erné, L. Narici, V. Pizzella, and G. Romani, "The positioning problem in biomagnetic measurements: A solution for arrays of superconducting sensors," *IEEE Trans. Magn.*, vol. 23, no. 2, pp. 1319–1322, 1987.

[105] T. Bardouille, L. Power, M. Lalancette, R. Bishop, S. Beyea, M. J. Taylor, and B. T. Dunkley, "Variability and bias between magnetoencephalography systems in non-invasive localization of the primary somatosensory cortex," *Clin. Neurol. Neurosurg.*, vol. 171, pp. 63–69, 2018.

[106] G. Curio, B.-M. Mackert, M. Burghoff, R. Koetitz, K. Abraham-Fuchs, and W. Härer, "Localization of evoked neuromagnetic 600 Hz activity in the cerebral somatosensory system," *Electroencephalogr. Clin. Neurophysiol.*, vol. 91, no. 6, pp. 483–487, 1994.

[107] G. Curio, B.-M. Mackert, M. Burghoff, J. Neumann, G. Nolte, M. Scherg, and P. Marx, "Somatotopic source arrangement of 600 Hz oscillatory magnetic fields at the human primary somatosensory hand cortex," *Neurosci. Lett.*, vol. 234, no. 2-3, pp. 131–134, 1997.

[108] A. Eisen, K. Roberts, M. Low, M. Hoirch, and P. Lawrence, "Questions regarding the sequential neural generator theory of the somatosensory evoked potential raised by digital filtering," *Electroencephalography and Clinical Neurophysiology/Evoked Potentials Section*, vol. 59, no. 5, pp. 388–395, 1984.

[109] H. Hughes, T. Darcey, H. Barkan, P. Williamson, D. Roberts, and C. Aslin, "Responses of human auditory association cortex to the omission of an expected acoustic event," *Neuroimage*, vol. 13, no. 6, pp. 1073–1089, 2001.

[110] E. V. Orekhova, A. V. Butorina, O. V. Sysoeva, A. O. Prokofyev, A. Y. Nikolaeva, and T. A. Stroganova, "Frequency of gamma oscillations in humans is modulated by velocity of visual motion," *J. Neurophysiol.*, vol. 114, no. 1, pp. 244–255, 2015.

[111] F. Boldizar and U. Slipac, "Optimizing design of on-scalp MEG systems," master thesis, Chalmers University of Technology, 2017.

A

Instructions for 7-channel operation

A.1   Pumping

The cryostat should be pumped with a turbopump at least for a few hours (to reach below 10^{-4} mbar). If it takes long to get to low pressure, or if the vacuum has been broken while the cryostat was cold, it may be necessary to back-fill the cryostat with nitrogen gas and pump out a few times. Pumping in a warm environment or blowing warm air into the LN_2 tank while pumping can furthermore help the charcoal release trapped water.

Once the cryostat is pumped, close the vacuum connector and disconnect the T-connector (unscrew from the plug first).

A.2   Cooldown

For cooldown the 7-channel system should be placed inside an MSR as central as possible (the field is typically lowest in the center of an MSR), avoiding vibrations (e.g., do not fix it to a long, swinging arm or directly on the floor), as moving the sensors inside the remnant field can lead to flux trapping. During LN_2 transfer the tubes will contract and stretch while freezing. The cryostat should therefore NOT stand freely, but instead be fixed in place. Otherwise it might fall over and get damaged or hurt people in its vicinity. To ensure slow cooldown, the cryostat can be tilted ($\sim$45 degrees) with the sensors facing upwards (this way there is more time for evaporated nitrogen to cool the SQUIDs before liquid reaches them).

If the remnant field inside the MSR is high, set up a Helmholtz coil (preferably with known voltage/current-to-field conversion) where the cryostat will be fixed for cooldown (e.g., attached to wooden arm). Use fluxgate or other magnetometer to measure the field where the sensors will be and in the direction they will be facing (should be inside the Helmholtz coil in the direction of the coil's field). Depending on the magnetometer, it may be necessary to measure in the direction of interest as well as in the opposite direction to subtract offset. Subtracting the two measurements should cancel any offset. Apply a DC voltage/current to the coil to generate a field that cancels the remnant field. Measure again to verify and fine-tune the applied current as needed to minimize the field. Once the field is minimized, disconnect/remove the magnetometer and fix the 7-channel system for cooldown, carefully
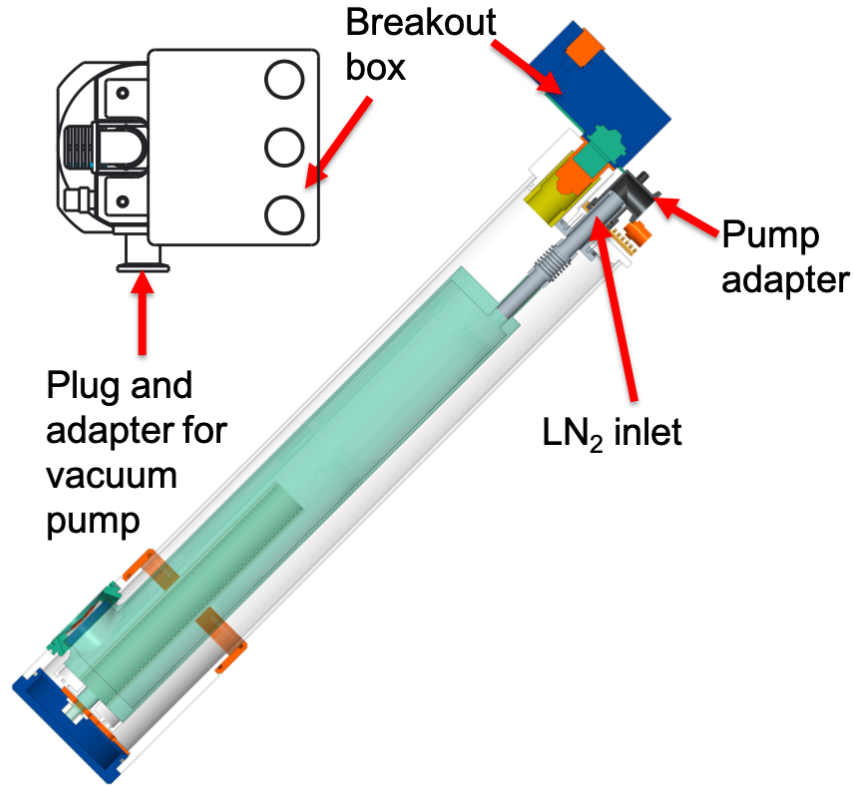
Figure A.1: Schematic of the 7-channel system highlighting parts that are important for cooldown.

avoiding moving the fixture/Helmholtz coil.

Once the fixture is set up, verify that all SQUIDs are shunted at the cryostat breakout box (see Fig. A.1), carefully carry the cryostat into the MSR and fix it for cooldown. Make sure all unnecessary cables into the MSR are removed and all unnecessary equipment turned off. Connect the SQUID electronics to the computer and (in SQUIDViewer) set all biases and generators to zero before connecting them to the breakout box of the cryostat. Unshunt the SQUIDs and set the electronics to sleep (using global mode). Make sure the adapter for pumping on the LN_2 tank, a (non-magnetic!) stick to test filling height, gloves, and all other necessary equipment is inside the MSR before starting the cooldown. Opening the MSR once the LN_2 transfer has started should be minimized. When necessary, open the MSR door slowly and as little as possible. Check the pressure of the pressured air that is used for transferring. Never cool down alone! There should always be a second person outside.

Once everything is set up, put the LN_2 transfer tube into the cryostat. If you have a pressure control valve, set the pressure as required (depends on the size and filling level of the LN_2 dewar but typically well below 1 bar). Otherwise there are two ways to control the pressure inside the LN_2 dewar - and thus the LN_2 flow - directly at the LN_2 dewar. Either reduce the airflow into the dewar by partially closing the

input valve (requires not perfectly tight connection to the dewar since otherwise the tube will popp off) or let air flow out to reduce the pressure by partially opening another valve in the dewar.

The transfer should be relatively slow (on the order of 1h+ in total), starting with mostly gas flowing into the cryostat to slowly pre-cool the SQUIDs (this can take up 1/2 to 2/3 of the total time). Once liquid is filling the cryostat (can typically be heard, sounding like boiling water in a flask) check the filling until the level is satisfactory. If the cryostat is cooled titled and complete filling is desired, wait until the SQUIDs are immersed in liquid before rotating the cryostat. Avoid excessive spilling of nitrogen (some is no problem) because nitrogen spilling out can freeze the o-ring at the inlet of the LN_2 tank, breaking the vacuum.

Once the cryostat is full, release the pressure from the LN_2 dewar by disconnecting it from the pressured air. Wait for the transfer tube to warm up and pull it out of the cryostat. Connect the LN_2 inlet to the pump using the adapter and the pressured air to the pump (can be the same as used for pressurizing the dewar). Turn up the air pressure to gain the desired pumping (usually on the order of 4 bar) and wait for ca. 10-15 min for the temperature to settle (use the output pressure of the pump for orientation). Wake up the electronics and, if used, slowly ramp down the field compensation before turning it off.

A.3 Tuning the SQUIDs

When the cryostat has reached operating temperature, connect the SQUID electronics (all bias and generator off!) to the cryostat's breakout box and then unshunt the SQUIDs. In DC bias mode, set the SQUID bias currents Ib (it can be useful to note bias currents, voltage modulation, and feedback current required to generate 1 flux quantum of each SQUID). If you are using the modified SEL-1 electronics, turn on global mode, set bias mode to AC and turn on slave mode. Then turn off global mode, choose the channel you want to provide the global clock and put it into master mode. All channels should use the same bias reversal frequency now. The global bias mode has a few bugs. To help verify that the global bias works, I recommend choosing a very different bias frequency (e.g., 0.1 kHz) for the channels that don't generate the global bias. That way a clear difference can be seen when going from normal to global bias. Once all the SQUIDs are in AC bias mode and using global bias, set the bias voltage Vb and bias flux Phib for each SQUID by bringing the two curves together (if a filter with cutoff lower than the modulation frequency is applied, Vb is optimal when the variance of the signal is minimal) and then maximizing their overlap, respectively (if a filter with cutoff lower than the modulation frequency is applied, optimum Phib is reached when the amplitude of the combined signal is maximum). If the signal is not centered around zero shift it using the offset voltage Vo (needs to be unlocked to change). Once Ib, Vb, and Phib (Vo, if applicable) are set, put the SQUIDs into FLL mode. The system is ready to operate.

A.4   Calibration

To calibrate the system, connect a waveform generator to the Helmholtz coil and apply a sine wave. Record the magnetic fields with the sensors. If the coil's voltage-to-field conversion is known, you can calculate the responsivity as the ratio of the amplitude of the SQUID output signal and the applied field. Otherwise you need to calibrate the coil with a reference sensor (e.g., fluxgate). Since the SQUIDs are not aligned to each other, a separate recording for each SQUID is necessary to optimally measure their responsivity (although the difference is small). Alternatively, one can record and vary the orientation multiple times and find the maximum responsivity of each SQUID. The maximum is reached when the SQUID faces in the direction of the field.

A.5   Warming up

After recording, turn off master mode in the "master channel" and set all channels to DC mode. Ramp the biases (Ib, Vb, Phib and Phio) to zero. Once all biases are off you can shunt the SQUIDs at the breakout box and disconnect the SQUID electronics. You can leave the cryostat in place to let it boil off all the remaining nitrogen. This can take a while (several hours). Alternatively, you can speed up the process by pouring out the LN_2. Always wear gloves to pour out LN_2 and pour it into a safe container (e.g., a double-walled bottle/pot or a Styrofoam pot). Turn the cryostat slowly to pour the LN_2, as it will rapidly evaporate when touching the warm inlet tube. After the LN_2 is poured out, blowing nitrogen gas into the LN_2 tank make the warming up faster.

   If you do not plan to record again soon, store the cryostat in a safe location. When storing the cryostat for a long period, consider re-pumping it in regular intervals (I would advice approximately once per month).